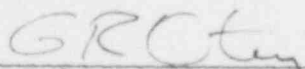NUREG/CR-1509/1of4
SAND80-1304/1of4
R3

LIGHT WATER REACTOR SAFETY RESEARCH PROGRAM
QUARTERLY REPORT JANUARY-MARCH 1980
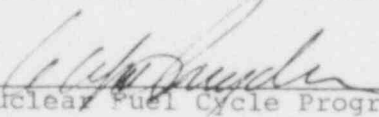
Marshall Berman, Person in Charge

Manuscript Submitted: May 1980
Date Published: July 1980

Approved:

GRCten

Manager, Light Water Reactor Safety Department

signature

Director, Nuclear Fuel Cycle Programs

Sandia National Laboratories
Albuquerque, NM 87185
Operated by
Sandia Corporation
for the
U.S. Department of Energy

8009190743

CONTENTS

ILLUSTRATIONS

Illustrations (cont'd):

TABLES

LIGHT WATER REACTOR SAFETY RESEARCH PROGRAM
QUARTERLY REPORT
JANUARY - MARCH 1980

1. Molten Fuel Concrete Interactions Study

1.1 Summary

The Molten Fuel Concrete Interactions (MFCI) study
is comprised of experimental and analytical investigations
of the chemical and physical phenomena associated with
interactions between molten core materials and concrete.
Such interactions are possible during hypothetical fuel-
melt accidents in light water reactors (LWRs) when molten
fuel and steel from the reactor core penetrate the pres-
sure vessel and cascade onto the concrete substructure.
The purpose of the MFCI study is to develop an understand-
ing of these interactions suitable for risk assessment.
Emphasis is placed on identifying and investigating the
dominant interaction phenomena occurring between proto-
typic materials in order to evaluate:

1. The generation rate and nature of evolved
   noncondensable gases.

2. The effects of gas generation on fission products
   release.

3. The mechanism, rate, and directional nature of concrete erosion by the melt.

In addressing this objective, the experimental program was divided into four areas of investigation:

1. Deposition of Corium-type melts onto concrete.

2. Kinetics and stoichiometry of the thermal decomposition of concrete.

3. Response of concrete to high heat fluxes at one surface.

4. Simulation experiments exploring phenomena at the interface between a melt and a decomposing solid.

In the analytical portion, we are developing a computer model of molten core material concrete interactions capable of providing quantitative estimates of reactor fuel-melt accident situations. We divided this effort into two phases:

1. Development of a preliminary interaction model based on the earliest results from the experimental program - INTER.

2. Development and verification of an improved interaction model that involves a more detailed and refined treatment of the interaction phenomena - CORCON.

2

CORCON development activities concentrated on debugging and check-out of the initial version of the code, CORCON-MOD 0, and bringing it to an operational status. The latter, which represents a major milestone of the analytical program, was achieved at the end of February. We corrected a number of computational problems in accomplishing this goal and, since then, have made additional modifications to CORON. Two of the most important modifications to the original program concern the melt/gas phase chemical equilibrium computation and the basic data structure (i.e., bookkeeping logistics) of the code. We completed the equilibrium computation modifications soon enough to include them in the initial version of the code; modifications to the data structure were not incorporated until after CORCON-MOD 0 became operational.

During testing and debugging of the mass and energy transport and conservation routines in CORCON, it became apparent that a change in the basic data structure within the code would simplify it considerably. It was found to be computationally more efficient to model the system as a fixed number of layers (the maximum possible), some of which might contain no material, than to employ a variable number of layers with flags to identify their contents, as was done in the original program. With this new concept, which has been developed and implemented, layer masses

and energies are updated for mass transfer, mass related
energy transfer, and chemistry in two passes through the
system--upward, then downward, following the flow of
rising and falling materials, respectively. The final
energy conservation calculation for each layer, which
involves the temperature driven energy flows into and
out of the layer, is performed using a linearized implicit
scheme to insure computational stability.

Modifications to the melt/gas phase chemical equili-
brium computation improve the stability and convergence and
reduce the number of iterations required. We replaced
the linear equation solver used in the original routine
with a singular value decomposition solution algorithm
that computes a well-behaved, approximate solution to
almost singular linear problems. The use of this algorithm
has significantly reduced the number of iterations required
for a solution and, hence, the overall computation time
as well. The algorithm also eliminates the need for intro-
ducing fictitious amounts of elements that are physically
absent, solely for computational purposes.

Several other computational problems were identified
and corrected during the quarter. In addition, the CORCON
data input routine and the associated input instructions
were extensively revised to eliminate unused portions and
insure compatibility with the initial version.

CORCON-MOD 0 contains all of the essential elements
of the melt/concrete interaction process. It does have
several simplifications and approximations, however, that
restrict its application. The most significant are:
1. no coolant included, 2. superficial treatment of the
melt atmosphere, 3. constant convective heat transfer
coefficients in the pool and atmosphere, and 4. no decay
heat generation model.

Sample problem input conditions representative of
the Zion and Indian Point nuclear power plants were
identified based on data obtained from structural
drawings of the two plants, results of MARCH-CORRAL calcu-
lations performed by Battelle Columbus Laboratory (BCL),
and the Zion/Indian Point (ZIP) Study.[1-3] An initial
sample problem calculation has been made with CORCON-MOD 0
out to a time of 1-1/2 hours. The results are compared
with the predictions of two other melt concrete interac-
tion codes, INTER[4] and WECHSL[5], for the same input
conditions. Despite the preliminary nature of the CORCON
results (as a consequence of the approximations and
simplifications in the initial version), it is signifi-
cant that the general trends of the CORCON variations
are qualitatively similar to the WECHSL predictions.

Experimental activities during the quarter produced
results in three separate areas: the code comparison

tests, aerosol generation rates, and the viscosity of two-phase mixtures. The objective of the code comparison tests was to provide a comprehensive set of quality data as a basis for evaluating various melt/concrete interaction computer models. To accomplish this task, code developers and evaluators require sufficient information about the tests to define code input conditions. A complete description of the experimental conditions for the two code comparison tests, CC-1 and CC-2, is provided to meet this requirement. Data obtained before and during the tests are presented, instrumentation and measurement techniques are described, and the quality of the various experimental results is discussed. Actual test results will be withheld until after all code comparison calculations have been made.

Aerosol generation during melt/concrete interactions has been monitored in both large- and small-scale tests. Optical transmission was used to determine the aerosol concentration in the gas flow above the melt. Aerosols were collected for particle size analysis and determination of chemical composition using inertial cascade impactors. Early results based on analysis of only a small portion of the data collected during the experimental program have led to a number of observations concerning the effects of various interaction phenomena on aerosol

concentration, composition, and production. An empirical
model describing the amount of aerosol produced during
an interaction was developed based on data from one
small-scale, transient, Corium/concrete test and two
large-scale, sustained, stainless-steel/concrete tests.
The form of the correlation appears quite attractive
because of the manner in which it includes explicitly
the effects of gas flow through the melt and melt tempera-
ture on aerosol generation.

1.2 CORCON Model Development (R. K. Cole, M. L. Corradini,
    J. F. Muir, D. A. Powers)

Development of an improved molten core/concrete
interaction model, CORCON, continued. CORCON is a user-
oriented computer program written in a modular structure
in which most computational units are contained in separate
subroutines. Maximum use is made of existing codes and
subroutines. Phenomenological models developed for the
code have relied heavily on existing techniques, and data
and correlations available in the literature. Numerous
input options provide a flexibility that enables a variety
of problems to be solved by merely changing input data.

We achieved several milestones in the CORCON develop-
ment effort during the past year:

1. Performed the first successful calculation through the point where the metallic and primary oxidic layers of the melt flip and the primary and secondary oxidic layers are combined.

2. Performed the first calculation including complete energy transport among, and conservation within, all components of the system (producing time-varying melt temperatures).

3. Brought to an operational status, the initial version of the program, CORCON-MOD 0.

4. Performed sample problem calculations with CORCON-MOD 0 for conditions representative of those postulated to exist during an LWR fuel melt accident and compared the results with the predictions of other melt/concrete interaction codes.

The efforts and activities associated with these accomplishments are described in the following sections.

1.2.1 Programming and Numerical Concerns

During the quarter we completed, debugged, and checked out the initial version of CORCON. The checkout was performed by exercising the code on a sample problem that is representative of nuclear reactor fuel-melt accident conditions. Debugging activities consisted

of identifying and correcting programming errors as well as modelling deficiencies and omissions.

During testing and debugging of the energy conservation routines in CORCON, it became apparent that the mass-transfer and chemistry-related terms were causing the most difficulties. The problems were primarily in bookkeeping, i.e., deciding which terms were present and then properly adding or subtracting energy from the correct component of the system (either from pool layers [melt and coolant] or from the atmosphere above the pool).

On reconsideration of the basic problem, we decided that a change in data structure would simplify the code considerably. Rather than describe the system as a variable number of layers with flags to specify their contents, it was found to be computationally more efficient to describe it as a fixed number of layers (the maximum possible) some of which might contain no material. This concept was developed with the layers being, from the bottom up: heavy oxide phase (HOX), heavy heterogeneous mixture (HMX), metallic phase (MET), light heterogeneous mixture (LMX), light oxide phase (LOX), coolant (CLN) and the atmosphere (ATM). (See Figures 1-3). The three letter mnemonics are useful in describing the pool

structure, and have been used in appropriate variable names in the code written to test this concept.

In this scheme, a two-phase, metallic and oxidic, melt would assume any one of three possible configurations depending on phase densities: it would have mass in HOX and MET (when $\rho_{OX} > \rho_{MET}$) or in MET and LOX (when $\rho_{OX} < \rho_{MET}$) for a two-layer configuration, while a three-layer pool would have mass in HOX, MET, and LOX (with $\rho_{HOX} > \rho_{MET} > \rho_{LOX}$). Pool inversion (layer flip) is handled by adding the contents of HOX to LOX and then zeroing out HOX "between timesteps." At present, CLN is always absent, and ATM is only partially included. (See Section 1.2.2.) The two heterogeneous mixtures (HMX and LMX) are included in anticipation of future model improvement. Their mass- and energy-conservation equations are included and solved, but the logic for creation or elimination of these layers is extremely rudimentary at present.

The masses and energies of all pool layers are updated for mass-transfer, mass related energy transfer, and chemistry in two passes. The first, up through the pool, follows rising gases and rising condensed-phase species from concrete decomposition or melt/gas-phase reactions. The compositions and enthalpies of these rising materials are followed and modified for chemical reactions. The materials are thermally equilibrated

with layers they pass through, and their energy is ultimately
added to the layer where they remain. The second, or
downward, pass is similar, following ablation products
from surroundings and sinking reaction and concrete
ablation products. Figures 1-1 through 1-3 show this in
more explicit detail -- the actual code follows these
figures rather closely. In these figures, M/G refers to
the melt/gas oxidation reaction, and O/A to the oxide/
atmosphere reduction reaction. The latter is, of course,
considered for at most one layer (only for an oxide-
containing layer in contact with the atmosphere).

When the new routine, MHTRAN, was completed, tested,
and incorporated into CORCON, it was possible to eliminate
the original mass conservation routine, MASCON. However,
before doing this, we made calculations using the two
routines in parallel, and then checked the results exten-
sively to insure that the two were identical. Finally,
we found that a simple explicit advancement of the energy
equation was unstable for reasonable timesteps. The
problem was with the terms representing heat transfer
between layers and from the pool surface to the atmosphere
and the surroundings. This calculation was there-
fore replaced by a linearized implicit scheme. These
terms have the form

$$\Delta H_i = [Q_i \ (T_{i-1}, T_i) - Q_{i+1} \ (T_i, T_{i+1})] \ \Delta t$$
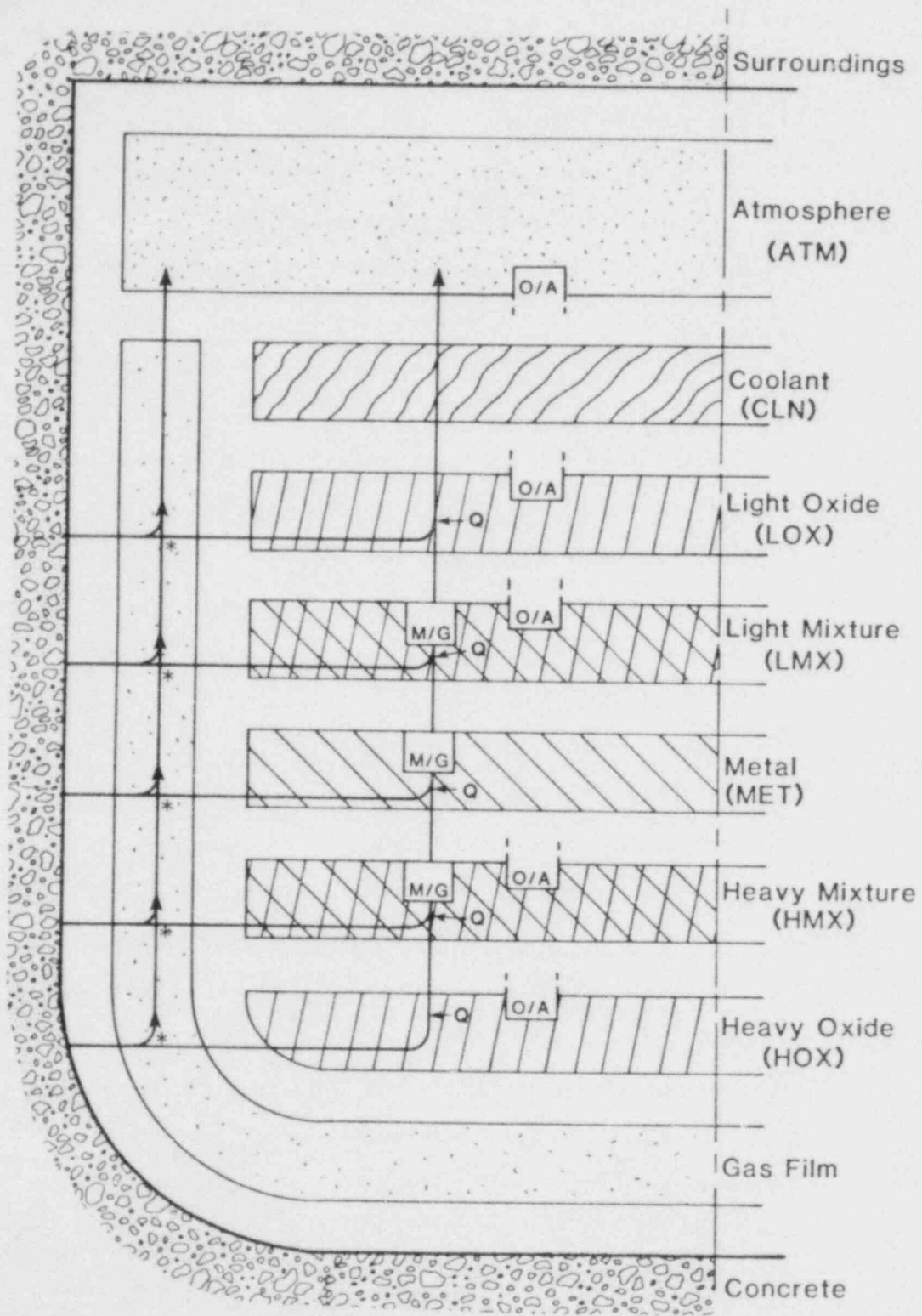
Figure 1-1. Path of Gas Through Pool. Whether gas
goes into film or pool at each * is
determined by body angle. Q denotes
thermal equilibration.
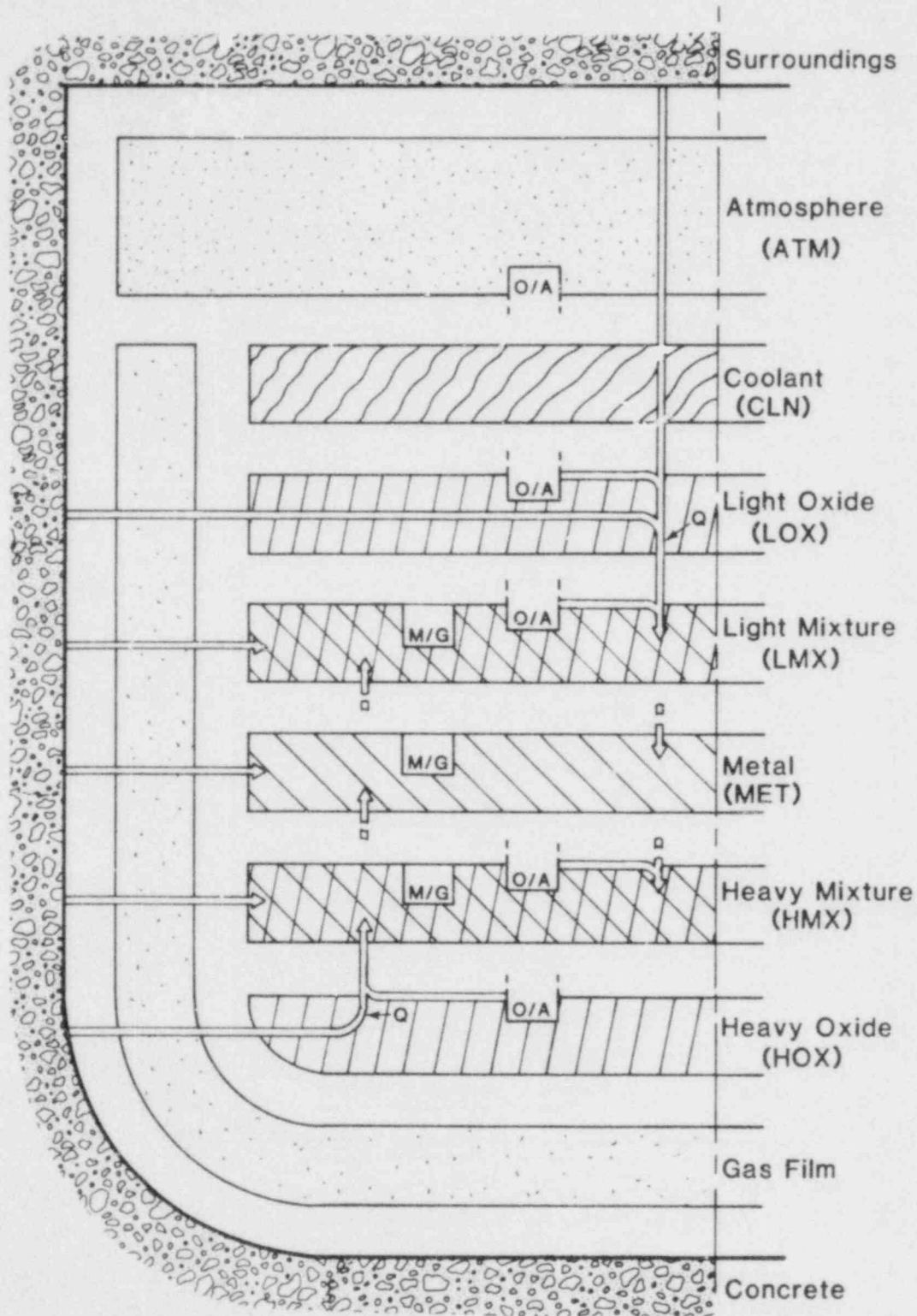
Figure 1-2. Path of Metal Through Pool.
Q denotes thermal equilibration.
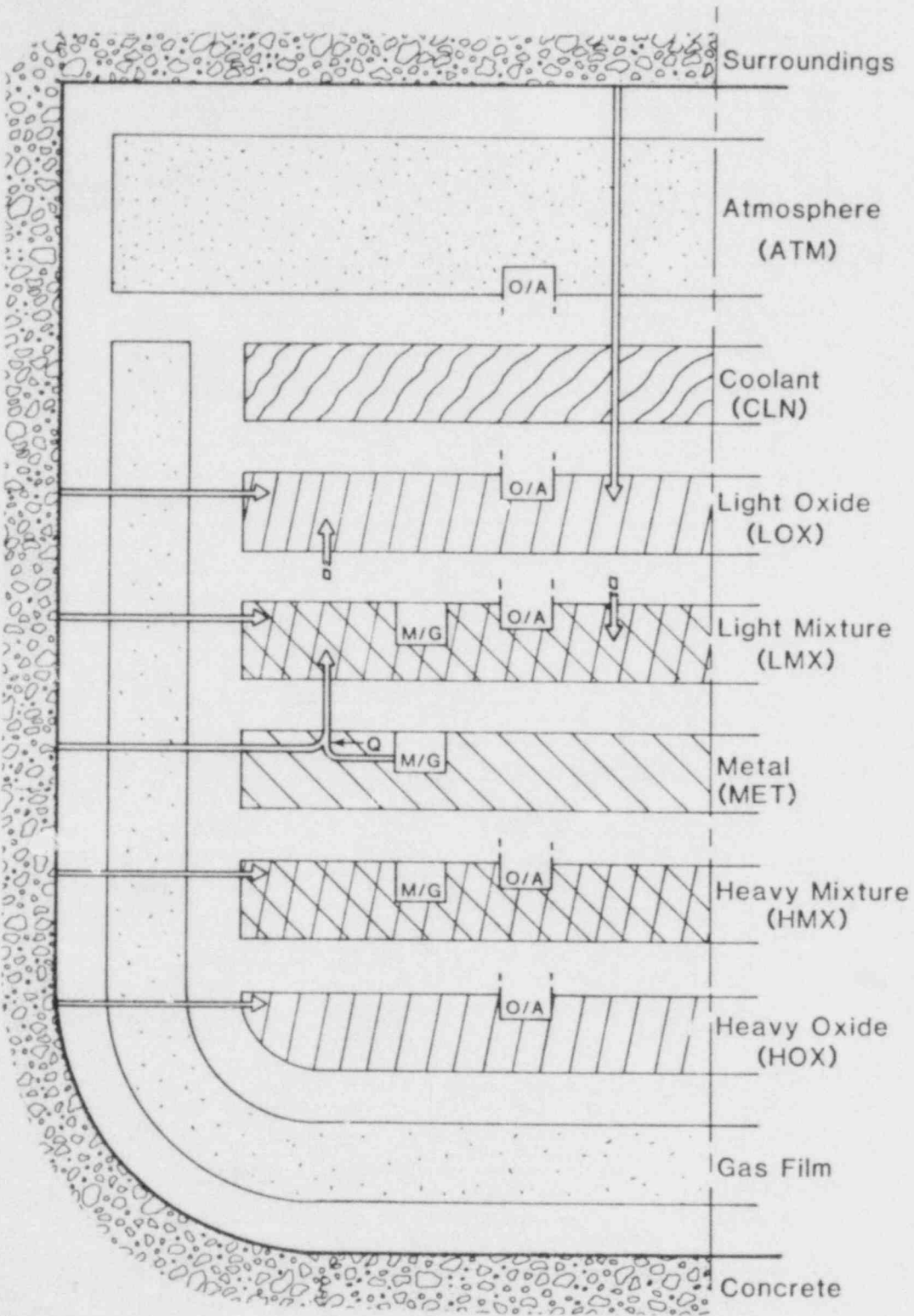
Figure 1-3. Path of Oxide Through Pool.
Q denotes thermal equilibration.

where H_i is the total enthalpy of layer i, and Q_i, Q_{i+1} are the heat flow rates (W) at its lower and upper interface, T is temperature and t is time. For an explicit calculation, the temperatures at the start of the time step, T^n, are used to evaluate the Q's. In an implicit calculation, some fraction Ω (where $0 < \Omega \leq 1$) of the heat flow is evaluated using the (as-yet unknown) temperatures at the end of the time-step. Thus, we have

$$H_i^{n+1} = H_i^{n+1}(expl) + \Omega \left\{ \left[Q_i \left(T_{i-1}^{n+1}, T_i^{n+1} \right) - Q_i \left(T_{i-1}^n, T_i^n \right) \right] \right.$$
$$\left. - \left[Q_{i+1} \left(T_i^{n+1}, T_{i+1}^{n+1} \right) - Q_{i+1} \left(T_i^n, T_{i+1}^n \right) \right] \right\}$$

where $H_i^{n+1}(expl)$ is the fully explicit solution (corresponding to $\Omega = 0$). Rather than solve this set of equations iteratively for the H_i^{n+1} and T_i^{n+1} which satisfy the equation of state, it was linearized by expanding each Q in terms of the layer temperatures, and approximating

$$T_i^{n+1} \approx T_i^n + X_i$$

where

15

$$X_i \equiv \left(H^{n+1}_i - \hat{H}_i \right) \Big/ \hat{C}_i \ ,$$

$\hat{H}_i$ is the total enthalpy of the _new_ layer mass at the _old_ temperature T^n_i and $\hat{C}_i$ the corresponding heat capacity. The result is a set of equations

$$- \Omega \, \frac{\partial Q_i}{\partial T_{i-1}} \, x_{i-1} + \left[\hat{C}_i + \Omega \left(\frac{\partial Q_{i+1}}{\partial T_i} - \frac{\partial Q_i}{\partial T_i} \right) \right] x_i + \Omega \, \frac{\partial Q_{i+1}}{\partial T_i} \, x_{i+1}$$

$$= H_i^{n+1}(\text{expl}) - \hat{H}_i$$

which are easily solved for the X_i. Then, we have

$$H^{n+1}_i = \hat{H}_i + \hat{C}_i X_i$$

and may find the new layer temperatures T^{n+1}_i with a simple Newton's iteration on temperature. Two comments seem appropriate: (1) the $\partial Q / \partial T$ terms are, of course, essentially interlayer heat transfer coefficients except for the radiative surface-to-surroundings term where a more complicated expression is obtained, and (2) while the equations are tridiagonal, advantage has not been taken of this feature and a general-purpose linear equation solvers, SAXB, from the Sandia Mathematical Subroutine Library, is used in the program. This algorithm is coded as part of the subroutine ENRCON, which handles those parts of the energy conservation equation not included in MHTRAN.

An energy balance at the pool/gas film-interface requires simultaneous solution of the equations:

$$(\dot{m} \Delta H)_{conc} = \sigma \epsilon_{eff}(T_A^4 - T_W^4) + h_F(T_A - T_W)$$

$$(\dot{m} \Delta H)_{conc} = h_{P\ell} (T_B - T_A),$$

where

T_B = pool bulk temperature

T_A = pool/film interface temperature

T_W = concrete surface ablation temperature

$\dot{m}$ = concrete ablation rate

ΔH = concrete ablation enthalpy

h_F = film heat-transfer coefficient

$h_{P\ell}$ = pool boundary heat-transfer coefficient

σ = Stefan Boltzman constant

ϵ_{eff} = effective emissivity = $(1/\epsilon_W + 1/\epsilon_{P\ell} + 1)^{-1}$

In the original CASCET* package developed by Acurex/Aerotherm Corp., these equations were not solved simultaneously. The value of $\dot{m}$ from the previous time-step was used in the second equation to calculate a T_A which was then used in the first equation to calculate a new $\dot{m}$. (A special iteration was performed for the first time-step, using subroutine MITT.)

---

*Concrete Ablation/Shape Change Evaluation Technique

This process is probably adequate. However, it did, on occasion, produce small negative values for $\dot{m}$. This problem has been eliminated by modifying the routine SURFEB to employ what is essentially a Newton's iteration to generate a simultaneous solution. Convergence is very fast, with five-figure agreement (and guaranteed positive $\dot{m}$) typically requiring two to four iterations. Subroutine MITT is no longer needed and has been eliminated.

The melt/gas-phase chemical equilibrium computation, subroutine MLTREA, is being modified in an effort to insure convergence and reduce the number of iterations required. A number of modificatons have been tried with mixed success. One that made a significant improvement to the computation involved the use of a different solution algorithm. The solution of the linear equations employed in the initial version of the equilibrium model was found to be extremely unstable -- the equations are nearly singular. Differences as small as 2 or 3 bits in the inputs to the computation (such as occurred when the input data computation routine was changed to replace X**0.5 by SQRT [X]) caused changes in the amounts of the trace species (reaction products) of as much as three orders of magnitude, while amounts of the major product species differed only in the fourth or fifth place. This sensitivity of the results to machine procedures would

have made it impossible to compare results obtained using two different computers. To rectify this, the linear equation solver was replaced with a Singular Value Decomposition solution algorithm (SVDRS, available in the Sandia Numerical Mathematical Subroutine Library). SVDRS computes a well-behaved, approximate (in a least-squares sense) solution to almost singular linear problems. The use of this algorithm has caused a significant reduction in the number of iterations required for a solution, particularly for the oxide/atmosphere reaction calculations. In addition, the computation time has been reduced by a factor of at least three. An additional benefit of this modification is that it eliminates the necessity of introducing (for computational reasons only) fictitious amounts of elements that are physically absent.

The above modification solved one problem but, unfortunately, others remained. Changes introduced to solve these worked for some situations but not for others; none was universally successful. A re-examination of the entire solution algorithm is in process to determine if a more basic modification can be made to insure rapid convergence, and what the nature of such a modification might be.

Several problems involving incorrect calculations were encountered at the timestep at which pool layer

flip and combination occurred. These were corrected. In addition, the CORCON data input routine, DATAIN, was extensively revised to eliminate unused portions and be compatible with the initial version of CORCON. The CORCON input instructions were also revised accordingly.

1.2.2 Initial Version of CORCON

The initial version of the code, designated CORCON-MOD 0, became operational on February 29, 1980. A computer tape containing this version, along with a partial draft of a topical report/user's manual describing the code, were transmitted to NRC on March 4. In this form, the program has a storage requirement of 115K octal. The ratio of problem real-time to computation time varies with problem conditions and time-step size. For the computations that have been made to date (on a CDC 7600), it ranges from approximately 10 to 40; thus the computation time for a 6-hour problem can range from about 9 to 36 minutes.

Although CORCON-MOD 0 contains all of the essential elements of the melt/concrete interaction process, it does have simplifications and approximations that restrict its application. The following limitations are the most significant ones found.

1. Includes no coolant (water) in the system.

2. Treats the atmosphere and its surroundings only superficially to facilitate heat transfer from

the pool surface and the top oxidic layer/atmosphere reduction reaction. Mass and energy flows to and from the atmosphere, other than from the pool surface, are not computed. Consequently, mass and energy conservation within the atmosphere is also omitted. The atmosphere surroundings are treated as a uniform temperature black body ($\epsilon_{surr} = 1.0$); the variation of temperature with time being specified as input to the computation.

3. Includes the convective heat transfer coefficients within the pool and the atmosphere (at the pool surface) as constants. A value of 10^4 (W/m^{2}K) is assumed for heat transfer from the interior of the pool to its periphery (i.e., for melt/concrete heat transfer). Values for the bulk-to-layer interface heat transfer coefficients (for inter-layer and pool/atmosphere heat transfer) are input by the user.

4. Does not model the fission product decay heat generated within the pool. The decay power to the oxidic and metallic phases must be input versus time.

Efforts to supplant these and other simplifications with more realistic models and treatments began with the

completion of CORCON-MOD 0. All will be rectified in the
next version of the code, CORCON-MOD 1, which is anticipated
to be completed by the end of the fiscal year.

1.2.3 Sample Problem Calculations

Three tasks were undertaken during the quarter:
(1) acquiring data representative of the Zion and Indian
Point nuclear power plants and setting up an input data
deck as a sample problem for CORCON, (2) initiating a
scoping sensitivity study of the code using CORCON-MOD 0
with the above ZIP input data as nominal conditions, and
(3) performing sample problem calculations with CORCON-MOD 0
and comparing the results with predictions made by the
INTER and WECHSL (initial version) codes for the same
nominal ZIP conditions.

Input data (initial and boundary conditions) required
for the CORCON sample problem calculations were obtained
from structural drawings of the Zion and Indian Point power
plants (supplied by the Nuclear Reactor Regulation Division,
NRC) and from results of the MARCH-CORRAL calculations per-
formed by Battelle Columbus Laboratory (BCL) as part of the
Zion/Indian Point (ZIP) Study.[1-3] The data so obtained
were subsequently adjusted to be identical to input data
used for melt/concrete interaction calculations performed
for the ZIP Study using the INTER[4] code and an initial version
of the WECHSL[5] code.[3] The resulting set of input conditions
are presented in Table 1-1.

Table 1-1

Input Data for ZIP Sample Problem

(Indian Point 3, Sequence AB-δ, BCL data)

Reactor Cavity Geometry - Flat - Based Cylinder

- Cavity Radius   - 3.125 m
- Cavity Depth   - 3.0   m
- Radial Wall Thickness   - 1.375 m
- Basemat Thickness   - 1.38   m

Reactor Cavity Concrete - Limestone

- Composition: $CaCO_3$ - 0.80 w/o
       $Ca(OH)_2$ - 0.15 w/o
       SiO_2 - 0.01 w/o
       Al_2O_3 - 0.01 w/o
       H_2O - 0.03 w/o

- Density   - 2520 kg/m^3
- Melt Temperature   - 1473 K
- Heat of Ablation   - 2.7 x 10^6 J/kg
- Rebar Content   - 0.135 w/o

Molten Fuel - Initial Properties

- Composition:

	Species	Mass (kg)
Metals	Fe	1.119 x 10^5
	Cr	1.754 x 10^4
	Ni	9.744 x 10^3
Oxides	UO_2	9.789 x 10^4
	ZrO_2	2.573 x 10^4

- Temperature - 2550 K

Decay Heat Generation in Melt Phases - Power Histories

Time (s)	Metallic Phase Power (MW)	Oxidic Phase Power (MW)
0	5.061	22.70
3605	3.126	18.59
7200	2.295	16.82
21603	1.752	13.09
32406	1.539	11.80

Atmospheric Pressure - 3.3265 x 10^5 Pa

The second task was begun by identifying the parameters to be varied in the study and setting up a systematic schedule of calculations based on a factorial design strategy. The six parameters identified as primary variables for the purpose of this study are (1) initial core melt composition (metallic and oxidic species masses), (2) concrete composition, (3) decay heat generation in the melt, (4) initial melt temperature, (5) initial cavity radius, and (6) computation time-step size. The resulting variable matrix/calculation schedule is shown in Table 1-2. The first two parameters are held constant at their nominal values (those for the ZIP sample problem given in Table 1-1). Parameters 3 through 5 are evaluated at their nominal values and at upper and lower bounds selected on the basis of plant data and discussions with BCL and Sandia researchers. The last parameter, time-step size, is varied over what is optimistically believed to be a reasonable range. Although some initial calculations have been made, no significant results or conclusions are forthcoming at present.

An initial CORCON-MOD 0 sample problem calculation for the nominal ZIP input conditions has been made out to a time of 5400 sec (1-1/2 hr). Similar calculations using the INTER[4] and WECHSL[5] (initial version) melt/concrete interaction codes were performed for the same input

Table 1-2

Matrix of Variables Included in Sensitivity Study

RUN NO.	1	2	3	4	5	6	7	8	9	10
Initial Melt Composition (Metallic and Oxidic Species Masses)	NOMINAL VALUES* - CONSTANT									
Concrete Composition (Species Mass Fractions)	NOMINAL VALUES* - CONSTANT									
Decay Heat (% of Nominal)	Nominal*	Nominal*	-20%	+20%	-20%	+20%	-20%	+20%	-20%	+20%
Initial Core Melt Temp (K)	2550*	2550*	1800	1800	2800	2800	1800	1800	2800	2800
Initial Cavity Radius (m)	3.125*	3.125*	2.14	2.14	2.14	2.14	4.66	4.66	4.66	4.66
Numerical Time Step (s)	30	90	60	60	60	60	60	60	60	60

*Nominal values are those for the ZIP Sample Problem given in Table 1-1.

conditions as part of the ZIP study.[3] The CORCON results
for a number of parameters that characterize the interaction
process are presented in Figures 1-4 through 1-11. For
comparison purposes, WECHSL and INTER results (where
they exist) for the time variations in selected system
parameters are included in Figures 1-4 through 1-9. In
addition, the eroded cavity shape at 5400 sec is compared
with that predicted by WECHSL in Figure 1-11.

The CORCON-MOD 0 results must be considered preliminary
in view of the approximations and simplifications employed
in the initial version (see Section 1.2.2). Nevertheless,
the variations exhibited in the figures appear to have
the proper directions and reasonable magnitudes. Perhaps
the most significant observation to be made is that the
general trends of the CORCON variations are qualitatively
quite similar to those of the WECHSL predictions. In
spite of this, there are some noticable quantitative
differences between the two sets of variations, particu-
larly in the amounts of concrete eroded (Figures 1-9 and
1-11). It is premature to discuss or interpret these
differences here, however, because of the preliminary
nature of the CORCON results, and because no investigaton
has been made to determine the causes of the differences.
It is sufficient at this point to note the qualitative
comparison of CORCON with WECHSL.
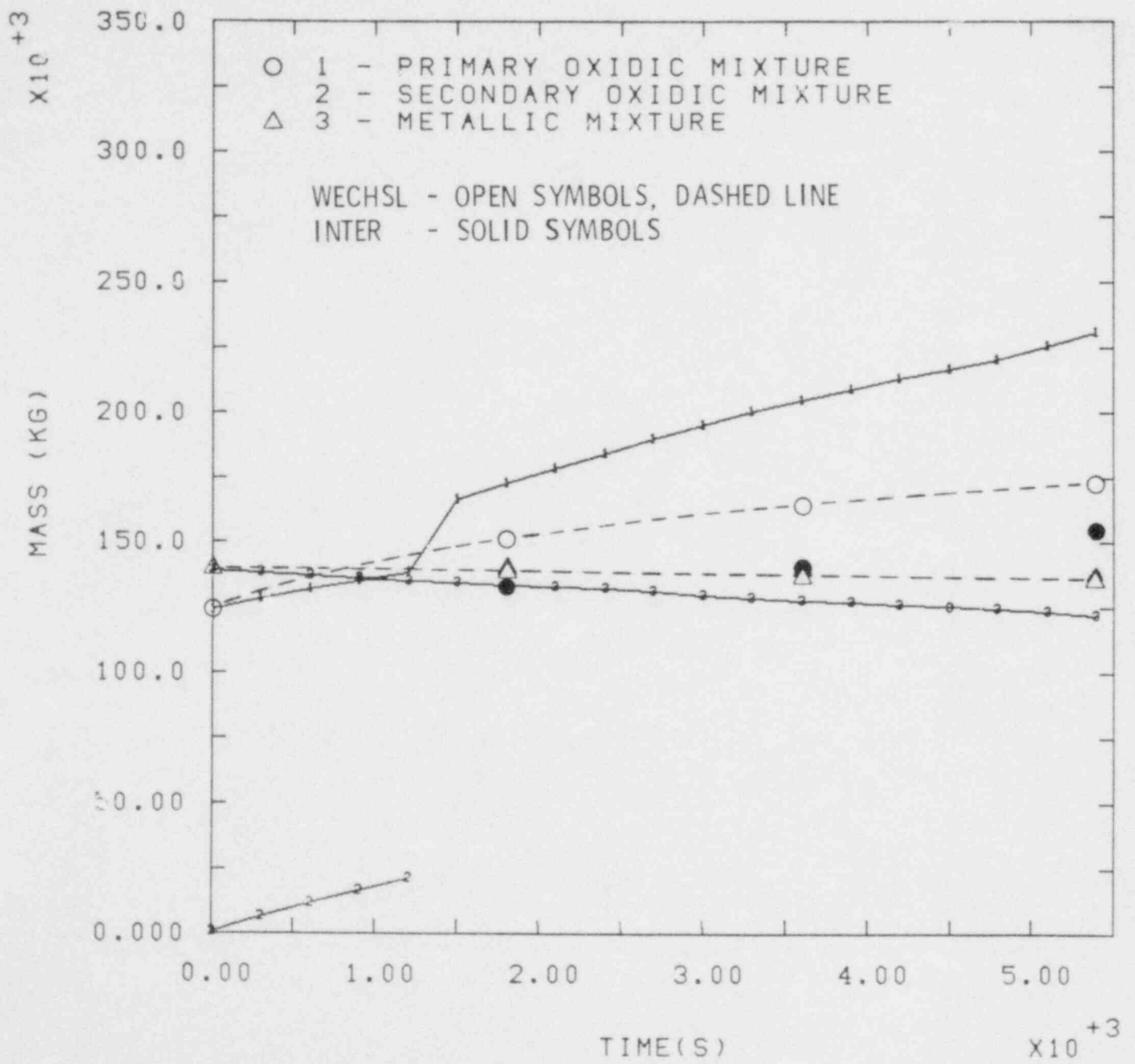
Figure 1-4. ZIP Sample Problem Calculation - Comparison of CORCON Layer Mass Histories with INTER and WECHSL Predictions
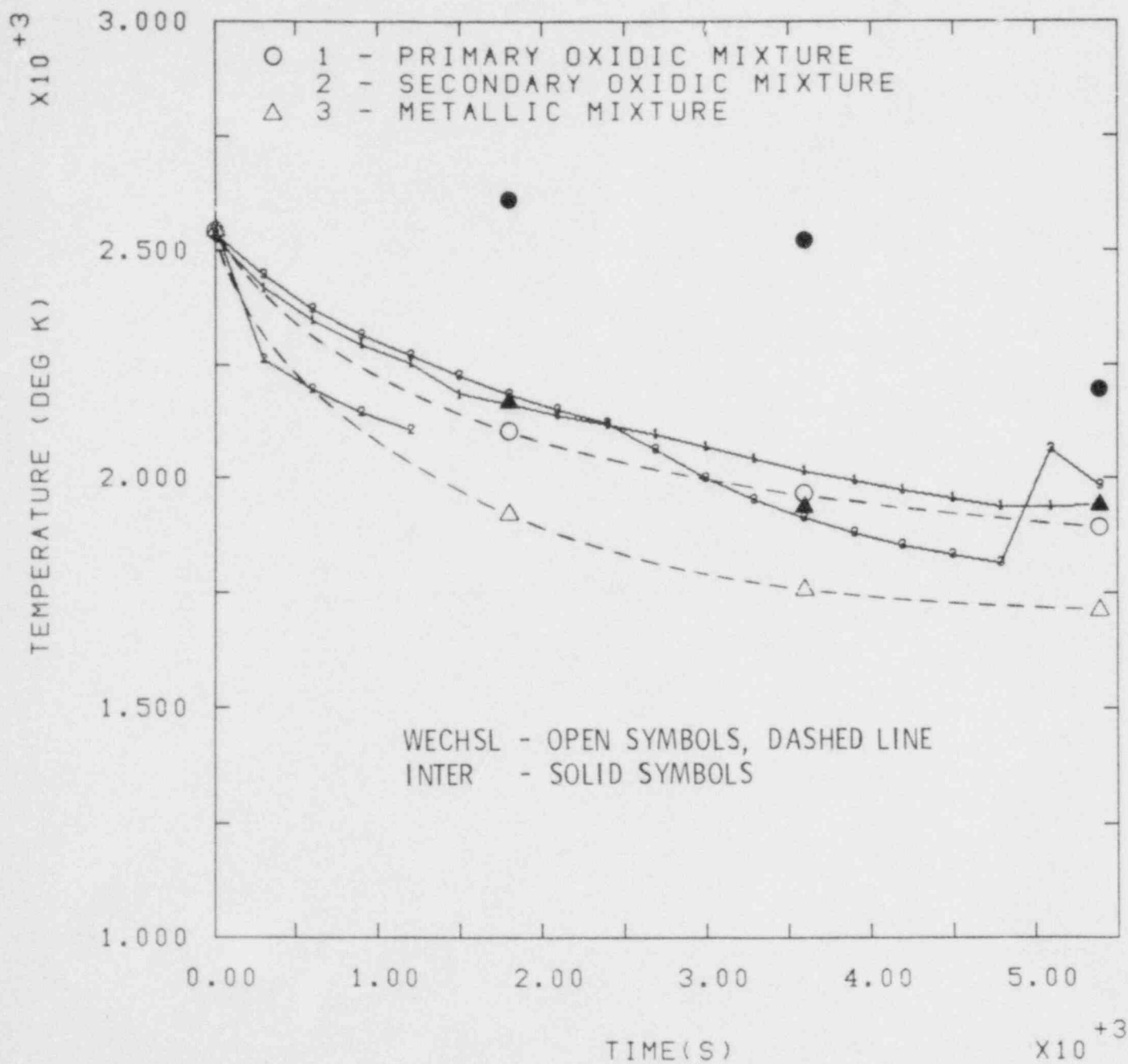
Figure 1-5.   ZIP Sample Problem Calculation - Comparison
of CORCON Layer Temperature Histories with
INTER and WECHSL Predictions
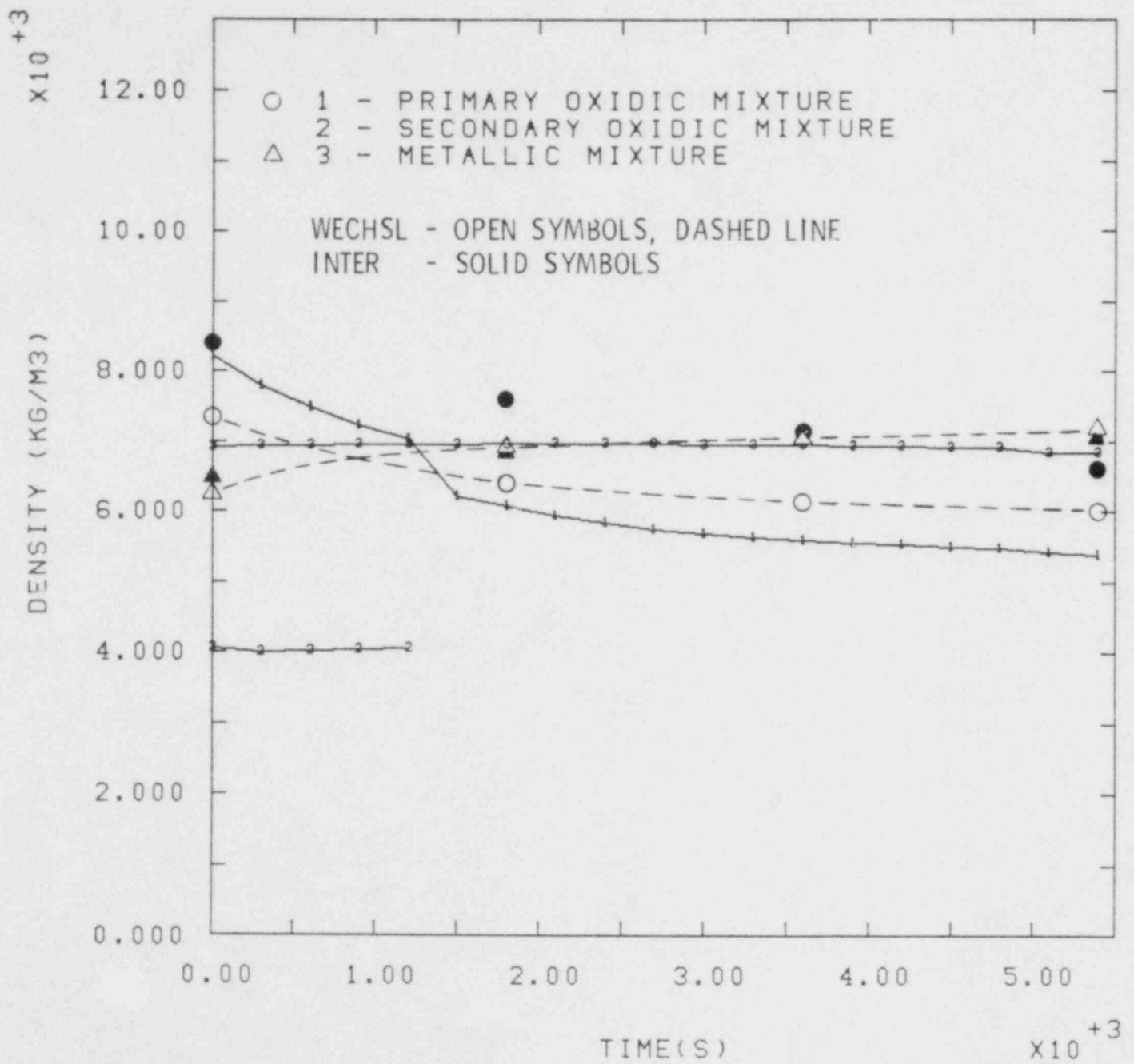
Figure 1-6. ZIP Sample Problem Calculation - Comparison of CORCON Layer Density Histories with INTER and WECHSL Predictions
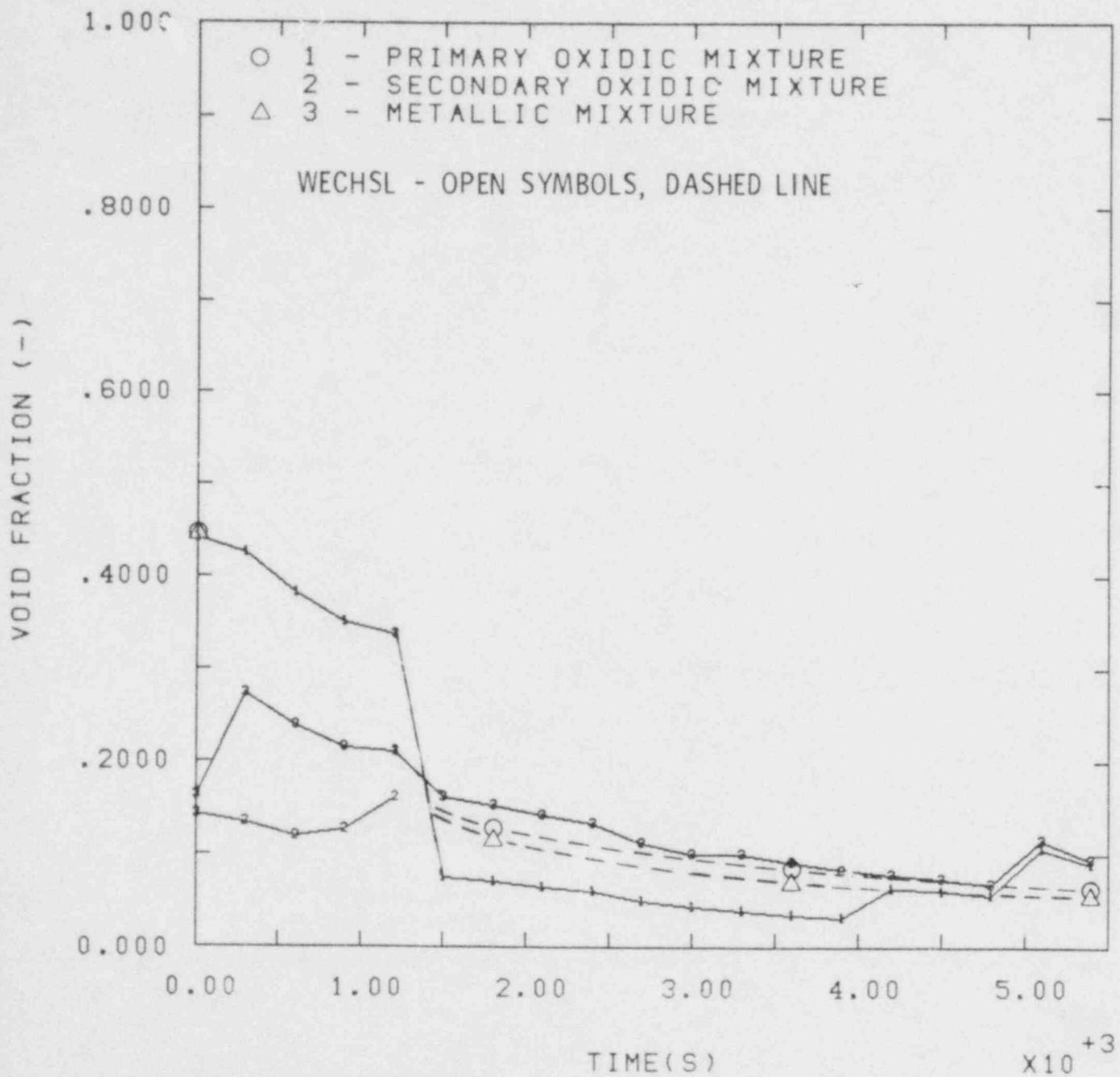
Figure 1-7. ZIP Sample Problem Calculation - Comparison
of CORCON Layer Void Fraction Variations
with WECHSL Predictions
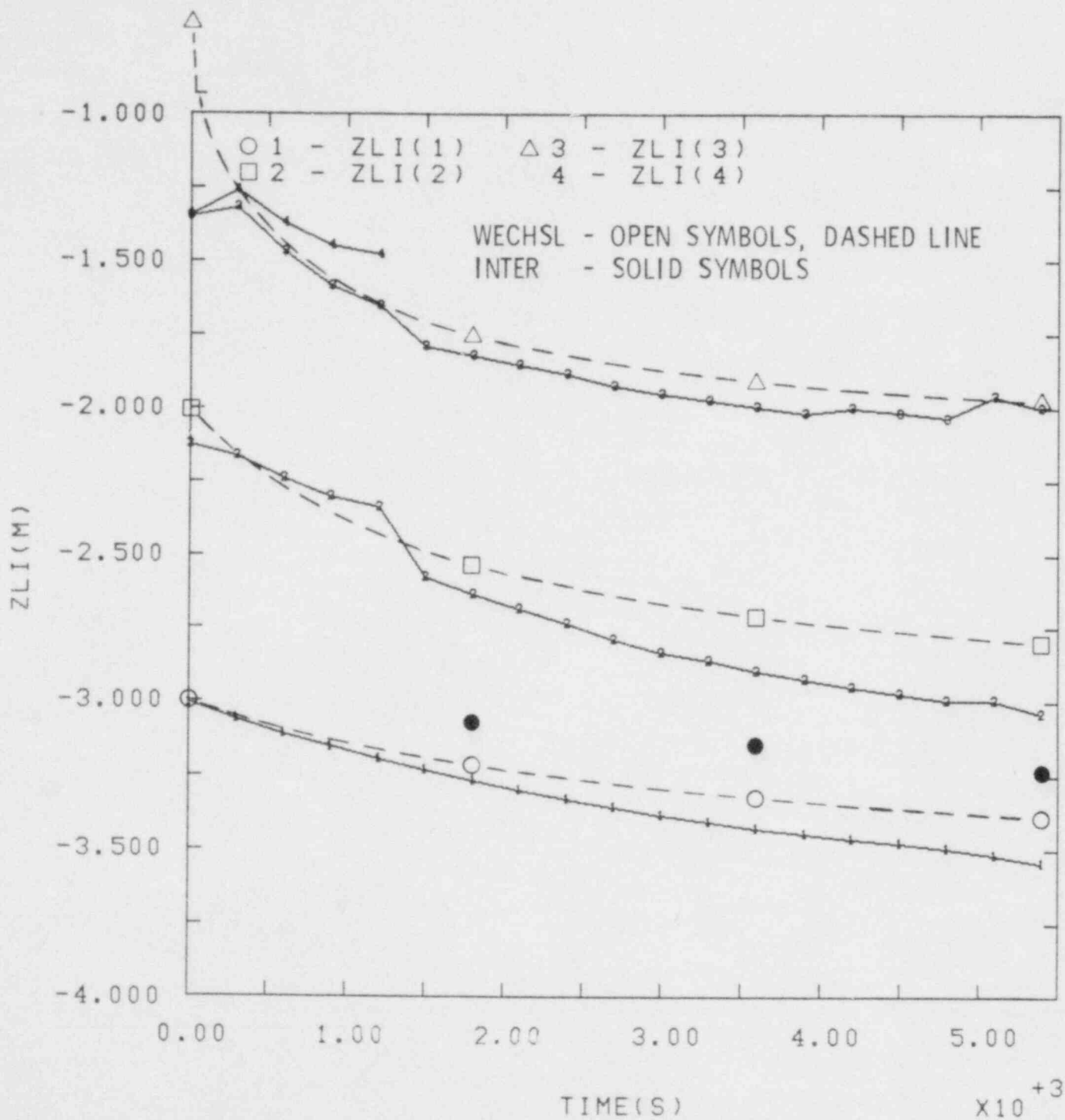
Figure 1-8. ZIP Sample Problem Calculation - Comparison of CORCON Pool Bottom, Top, and Layer Interface Location Histories with INTER and WECHSL Predictions
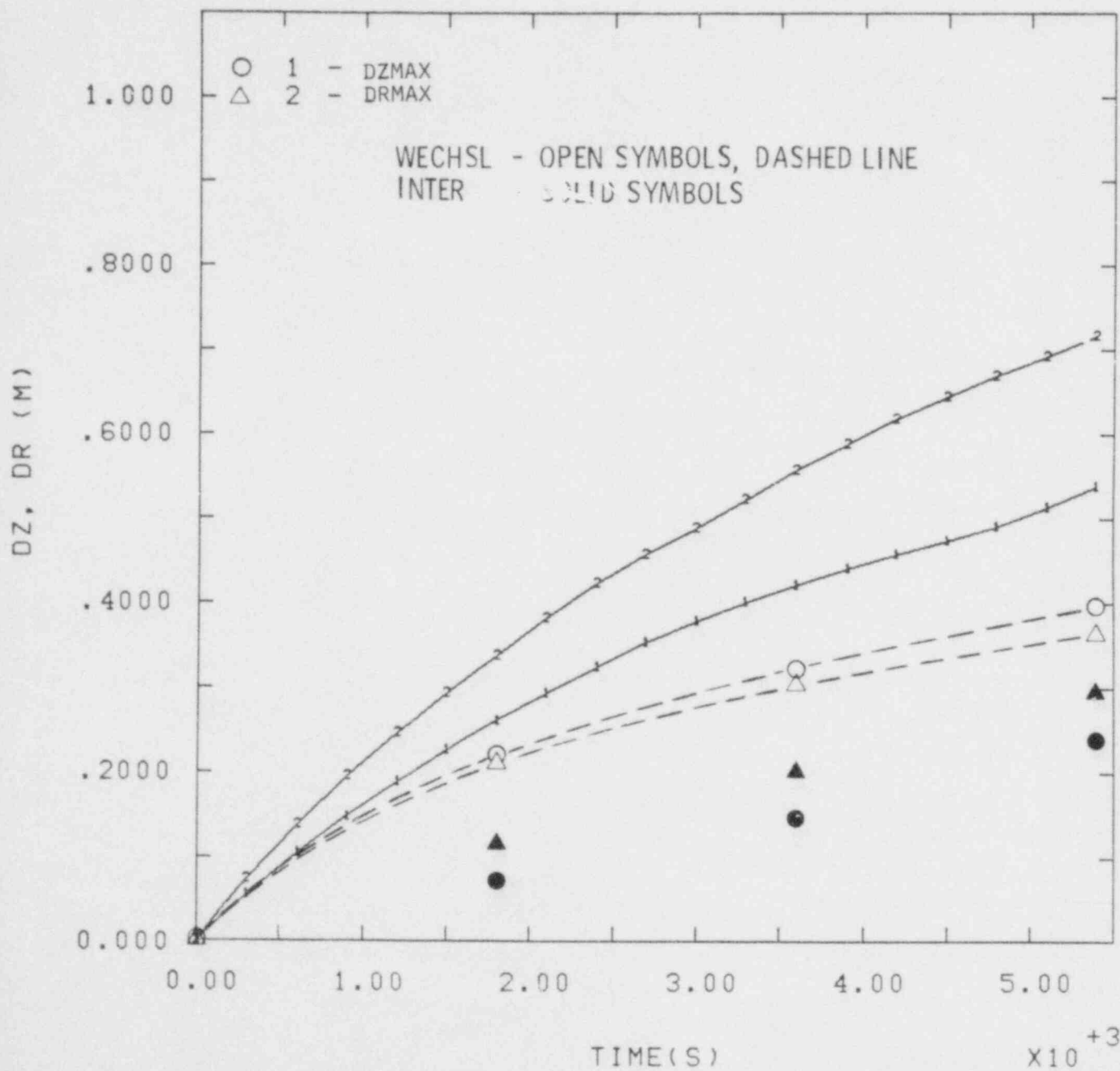
Figure 1-9.   ZIP Sample Problem Calculation - Comparison
of CORCON Maximum Vertical (DZ) and Horizontal
(DR) Pool Penetration Variations with INTER
and WECHSL Predictions

32
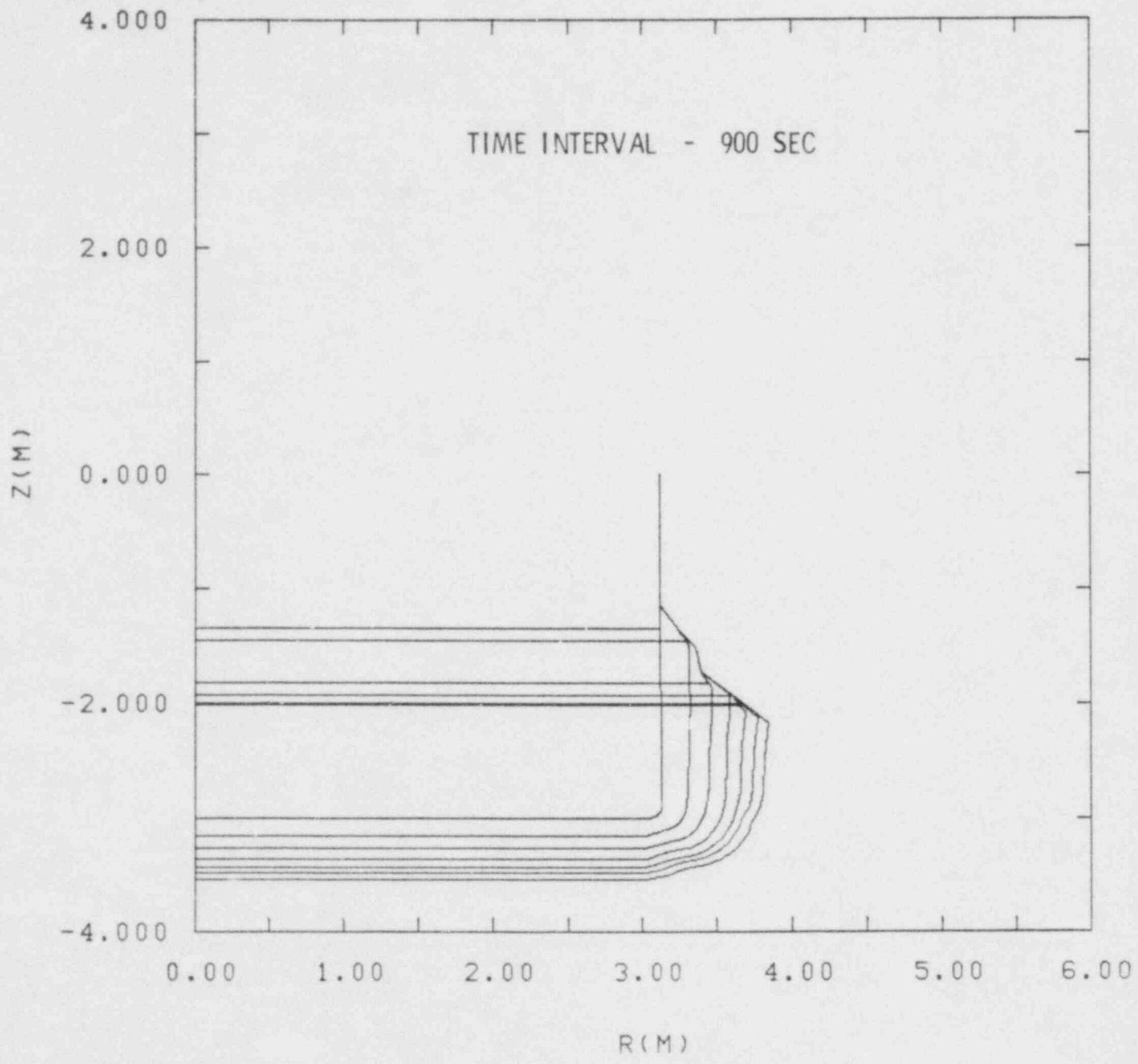
Figure 1-10. ZIP Sample Problem Calculation - CORCON
Prediction of Cavity Growth and Shape
Change with Time
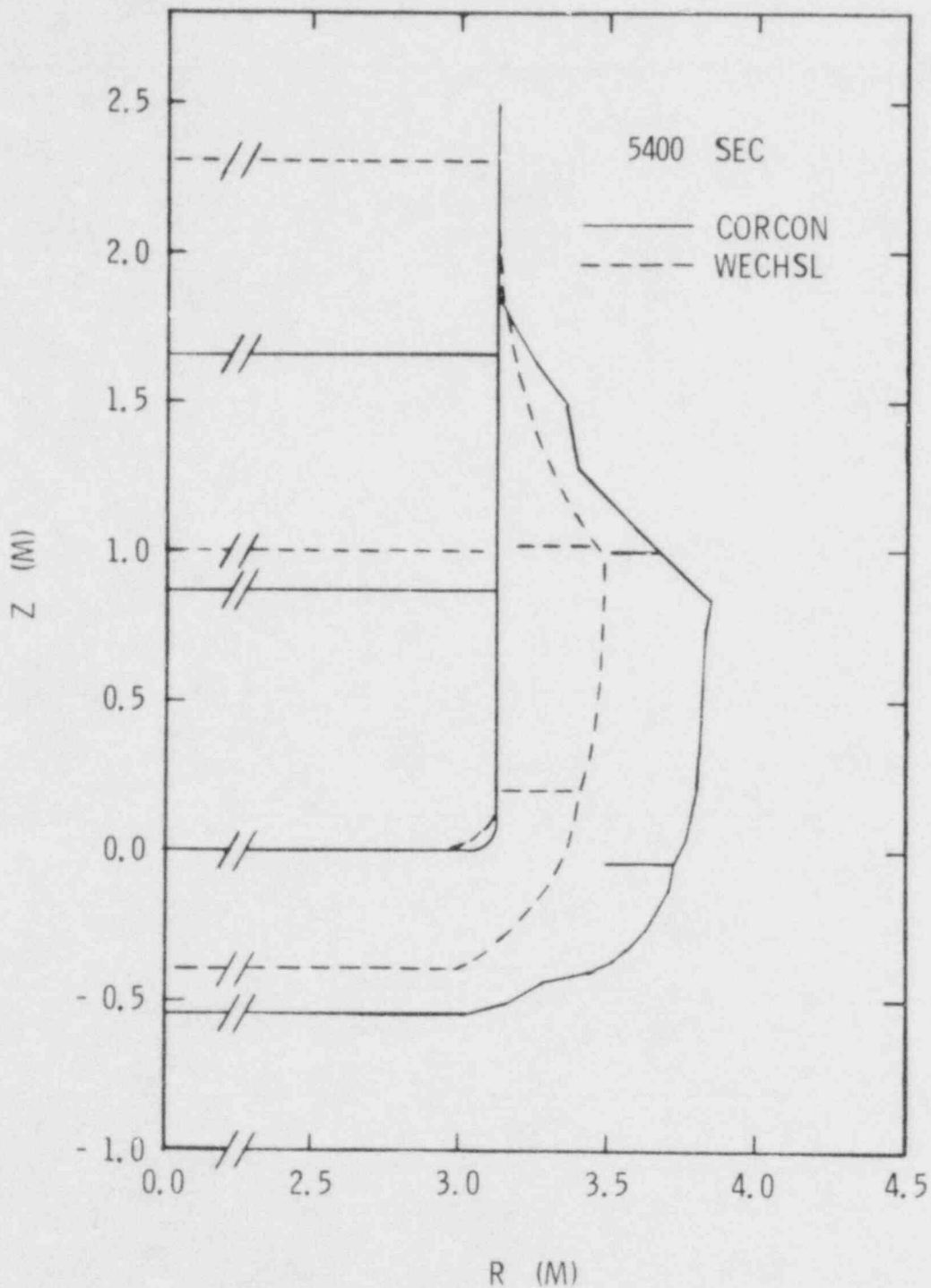
Figure 1-11.   ZIP Sample Problem Calculation - Comparison
of CORCON Cavity Shape at 1-1/2 Hours with
Cavity Shape Predicted by WECHSL

1.3 Experimental Program (D. A. Powers)

1.3.1 Code Comparison Tests

Two tests of sustained molten stainless steel inter-
actions with limestone concrete were conducted as part of
the code comparison effort. These tests, CC-1 and CC-2,
were sustained for 60 and 87 minutes, respectively, using
the inductive heating technique developed for the COIL
test series.[6] The objective of these tests was to provide
a comprehensive set of quality data as a basis for evalu-
ating the various computer codes developed for predicting
melt/concrete interactions. Comparison of the code
predictions with results of the tests will allow a judg-
ment of the state of development of the codes and the
models upon which they are based.

Much of the information necessary to make predictions
of the results of these tests has been presented in previous
quarterly reports.[7-9] A digest of this previously reported
information, along with input data for the predictions
that became available only after the tests were executed,
are presented in the following paragraphs.

As in the COIL series tests, melts of stainless steel
were prepared in an induction furnace. Once the melts
reached a temperature of 1970 $\pm$ 10 K they were teemed
into concrete crucibles. The initial weights of the

melts were 204 and 206 Kg for tests CC-1 and CC-2,
respectively.

The crucibles were fabricated from the so-called Clinch
River limestone concrete. This concrete contains little
silica and about 81 w/o calcium carbonate. Consequently,
when heated, the concrete yields large quantities of gas
(~ 250 ml/gm concrete at STP). The solid products of
concrete decomposition are quite refractory since the
solid residue is mostly CaO. The melting range of the
solid residue is estimated to be between 1700 K (solidus)
and 1870 K (liquidus). The heat required to raise the
concrete from room temperature to melting is about 3000-4000
J/gm-concrete.

The crucibles had flat based cylindrical cavities
33.1 cm in diameter and 38.1 cm deep. The crucibles were
equipped with embedded induction coils which were energized
at a nominal input power of 120 kW at 920-980 Hz. Power
losses were determined by the difference in coolant
temperature between the inlet and outlet to the induction
coils. The coolant consisted of a 50 v/o aqueous ethylene
glycol solution which flowed through the coils at a rate
of 284 cm^3/s.

The net input power to the melt in tests CC-1 and CC-2
is plotted versus time in Figures 1-12 and 1-13. The appar-
ent increased efficiency of power input early in the tests
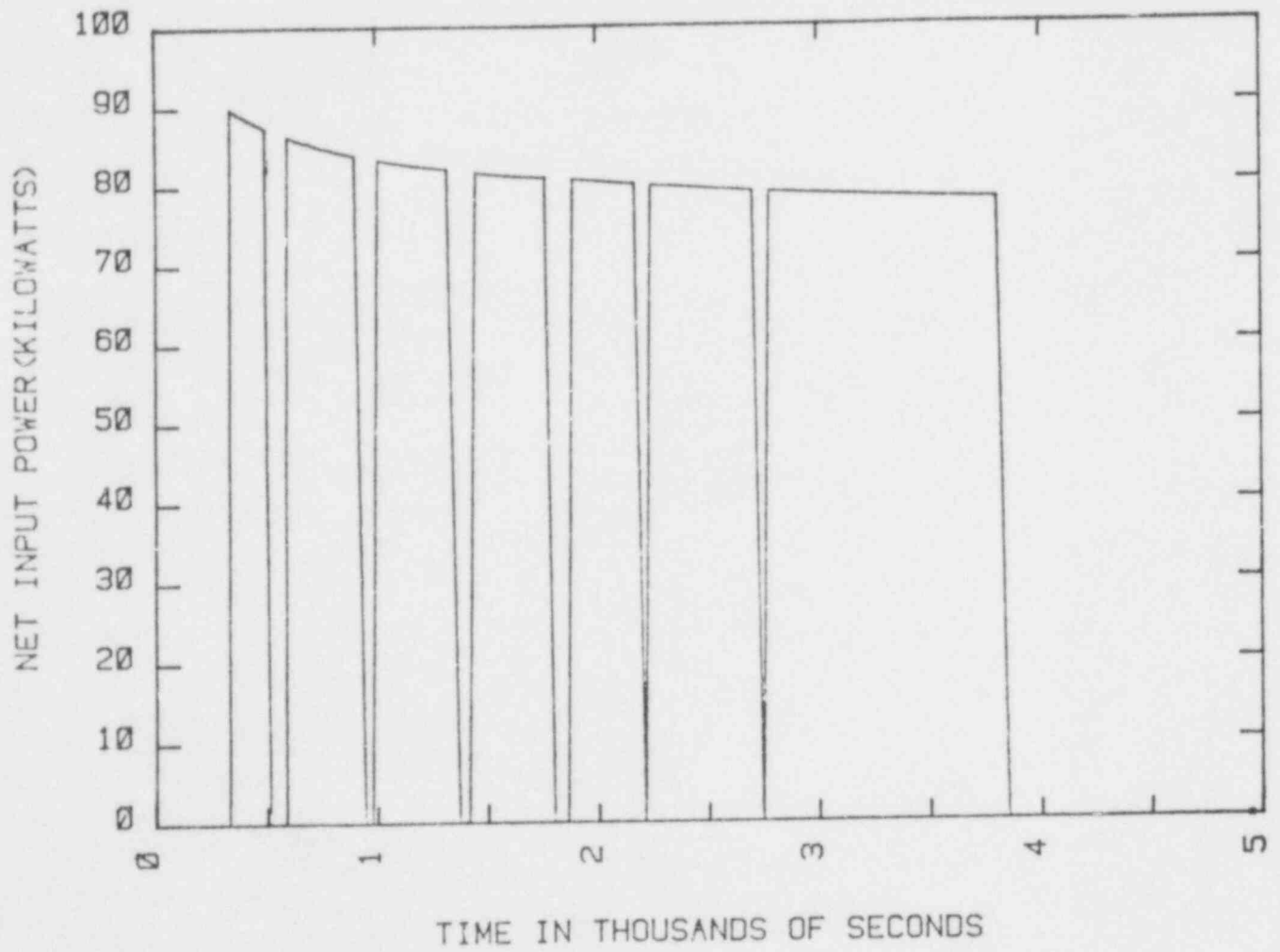
Figure 1-12. Net Input Power History for Test CC-1
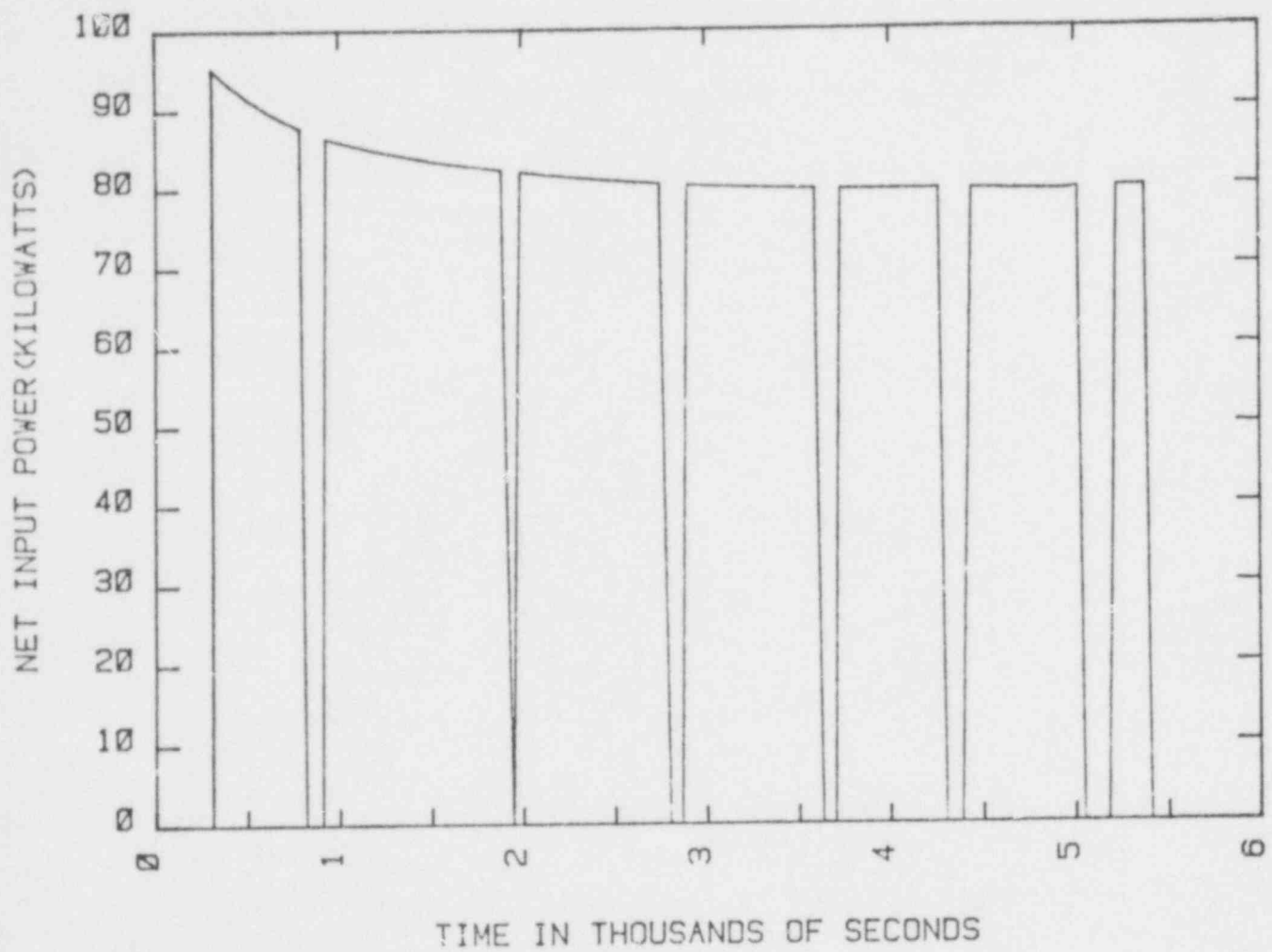
Figure 1-13. Net Input Power History for Test CC-2

may not be real. More careful analysis of the coolant temperature data is now underway to see if this behavior might be due to a systematic error in the way heat losses were computed.

The six interruptions that appear in the melt power histories were produced when the induction power supply was shut off, the instrumentation tower raised, and the melt temperature measured. During these interruptions, the melt surface was visually inspected for evidence of crust formation.

In both tests, the net input power to the melt reached an approximately steady value about 1800s after the start of the test. This steady state value indicated that the efficiency of power input was about 65 percent.

Data were collected during and after the tests for the specific features of melt/concrete interactions to be considered in the code comparison effort:

1. melt temperature history including time to solidification
2. concrete temperatures
3. rate and extent of concrete erosion
4. melt oxidation
5. onset of crust formation.

Melt temperatures were obtained primarily by immersion thermocouples. An optical pyrometer was also focused on the

surface of the melt. The melt temperature data collected in the two tests were of outstanding quality and showed good reproducibility.

A large amount of concrete temperature data was obtained in both tests from 43 type K thermocouples located about the crucible cavity, as illustrated in the top view of the cavity shown in Figure 1-14. Eleven thermocouples were arrayed at equal distances about 10 cm diameter ring centered on the axis of the cavity. The relative vertical locations of the thermocouples were fixed by a coplanar set of rings. The relative separations in depth of the 11 centerline ring thermocouples were:

TC	Relative Vertical Location (cm)	
1	0	← This TC is located
2	1.3	a small distance
3	2.5	beneath the initial
4	3.8	cavity bottom that
5	5.1	is yet to be
6	6.4	determined.
7	7.6	
8	8.9	
9	10.2	
10	12.7	
11	15.2	

A second set of eleven thermocouples were equally spaced about a 140 degree arc of a 26.6 cm diameter ring. The relative vertical locations of these thermocouples were the same as those given above for the centerline thermocouples. Twenty-one thermocouples were located along the walls of the crucible cavity. Three stations of thermocouples

TOP VIEW

CAVITY
PERIMETER

SCALE INTERVAL= 1 CM
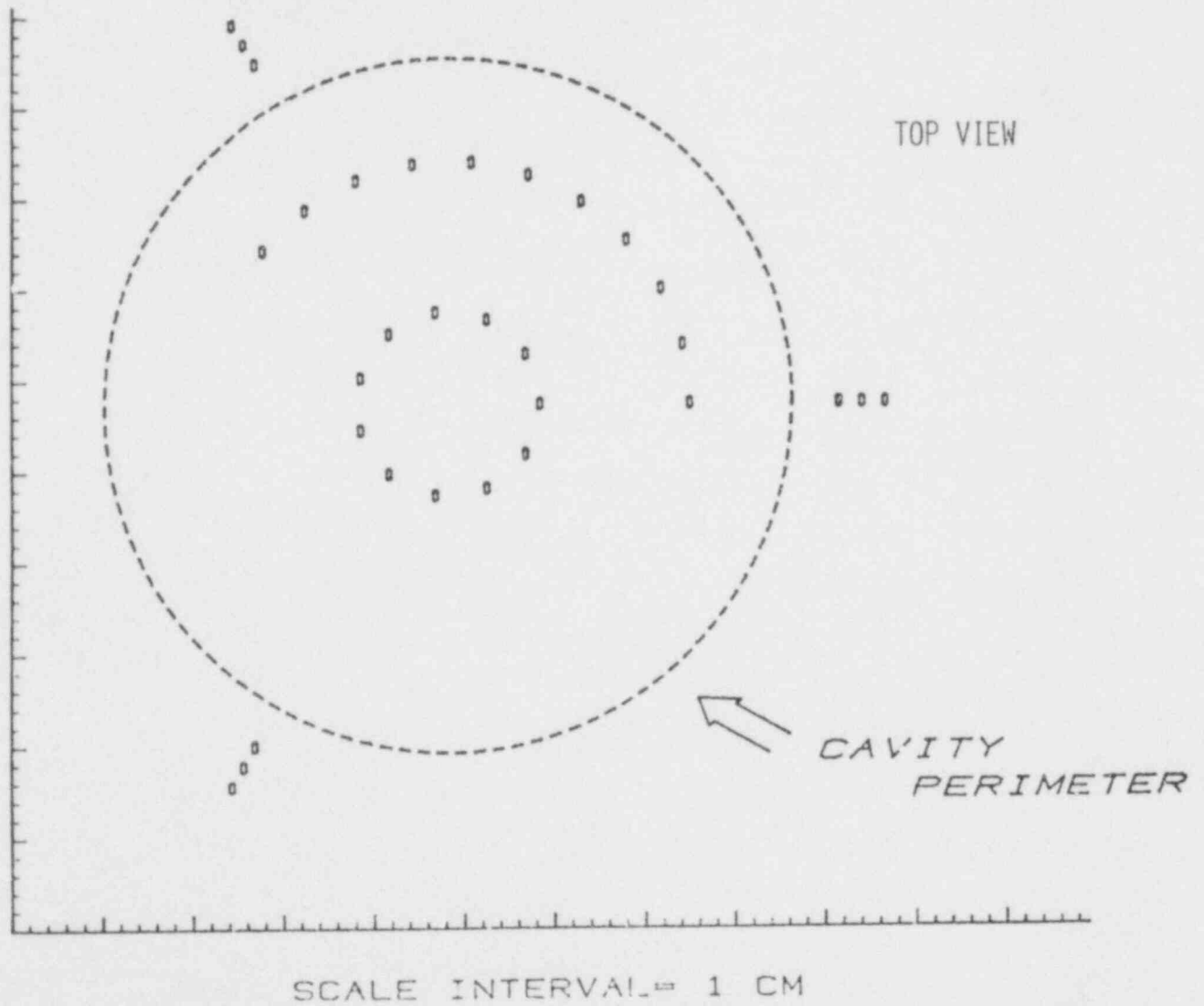
Figure 1-14. Thermocouple Locations for Tests CC-1 and CC-2

were installed 120 degrees apart around the circumference of the cavity. Within each of these stations, thermocouples were mounted at three vertical locations: level with the initial bottom of the crucible cavity, and at heights of 11.4 cm and 22.9 cm above the bottom. At each location, three thermocouples were located radially (horizontally) 2.5, 3.8, and 5.1 cm from the cylindrical walls of the cavity.

No information concerning the onset of crusting was obtained in the test. When the instrumentation tower over the melt was raised for the melt temperature measurements, no existing crust over the melt could be seen. However, a crust did begin to form once the tower was lifted, but it is unclear whether this was because of accentuated upward heat loss from the melt or because power to the melt was no longer being supplied. When the tests were terminated, a crust rapidly formed over the melt.

A variety of other data, beyond that required for the code comparison effort, were also collected during the tests:

1. gas generation rate

2. gas composition

3. aerosol composition

4. aerosol generation rate

5. moisture migration within the concrete

6. upward heat flux from the melt.

Gas flow data were collected pitot-statically, by a turbine flow meter, and by a pressure drop method. The three methods all yielded different results. It is not clear at present how these data should be interpreted.

Grab samples of the evolved gases have been analyzed and appear to be of good quality. Similarly, cascade impactor data for the aerosols seem to be of high quality. Attempts to make real-time measurements of gas composition and aerosol generation rate appear to have been only partially successful. The intensity of vibrations to the instrumentation tower and the heating of the sensors may have upset locations and calibrations of the devices used for these purposes.

Moisture sensors were located along the center line of the crucible cavity. The sensors consisted of a thermocouple, a pressure sensor and a four-point electrical conductivity bridge. As was observed in the COIL tests, the pressure transducers appear to have been the best indicators of the arrival of the dehydration front propagating through the concrete.

It is apparent that very detailed study of the raw data from the various instruments employed during the tests will be necessary before a consistent interpretation is possible.

1.3.2   Empirical Description of the Rate of Aerosol Generation

The interaction of molten reactor core materials with concrete is intense. Thermal decomposition of the concrete produces large quantities of gas. The combination of this gas sparging through the melt and the high temperatures of the molten material combines to form copious quantities of aerosol. The rate at which aerosols are formed has been monitored in large- and small-scale tests of melt/concrete interactions conducted at this laboratory. Optical transmission has been used to determine the concentration of aerosol in the gas stream evolved during melt/concrete interaction. We collected the aerosols to analyze their particle size and to determine their chemical composition with inertial cascade impactors.

Only a small portion of the data collected in tests of melt/concrete interactions have yet been analyzed. The early results of the data analysis have led to the following observations:

1. Aerosol concentration and hence, aerosol generation rate, at a fixed temperature is linearly proportional to the superficial velocity of gas sparging through the melt.

2. Aerosol concentration is a sharp function of melt temperature.

3. Aerosol concentration is not strongly dependent on concrete type.

4. The aerosol is composed of mostly non-fuel materials.

5. The aerosol particle-size distribution is sharply peaked at a mean aerodynamic particle size of 2 μm.

6. Chemical reaction plays an important role in aerosol production.

In the open test fixtures, aerosol concentration is an approximate measure of the aerosol generation rate if the rate of gas flow is known and aerosol sedimentation is not important. The flow configuration of the test apparatus is best suited for very high gas flow rates. At low gas flow rates considerable impaction and sedimentation of the aerosols are known to occur. Consequently, the observed aerosol concentrations at low gas flow rates are lower bounds on the true aerosol generation rate.

An empirical model describing the amount of aerosol produced during melt/concrete interactions was urgently needed for the Zion/Indian Point Study. To fill this need, data from one small-scale transient test of corium/concrete interactions and two large-scale sustained tests of molten stainless steel/concrete interactions were combined to yield an empirical correlation of the form

$$[A] = A_o \exp(-E/RT) \; (\beta V_s + \alpha)$$

where

$[A]$ = observed aerosol concentration (g/m^3)

R = gas constant (1.987 cal/mole)

T = melt temperature (K)

V_s = superficial gas velocity at standard
temperature and pressure (m/s)

A_o, β, α, E = empirical constants.

The data from the tests were sufficient to only algebraically
determine the empirical constants in the above expression
as follows:

$$E/R = 19000$$
$$\beta = 24$$
$$\alpha = 3.3$$
$$A_o = 10^5 .$$

No confidence intervals for the constants could be deter-
mined from the limited data set. Values of the aerosol
concentration predicted by the empirical correlation for
various melt temperatures and superficial gas velocities
are shown in Table 1-3.

The form of the empirical correlation is quite attrac-
tive. It takes specific recognition of gas velocity which
could impact aerosol formation by sparging, mechanical
shear, and as a reagent in chemical reaction. The effect
of temperature is recognized in an Arrhenius term that might
be typical for both vaporization processes or chemical
reactions. The activation energy determined by the empiri-
cal fit, 38 Kcal/mole, is consistent with either vaporiza-
tion or a chemical reaction and is totally inconsistent
with diffusion-limited processes.

Table 1-3

Aerosol Concentration

$$[A] = \exp(-19000/T)(24V + 3.3)10000 \ (g/m^3)$$

SUPERFICIAL GAS VELOCITY (m/s)

TEMP (K)	0.1	.03	.05	.07	.09
1573	0.32	0.60	0.87	1.14	1.41
1723	0.93	1.71	2.49	3.27	4.05
1873	2.24	4.13	6.01	7.90	9.79
2023	4.75	8.76	12.76	16.76	20.76
2173	9.09	16.74	24.40	32.05	39.71
2323	15.99	29.45	42.91	56.37	69.88
2473	26.25	48.36	70.47	92.58	114.69
2623	40.74	75.03	109.35	143.66	177.97
2773	60.28	111.04	161.81	212.57	263.33
2923	85.68	157.88	229.99	302.14	374.29

V = superficial gas velocity at STP (m/s)

T = absolute temperature (K)

A = aerosol concentration (s/m^3)

As further aerosol data are analyzed, they will be used to improve the empirical correlation. In particular an attempt will be made to improve estimates of the constants and to establish confidence bounds on these constants.

References

1. Private communication, R. Denning, Battelle Columbus Laboratories.

2. Private communication, W. B. Murfin, Sandia National Laboratories, Albuquerque, NM.

3. W. B. Murfin, compiler, Report of the Zion/Indian Point Study, Volume I, SAND80-0617/1 (Albuquerque, NM: Sandia National Laboratories, April 1980).

4. W. B. Murfin, A Preliminary Model for Core/Concrete Interations, SAND77-0370 (Albuquerque, NM: Sandia Laboratories, August 1977).

5. M. Reimann and W. B. Murfin, "Calculations for the Decomposition of Concrete Structures by a Molten Pool," PAHR Information Exchange Meeting, Ispra, Italy, October 10-12, 1978.

6. D. A. Powers, <u>Sustained Molten Steel/Concrete Interactions</u>
    <u>Tests</u>, SAND77-1423 (NUREG/CR-1066) (Albuquerque, NM:
    Sandia Laboratories, June 1978).

7. <u>Light Water Reactor Safety Research Program Quarterly</u>
    <u>Report October-December 1978</u>, SAND79-0820 (NUREG/CR-0768)
    (Albuquerque, NM: Sandia Laboratories, July 1979).

8. <u>Light Water Reactor Safety Research Program Quarterly</u>
    <u>Report July-September 1979</u>, SAND79-2290 (NUREG/CR-1162)
    (Albuquerque, NM: Sandia Laboratories nd) to be published.

9. <u>Light Water Reactor Safety Research Program Quarterly</u>
    <u>Report October-December 1979</u>, SAND80-0927 (Albuquerque,
    NM: Sandia Laboratories nd) to be published.

2. Steam Explosion Phenomena

The purpose of the steam explosion phenomena program is two-fold: (1) To identify experimentally the magnitudes and time characteristics of pressure pulses and other initial conditions which are necessary to trigger and to propagate explosive interactions between water and molten Light Water Reactor (LWR) core materials; and (2) to develop criteria to assess the probability and consequences of steam explosions during a hypothetical meltdown accident in an LWR. The major efforts in this program encompass four areas:

- Small-scale experiments using simulant molten materials (Corium A, E, Iron-oxide $\sim$ 0.1-10 gm) with water. These experiments are directed toward understanding the applied triggering pressures needed to induce a vapor explosion, and the conversion of heat to work under a variety of initial conditions.

- A large-scale, closed-geometry, fully instrumented test series using induction generated melts (Iron-oxide, Corium-E $\simeq$ 1-25 kg) dropped into water. These experiments are directed toward observing at large scale and with prototypic melts the thermal

to mechanical energy conversion ratio and propaga-
tion of the explosion as a function of fuel and
coolant temperatures, mass ratios, and compositions.

• Theoretical analysis of steam explosions. This
theoretical work is aimed at helping to interpret
the observed experimental results in light of past
theories and models of steam explosions (vapor ex-
plosions) and supplying additional modeling effort
w.ere past work has proven inadequate. The ultimate
objective is to be able to relate these experiments
and the results obtained to the possible behavior
of a steam explosion during a meltdown accident using
consistent modelling and scaling analysis.

• Assessment of containment failure resulting from
steam explosions. This work is directed toward
evaluating how a steam explosion might lead to
containment failure via missile generation or other
mechanisms, and to identify and evaluate the realistic
mechanisms that could dissipate the explosion energy
and reduce the probability of containment failure.

2.1 Summary

A brief summary of the research accomplishments during
the second quarter of fiscal year 1980 is presented in the
following sections.

2.1.1 Small-Scale Experiments

Steam explosion triggering experiments using single drops of molten iron-oxide were continued this quarter. Careful attention is being paid to overall reproducibility and the accuracy of diagnostics. Explosions have been triggered with bridgewires using 2.7 mm iron-oxide drops. Extensive data have been gathered, including high magnification, high speed films, calibrated pressure histories, and quantitative debris collection.

This quarter we have made a special effort to characterize the bridgewire pressure trigger. In addition, preparations are underway to use the newly developed electromagnetic impulse generator to produce the pressure transients. Finally a joint international interpretive exercise sponsored by the Committee on Safety in Nuclear Installations (CSNI) has been started using data from these experiments.

2.1.2 Fully Instrumented Test Series

During this quarter four major tasks were completed:

Two additional EXO-FITS experiments (MD series) were successfully conducted, producing spontaneous explosions with a 2 kg melt.

Photometric data from the earlier MD experiments were analyzed.

The FITS experimental chamber and facility were checked out and made operational.

The first in-vessel FITS experiment, FITS1A, was
performed 3 weeks ahead of schedule; all the
systems functioned properly and a mild
spontaneous interaction resulted.

2.1.3 Phenomenological Modeling of Steam Explosions

During this quarter, we modelled
the core meltdown phase, made estimates of the maximum
work potential from a steam explosion, and analyzed the
EXO-FITS tests using a recently developed transient 1-D
propagation code. Preliminary analysis for the first task
suggested that the core meltdown would proceed in a manner
similar to that assumed in WASH-1400, Appendix VIII, where
channel plugging and fuel freezing would allow a large
molten fuel mass to develop. For the second task, we
developed a simple model to determine the maximum work
potential due to a steam explosion for a variety of initial
conditions. Finally, we made progress in the modelling of
the EXO-FITS tests using a new transient propagation code.

2.1.4 Assessment of Containment Failure

Using a range of realistic estimates for the work
potential from a steam explosion, structural analyses similar
to those outlined in SAND79-2002, indicate for the Zion-Indian
Point Study:

1. Contrary to WASH-1400 assumptions, generaton of large mass missiles (e.g., reactor vessel head) due to in-vessel steam explosions seems unlikely.

2. Explosions could generate small mass missiles (e.g., control rod drive assembly) with velocities of the order . 100 to 400 m/s; however, it is unlikely that these missiles could penetrate both the control rod missile shield and the containment.

2.2 Small-Scale Experiments (L. S. Nelson)

2.2.1 Laser-Melted Drops of Iron Oxide

The initial scoping experiments which were performed last fiscal year with molten iron oxide were continued. These experiments are expected to produce theoretically tractable explosive interactions with melts that have properties similar to those that are encountered in a light water reactor core melt situation. In these experiments, a 350 W (maximum) continuous-wave carbon-dioxide laser was used as the sole heat source for the molten oxide.

Pendant drops of molten iron oxide were prepared from high purity iron. The deionized water used for the interaction was boiled and cooled rapidly prior to the experiment, in order to minimize dissolved gas.

Weighed iron samples were heated and oxidized in air with the beam of the carbon dioxide laser, while an iridium wire was used to support the sample. At equilibrium, a pendant drop of composition $O/Fe = 1.30 \pm 0.03$ (determined by weight gain) was produced. The drop was released into the water by an upward tug on the iridium wire using a solenoid.

We photographed the interactions at high speed (two framing cameras operating at 5000 to 7000 frames per s). Pressures generated during the interaction were measured with a calibrated lithium niobate pressure gage; the output was recorded simultaneously on both a slow and a fast digital oscilloscope (4016 points each at $5\ \mu s$ and $0.5\ \mu s$ per point). Drop temperatures at release time were recorded with an optical pyrometer which operates in the near infrared region. Debris was separated from the water by filtration through a filter paper under suction. A photograph of the current experimental apparatus is shown in Figure 2-1.

As in the earlier scoping experiments, vigorous explosions were obtained with the molten iron oxide drops by applying bridgewire-generated triggering transients with peak pressures of ~ 1 MPa.

Excellent data are being gathered via the high-speed films recorded at two magnifications. These films may be
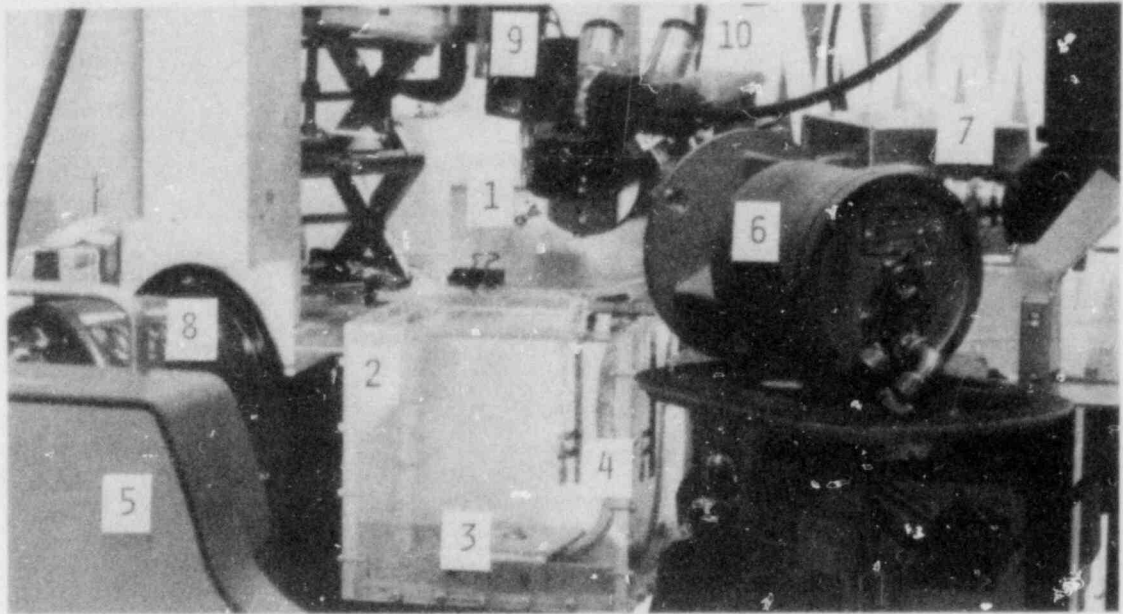
Figure 2-1. Photograph of Experimental Setup for Steam Explosion
Studies with Single Drops of Molten Iron Oxide (10-76-2)

1. $FeO_{1.3}$ drop hanging on iridium wire held in small
chuck (disregard larger spherical object below and
to the left of the drop; it is part of the
microscope).

2. Polymethylmethacrylate water vessel. It is
cubical, 150 mm on a side internally.

3. Exploding wire held in stainless steel base plate.

4. Lithium niobate pressure transducer.

5. High-speed camera focused on drop explosion
location.

6. Pyrometer focused on drop during melting.

7. Lens of carbon dioxide laser.

8. Quartz-iodine photographic lamp.

9. Solenoid mounted on 3-dimensional positioner.
Activation of the solenoid releases the iron
oxide drop.

10. Microscope (10X) for viewing drop during
laser melting.

correlated frame by frame with the pressure traces recorded on the oscilloscope. The films show a luminous drop that descends through the water with an image diameter about a millimeter larger than the drop diameter. This is caused by the boiling film that surrounds the drop. When the bridgewire fires about 0.1 s after immersion, the drop image begins to expand luminously and spherically within about 200 μsec (one frame). As the image expands, two concentric spherical fronts can be seen moving outward, the outer being an aggregate of small brightly luminous particles, and the inner a bubble with some fragmented debris. Eventually the bubble begins to shrink, leaving the front of luminous particles several millimeters from the center. As the inner spherical bubble collapses a pressure pulse is generated causing a secondary explosion of the tiny suspended drops. The bubble then alternately collapses and grows several times, all surrounded by a cloud of black debris particles suspended in the water. These oscillations are anticipated from hydrodynamic theory.

As the molten drop enters the water, it pulls behind it a tiny bubble of air about three times the drop volume. This was not observed in the scoping experiments where the fall distance was $\approx$ 1 cm compared to $\approx$ 4 cm in these experiments. It is felt that this tiny gas bag above the drop can modify the explosive behavior. Steps are being taken to use shorter fall distances to minimize this complication.

When correlating the pressure records with the behavior
of the drop and debris, it can be seen that a pressure
pulse is produced in the water each time a bubble collapses
in the chamber. This can be either the steam explosion
bubble or the bubble that surrounds the bridgewire; both
show cyclic collapse and reinflation behavior.

Efforts are underway to replace the bridgewire as a
pressure transient generator. An electromagnetic impulse
generator has been constructed to produce planar shock
waves that travel upward in a water tank similar to the one
shown in Figure 2-1. Electromagnetic repulsion between
parallel conductors is used to produce the impulses. A
schematic diagram of the apparatus is shown in Figure 2-2.
It will be tested soon.

Preparation is also underway to distribute sets of
data produced in the molten iron oxide drop experiments
among the dozen laboratories which have indicated interest
in participating in the joint interpretive exercise sponsored
by the Committee on Safety in Nuclear Installations (CSNI).
This will involve the delivery of high speed films, pres-
sure data and other descriptive material to each of the
participants.

2.2.2 Pressure Transient Characterization

The characterization of the pressure transients
generated when bridgewires are exploded under water has
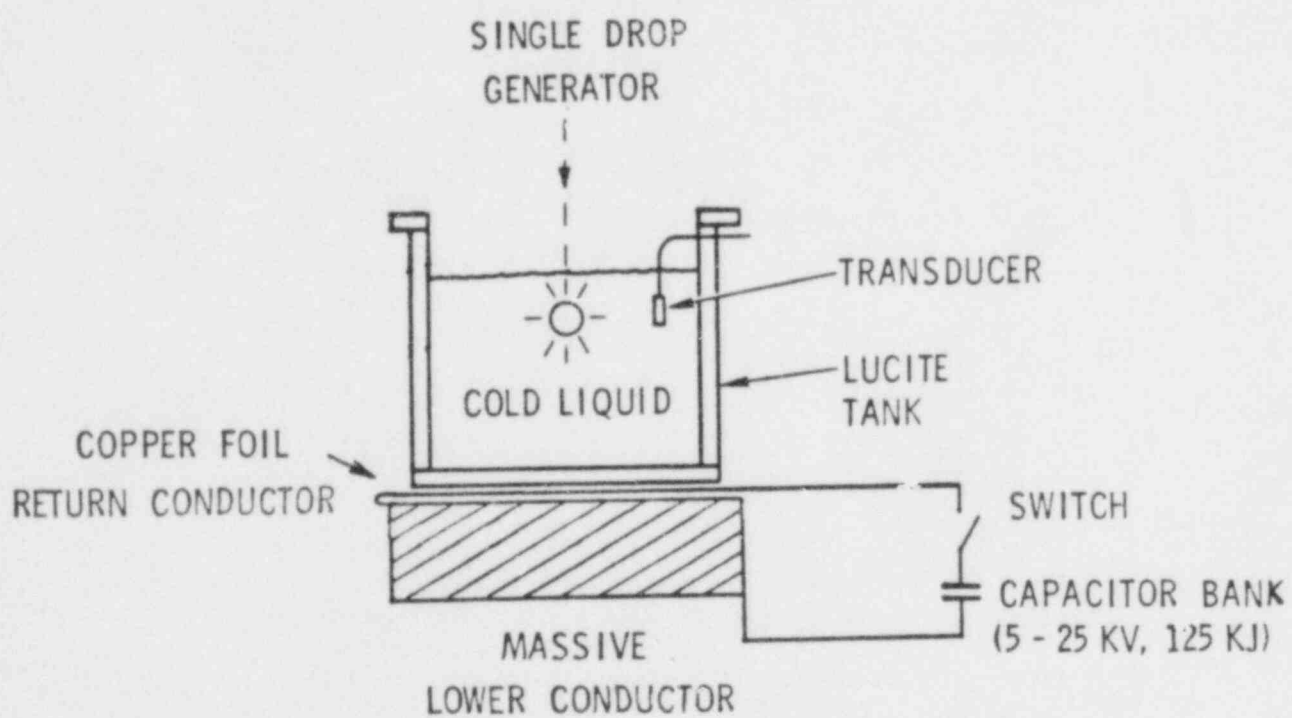
Figure 2-2. Schematic Diagram of Electromagnetic Impulse
Generator for Producing Planar Shock Waves

continued this quarter. The outputs of the bridgewires were recorded with a pair of lithium niobate pressure transducers placed as shown in Figure 2-3. Additional recording was done with high speed photography.

Considerable effort was expended to eliminate noise in the electrical signals produced by the lithium niobate gages. This involved extensive shielding of the circuitry, and recording the transducer traces using two Kistler Model 504D416 amplifiers and two Nicolet Explorer III oscilloscopes; all four were powered with an isolation transformer. The amplifiers and oscilloscopes were operated in a floating mode, independent of local grounding. Pressure traces were recorded on both fast and slow oscilloscopes (0.5 and 5 μs per point). It was shown that pressure transients on the order of 1 MPa and 50 μs wide were produced at the location of the drop at the time initiation was to be started. Typical pressure records at the two transducer locations (see Figure 2-3) are reproduced in Figure 2-4.

An attempt was made to relate bubble dimensions to the electrical energy input into the exploding bridgewire. It was estimated that on the order of 10 percent of the electrical energy used to fire the bridgewire (7 μF at 2 kV) was converted into mechanical work as determined by the pressure-volume characteristics of the bubble as a function of time. Melt enthalpy-to-work conversions will be estimated
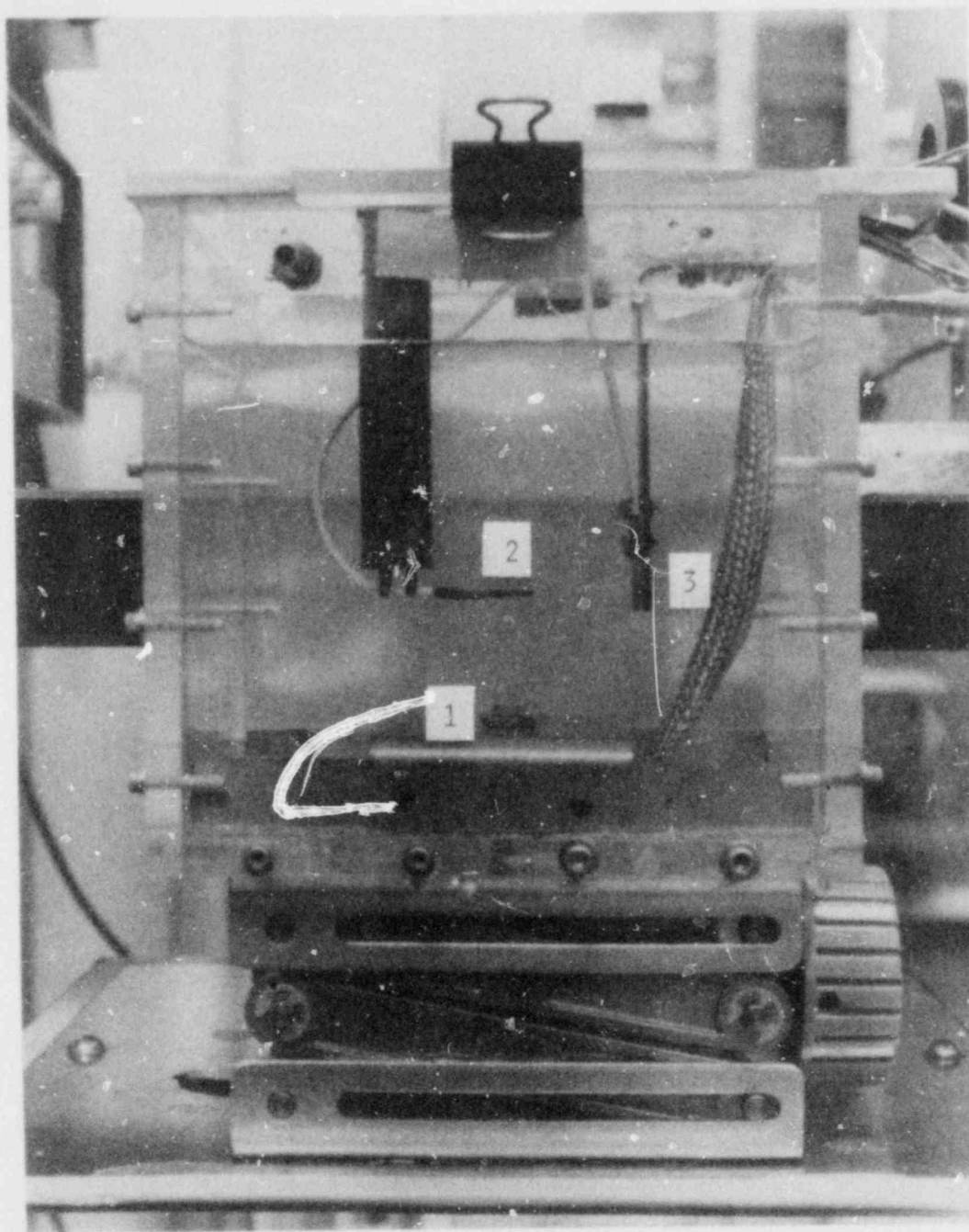
Figure 2-3. Arrangement for Studying Pressure Transients Generated by Exploding
a Submerged Wire (11-60-3)

1. Exploding wire held in stainless steel base plate.
2. Lithium niobate pressure, Transducer B, positioned with flat
   face downward, 29 mm directly above the exploding wire.
3. Lithium niobate pressure, Transducer A, positioned with flat
   face facing horizontally. The distance from the exploding
   wire to the center of the transducer is 45 mm.
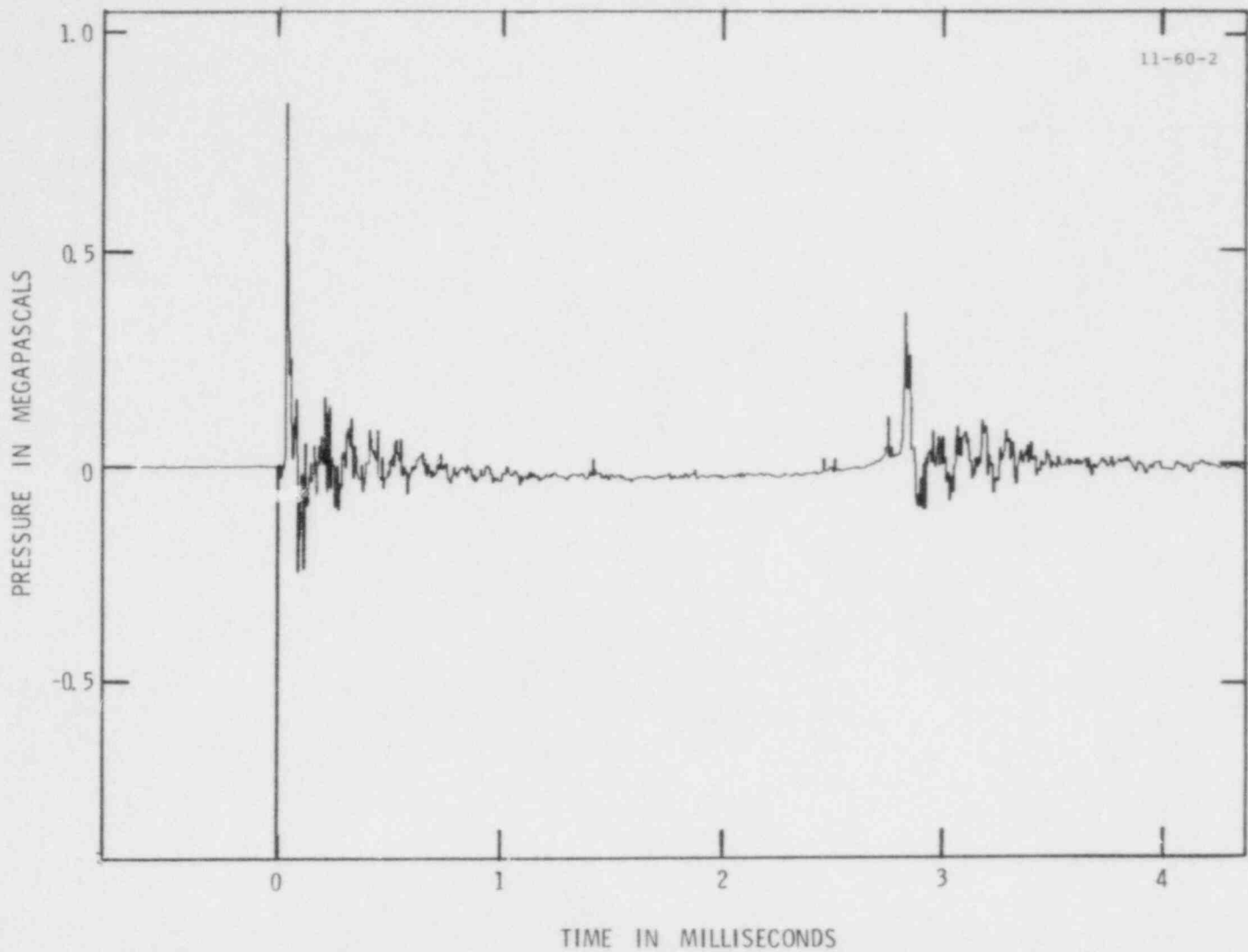
Figure 2-4. Typical Pressure Traces Recorded by Transducers Placed as Shown in Figure 2-3

a. Trace recorded digitally, 4016 points at 5 μs/point, using Transducer A.
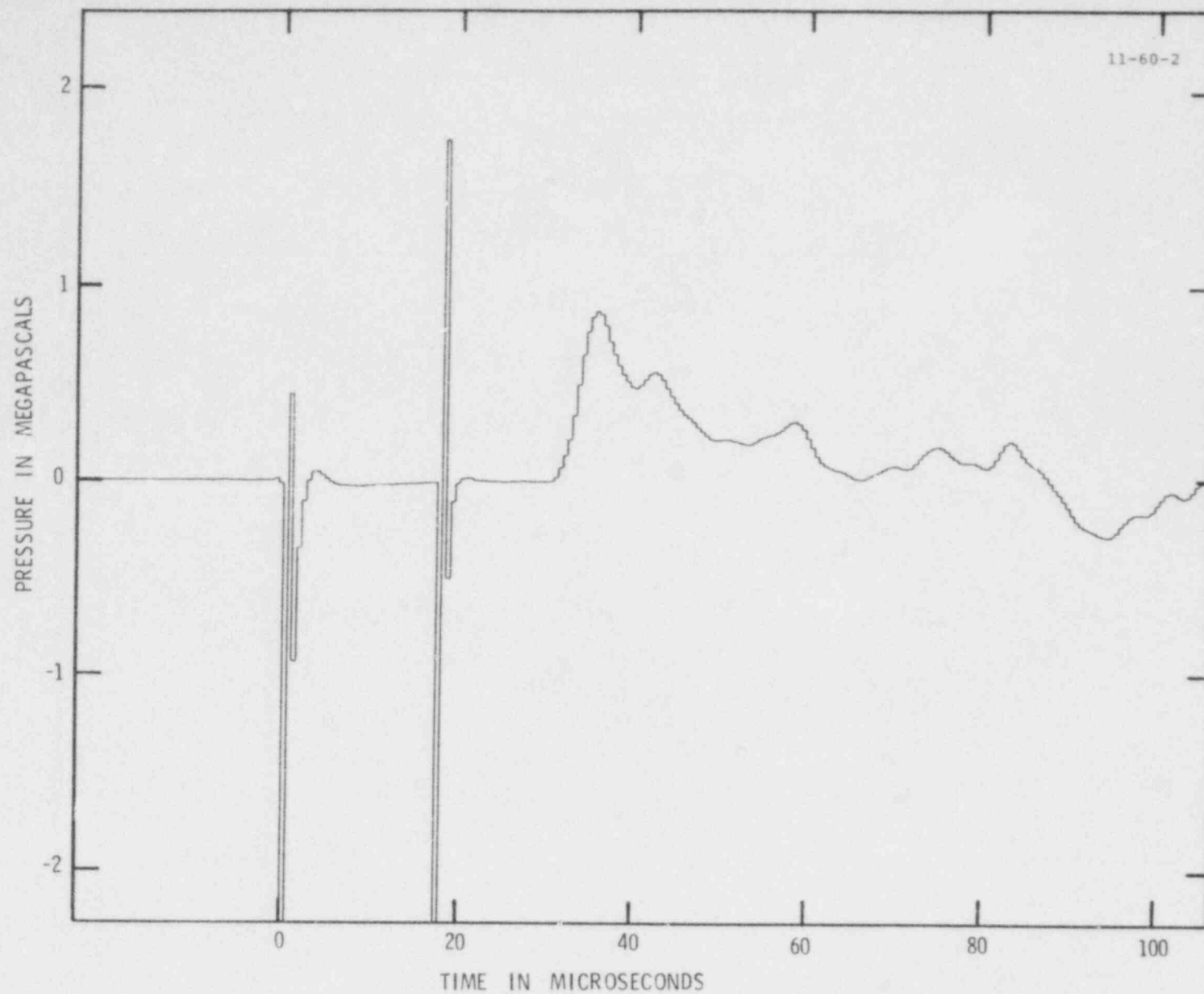
Figure 2-4 (cont'd). Typical Pressure Traces Recorded by Transducers Placed as Shown in Figure 2-3

    b.   Trace recorded digitally, 4016 points at 0.5 μs/point, using Transducer A. Signals prior to 20 μs are electrical noise and should be disregarded.
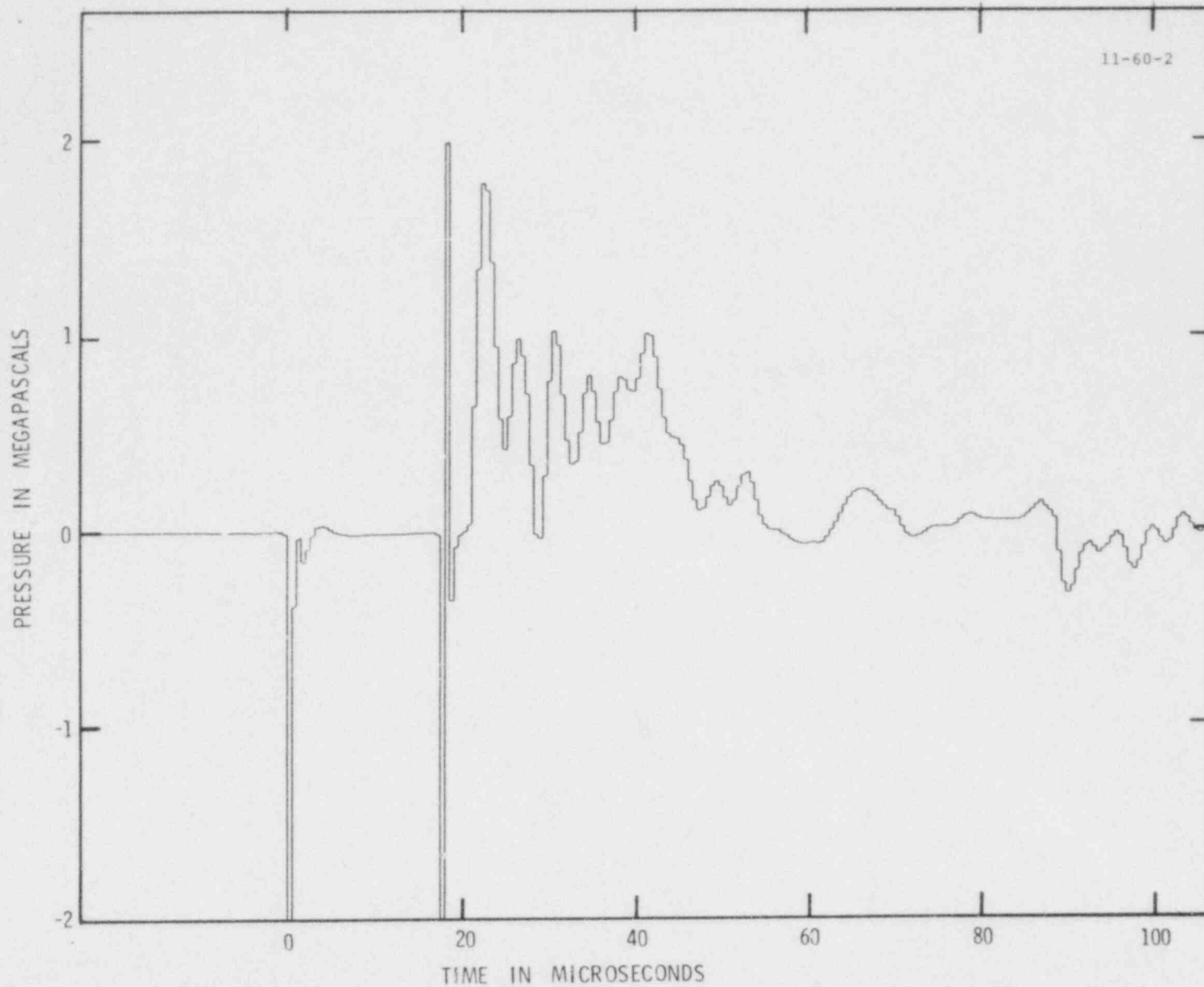
Figure 2-4 (cont'd). Typical Pressure Traces Recorded by Transducers Placed as Shown in Figure 2-3

    c. Trace recorded digitally, 4016 points at 0.5 μs/point, using Transducer B. Signals prior to 20 μs are electrical noise and should be disregarded.

in the same way in the single drop steam explosion experiments.

2.3 Fully Instrumented Test Series (D. E. Mitchell)

During this quarter the FITS facility was made operational. We conducted the first in-chamber experiment, performed two additional EXO-FITS experiments (MD series), and analyzed photometric data from the earlier MD experiments.

EXO-FITS experiments MD15 and MD16 were performed to determine the threshold melt spontaneously triggered explosions. This smaller fuel mass quantity could then be used in the first FITS experiment. These experiments used 2 kg quantities of thermite melt, and both resulted in spontaneously triggered explosions which exhibited the propagating thermal-detonation phenomena. The explosions were triggered at the chamber base.

The temporary instrumentation system used for these experiments did not function reliably, inasmuch as electrical noise generated during the experiment sequence made the data invalid. This noise may have caused the high pressures reported in the last quarterly, although the characteristics were somewhat different. Therefore, as in other MD experiments, high speed photography was used as the primary data source.

We used the information obtained from MD15 and MD16
to design the first in-chamber experiment, FITS1A. The
main objective of this experiment, conducted on March 18,
1980, was to serve as a system checkout. A 2.1-kg quantity
of thermite was used as the simulant. We recorded a total
of 15 data channels along with three high-speed and two
low-speed cameras. Photometric data indicated that a
small explosion resulted which was not as efficient was
the earlier 2 kg experiments MD15 and MD16. One possible
explanation for this behavior may be that the melt delivery
velocity was 20 percent higher than in the previous tests.
The in-chamber delivery system will need to be adjusted to
match EXO-FITS conditions, and this task is now underway.
Initial data showed that electrical noise from various
control functions and cameras was not a problem on this
experiment as it had been on earlier MD series experiments.
Static overpressure was found to be 0.083 bar and a tempera-
ture rise of 18°C was observed. Signal levels on other
transducers were very low because of the small explosion
that occurred. The experiment was successful inasmuch as
all systems functioned as intended. FITS1A will have to
be repeated when the delivery velocity adjustment is made.

This quarter, photometric data from the earlier MD
experiments were analyzed in greater detail. We obtained

data related to propagation velocity, melt column diameter, mixing time (time to explosion), and average fuel density. It was found that propagation velocity appears to be a function of fuel column diameter and average fuel density. The dependence of propagation velocity on these two variables suggests that thermal explosions can be modelled using methods similar to those used for chemical detonations.

Melt density and mixing may be important in determining threshold quantities for spontaneously triggered explosions. The data show that experiments near 2 kg are marginal as far as spontaneously triggered explosions are concerned, and if the mixing times (dependent in some way on melt delivery velocity and shape) are changed the threshold melt quantity could vary. This observation is substantiated by the results from FITS1A where entry velocity was 20 percent greater than the MD series experiments and only a partial reaction was observed.

2.3.1 Developmental Experiments

Threshold Experiments - Two experiments, MD15 and MD16 were done this quarter to determine the threshold melt quantity to be used in the FITS experiments. These experiments used 2 kg quantities of thermite melt dropped into 90 kg of water at 10°C. The water was contained in a clear lucite chamber as in earlier experiments in this

series. Both experiments resulted in spontaneously trig-
gered explosions. Average propagation velocities for
these explosions were 249 m/s for MD15 and 429 m/s for
MD16. The differences may be due to the melt column diameter
at the time of the explosion. The effect of this diameter
on propagation velocity is discussed later in this report.

Electrical noise generated during the experiment sequence
invalidated the active data. High-speed photography (7200
frames/sec) was used to observe the interactions.

MD Series Data Analysis - Photometric data from experi-
ments MD7 through MD16 were analyzed in greater detail than
previously reported. Detailed study of the films showed that,
for all experiments that result in explosions, some evidence of
a propagating reaction could be observed. These propagation
velocities were measured along with average melt column
diameter at the time of explosion. The results are plotted
in Figure 2-5 where it can be seen that propagation velocity
seems to be dependent on the diameter of the melt. If one
assumes that this behavior is similar to chemical explosives,
a failure diameter and infinite charge diameter velocity
can be empirically determined

$$V_D = V_\infty (1 - \frac{a}{d}) .$$

where d is the melt diameter, V_∞ is the infinite charge
diameter propagation velocity, a is the failure diameter,
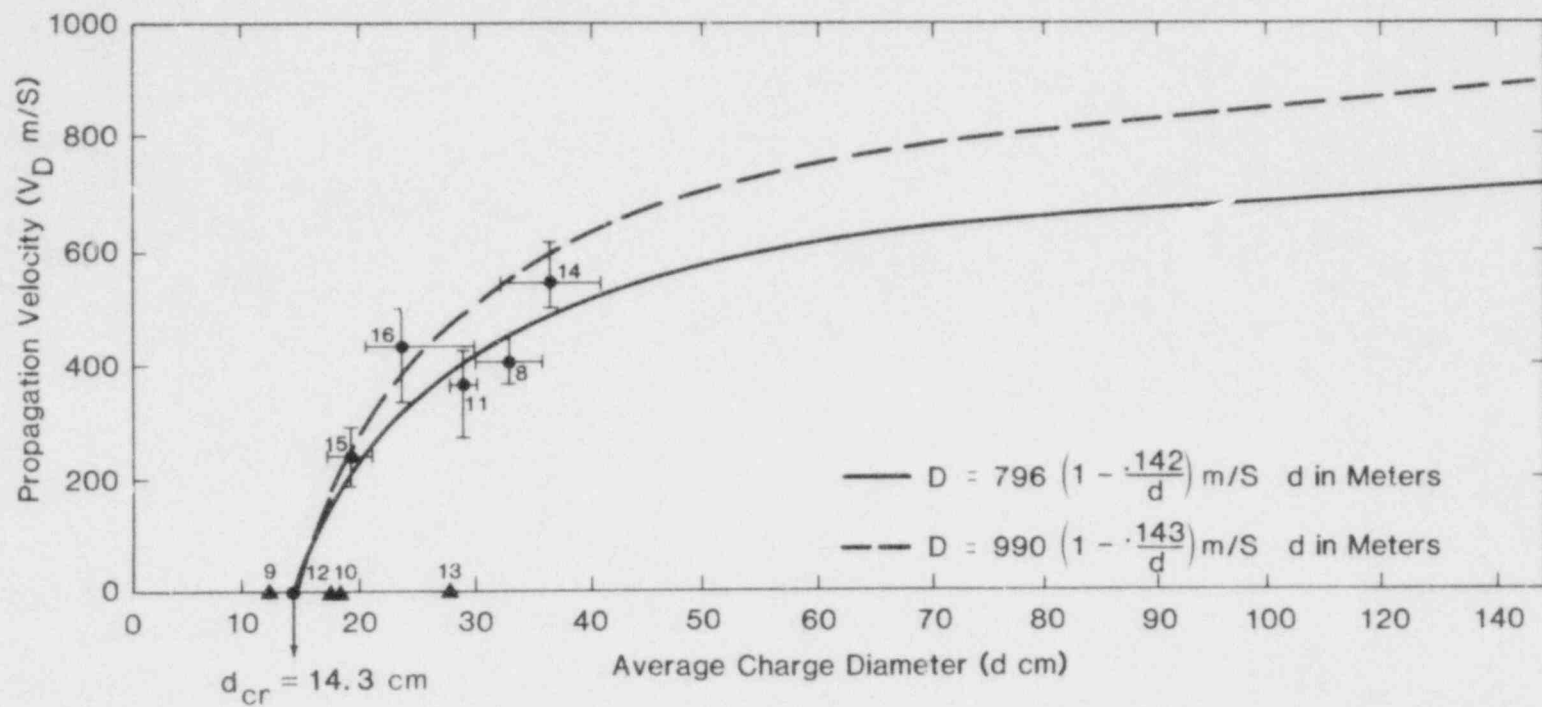
Figure 2-5. Propagation Velocity versus Average Melt Diameter for Thermite Experiments under Ambient Conditions

and using the data shown in Figure 2-5, the values obtained
for a and V_∞ are

$$0.142 < a < 0.143 \text{ meters}$$
$$796 < V_\infty < 990 \text{ m/s} \quad .$$

Figure 2-5 shows that, with the exception of MD13, all the
data tend to support this observation; i.e., propagation
velocity is in some way dependent on melt diameter.

Figure 2-6 shows propagation velocity as a function of
apparent fuel density at time of explosion. This fuel
density is defined as mass delivered divided by the mixture
volume occupied by the melt prior to the explosion. This
definition is analogous to assuming that the relative volume
fraction of coolant liquid to vapor is constant for all the
experiments. The average melt column diameter is used
along with an estimate of the length of the column for
volume calculations. The height of the column is less
certain than the diameter because it is somewhat cooler and
cannot be observed as easily as the diameter. The figure
shows that as the density increases the velocity decreases
and propagation probably can only occur over a range of
apparent fuel densities. The same effect of fuel density
is shown in Figure 2-7 where response (either explosion or
no explosion) is plotted versus fuel density for all the
experiments performed in the MD series. The figure also
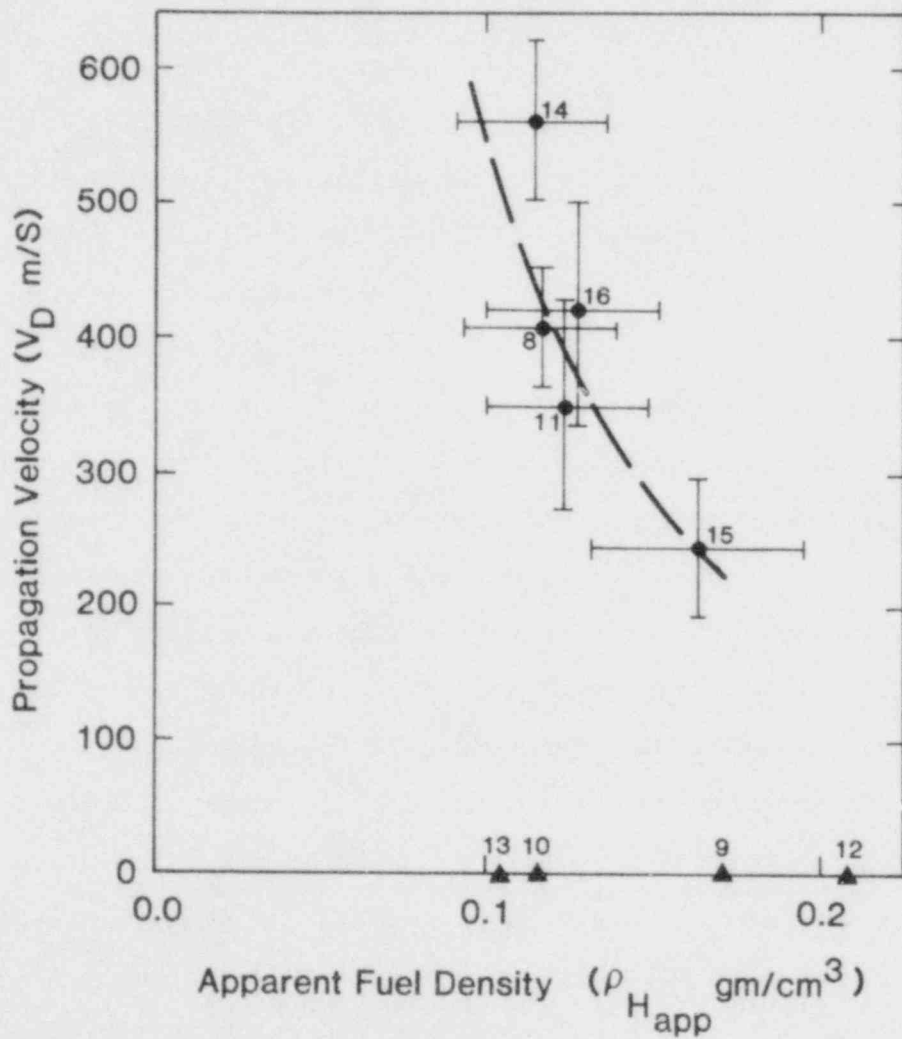
Figure 2-6.   Propagation Velocity versus Apparent Fuel Density
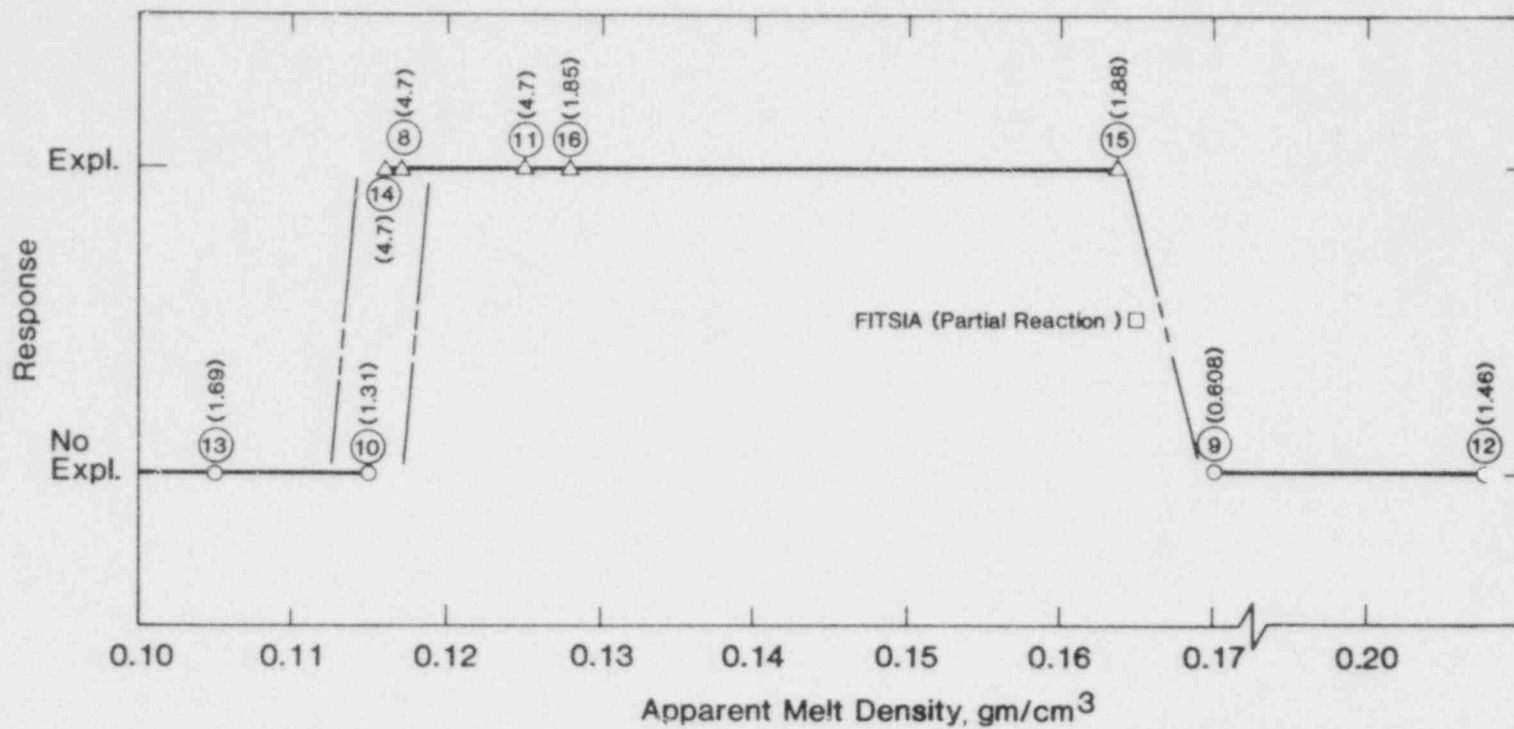
Figure 2-7. Response versus Average Fuel Density at Time of Explosion or Base Impact

shows that explosions occur when the density of the fuel
is between ~ 0.115 and 0.169 gm/cm^3. The numbers for
density that are quoted are average values and in reality
there is a density gradient both axially and radially in
the melt column. The results from FITS1A are also shown
and indicate that for this simulant a 2-kg quantity is
marginal as far as spontaneous explosions are concerned.

A simple relationship between fuel density and response
probably does not exist because time to achieve a critical
density compared to melt cooling time, for example, must
also be considered. Figure 2-8 shows response as a function
of mixing rates. Mixing rate is determined by two experi-
mentally measured quantities: the initial quantity of melt
delivered and the dwell time for the melt either to explode
or impact the chamber bottom for those experiments that
did not explode. A trend similar to that shown for fuel
density is observed with the exception that MD13 shows a
failure to explode in the density plane although it should
have exploded as indicated in the mixing rate plane. This
failure to explode in either plane indicates that both of
these parameters may be important in looking at the sensi-
tivity of those materials to spontaneous initiation. Similar
behavior is seen for experiment MD10 where, in the mixing
rate plane, failure is expected and in the melt density
plane, a marginal condition exists. FITS1A results show
similar behavior to MD13.
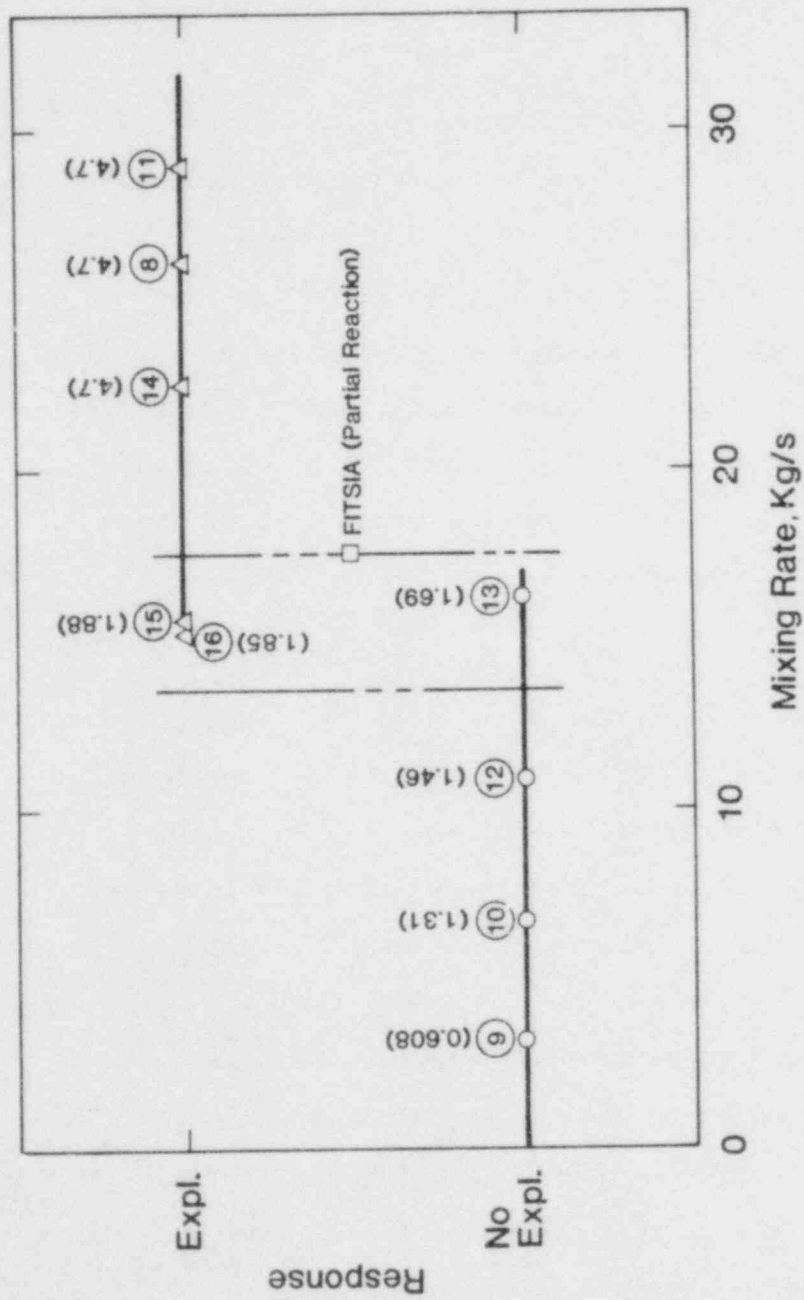
Figure 2-8. Response versus Mixing Rate

75

Further experiments in the MD series are planned to
study the effect of mixing rate on sensitivity to sponta-
neous explosion and the effect of melt diameter on propaga-
tion velocity.

The importance of these parameters is that if the
relationship between melt diameter, density, and propaga-
tion velocity is valid, then steam explosion behavior can
be modelled in a manner similar to that for detonating
chemical explosives. The input parameters required for
equation of state definition in those types of calculations
are the detonation velocity, the density, and the ratio of
specific heats. For steam explosions, the ratio of spe-
cific heats is similar to ideal gases.

2.3.2 FITS1A

The first in-chamber experiment (FITS1A) was conduc-
ted on March 18, 1980. The objectives of this experiment
were to evaluate the performance of the melt delivery,
chamber closure, and instrumentation systems and to deter-
mine the response of the chamber to a steam explosion
loading.

Figure 2-9 describes a typical FITSA experiment and
Figures 2-10 through 2-12 show the FITS1A experimental
assembly. The experiment parameters are given in Table 2-1.

In addition to the above instrumentation five cameras
were used to observe the interaction and chamber; three
high-speed (7000 frame/s) and two real-time cameras.
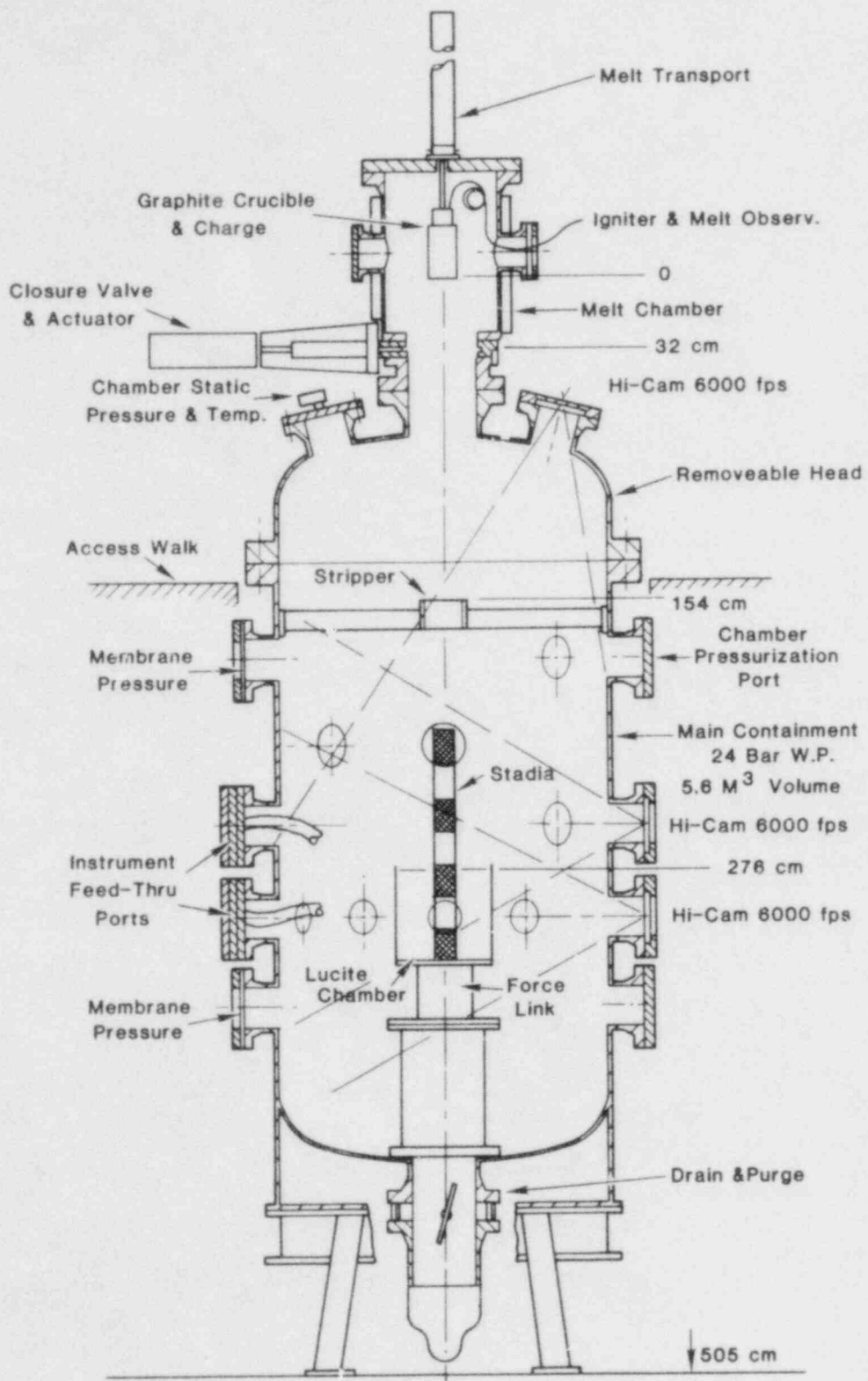
Figure 2-9. Typical FITSA Series Experiment
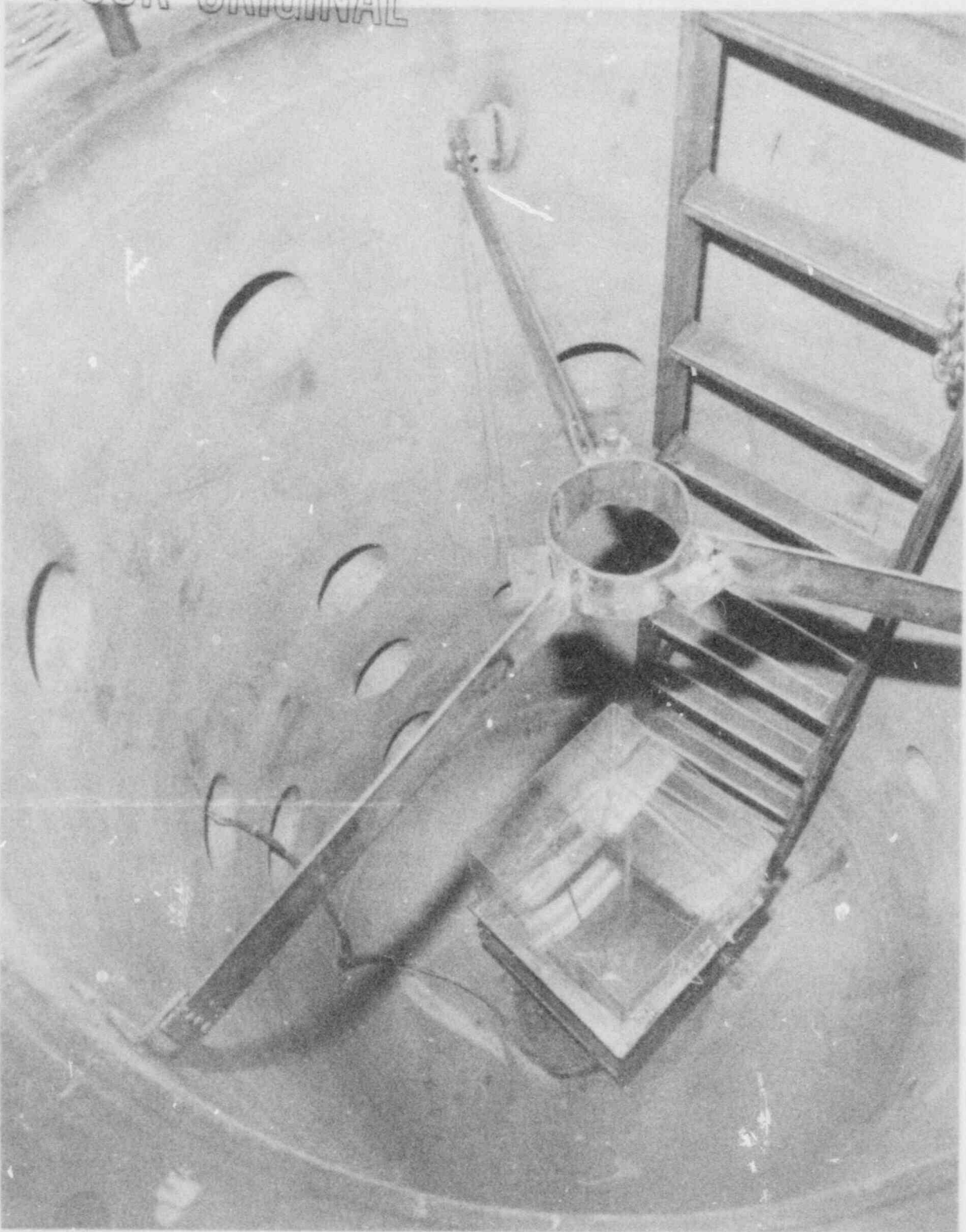
Figure 2-10. Chamber Internals Showing Stripper, Water
Chamber and Instrumentation Cables
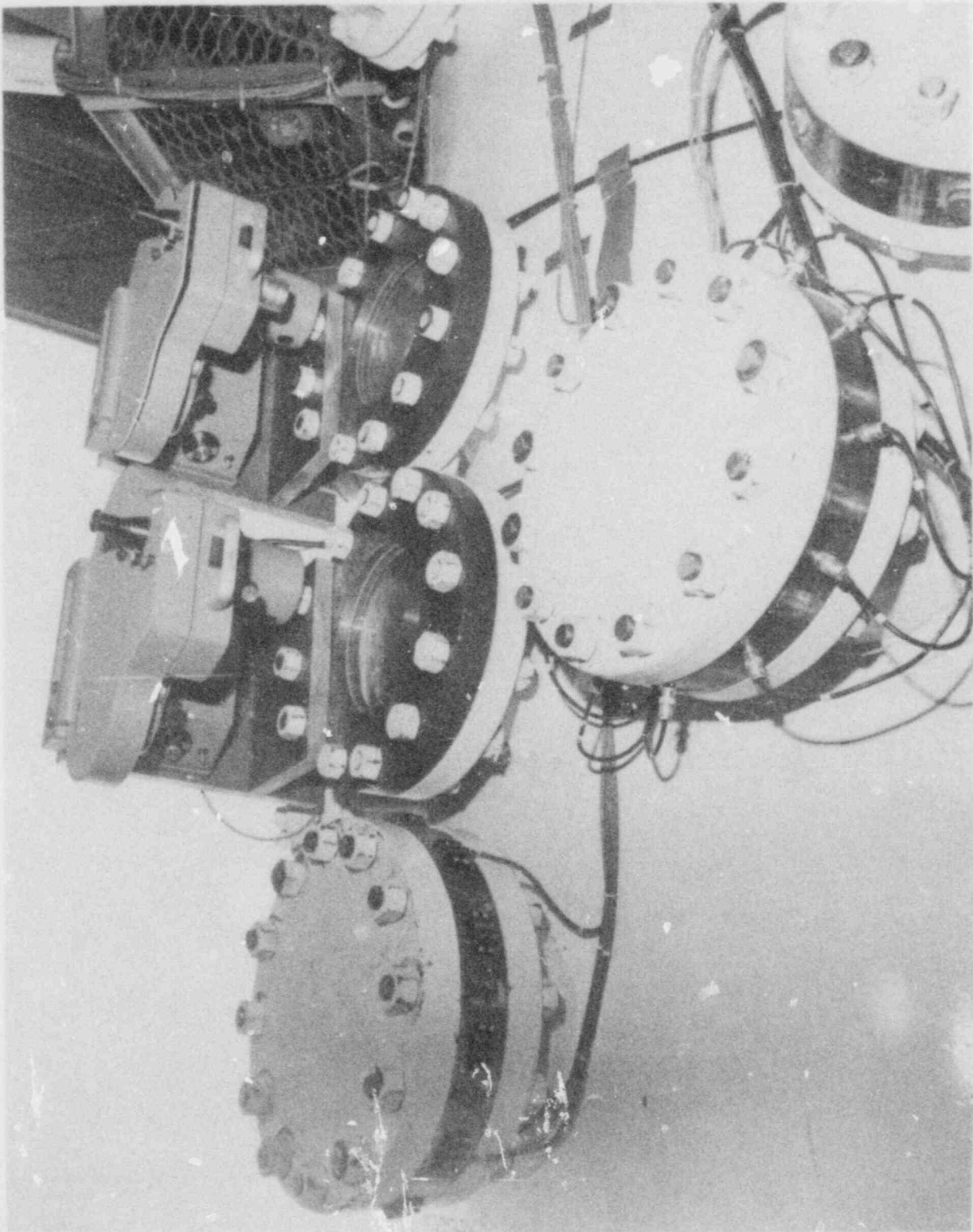
Figure 2-11. Chamber Externals Showing Instrumentation Feed-Through Ports, High Speed Cameras and Camera View Ports
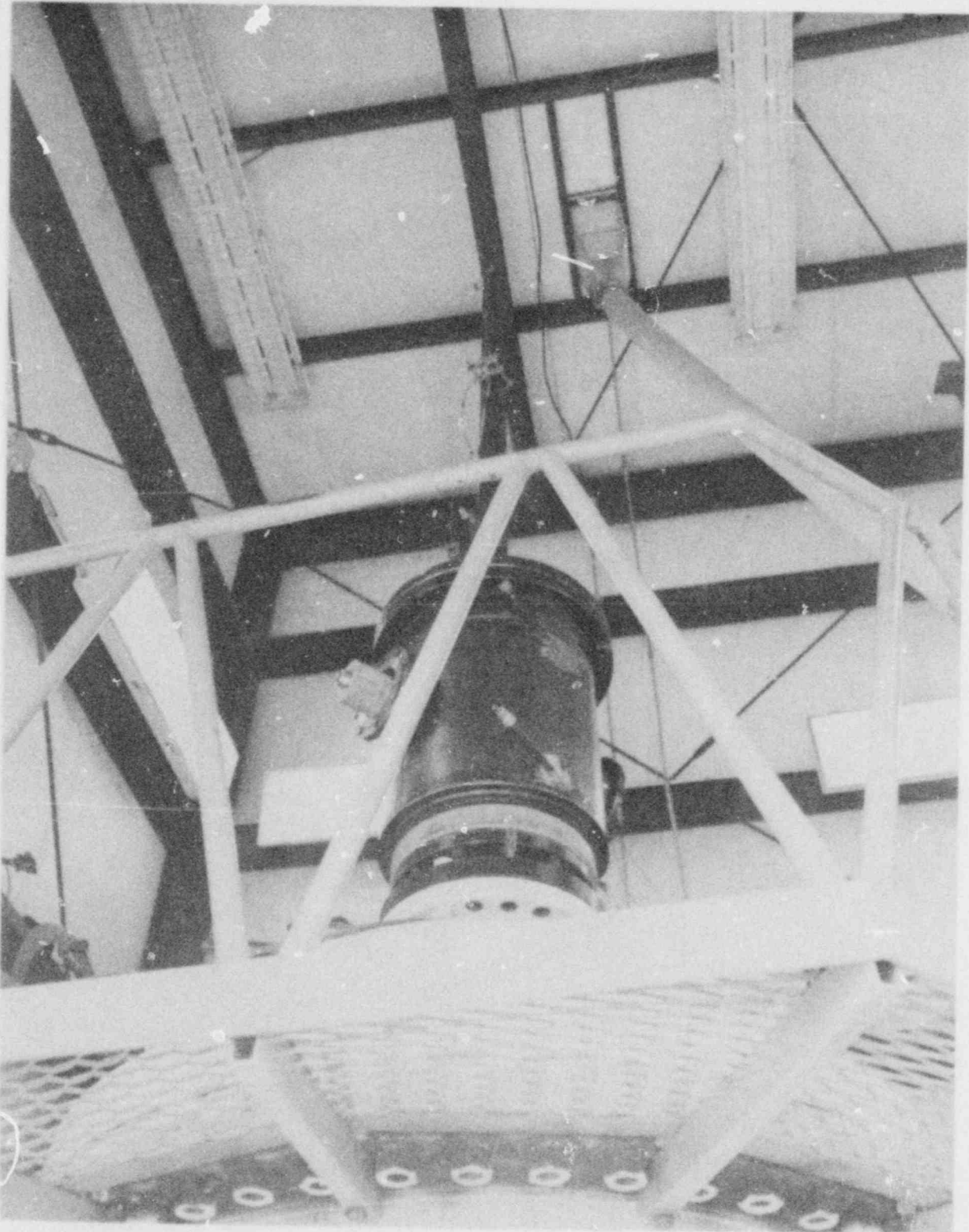
Figure 2-12. Chamber External Showing Melt Section
and Crucible Transport Cylinder

Table 2-1

FITS1A Parameters

Melt: 2.1 kg Fe_3O_4/Al thermite

Coolant: 90.2 kg water at 10°C

Chamber: 3.18 mm thick lucite

Pressure: 0.83 bar

Temperature: 13°C

Melt entry velocity: 6.24 M/S

Instrumentation used during the test is given in Table 2-2.

Table 2-2

FITS1A Instrumentation

Channel	Measurement	Cal. Level	Comment
MS1	Melt	--	Power Supply Mal-function
MS2	" "	--	" " "
P1	Water Pressure	200 bar	
P2	" "	" "	
P3	Base Pressure	500 bar	
P4	Tank Overpressure	1.4 bar	
P5	" "	" "	
P6	Chamber Static	1.4 bar	Digital output
T1	Water Temp	100 °C	
T2	" "	100	Damaged prior to test
T3	Chamber Ambient	100	" "
T4	" "	100	" "
T5	" "	100	
F1	Impulse	66.7 KN	
S1	Chamber Response	500 G	
S2	" "	500 G	
I1	Melt Release	--	

The experiment was successful inasmuch as all systems functioned as intended. A small explosion occurred 0.124 s after the melt entered the water. This reaction, while violent enough to rupture the water container and scatter melt, was not as efficient as the earlier 2-kg experiments, MD15 and MD16. Therefore, the response of the chamber to an energetic steam explosion load was not determined. Signal levels on tank instrumentation were very low because of the small explosion; however, electrical noise, which was a problem on the earlier MD series experiments, was not a problem here. The static pressure transducer recorded a chamber pressurization of 0.083 bar after the experiment and an air temperature rise of 18°C. Debris collected was weighed and more than 90% was recovered, mostly spherical in nature. This debris will be characterized in a manner similar to the work done by Buxton and Nelson.

FITS1A will have to be repeated with minor changes in delivery velocity. The data from this experiment are shown plotted along with the MD data in Figures 2-7 and 2-8 the data show that this quantity of melt, under the delivery conditions which result. .as marginal in terms of spontaneous explosion. The next FITS experiment will use a larger mass.

2.4 Phenomenological Modelling (M. L. Corradini, D. S. Drumheller)

2.4.1 Core Disruption and Meltdown

A major area of uncertainty in the core meltdown scenario for the LWR is how the geometry of the core is initially disrupted and how the meltdown progresses. It is known that a number of physical processes that may threaten containment integrity can result from such an event; e.g., steam explosions, core concrete interactions, hydrogen combustion. However, many of the details of core behavior in a disrupted state or core material motion are unknown. A review of past work in this area by Rivard[1] identified a number of uncertainties in the initial disruption and meltdown process. These uncertainties are of two types, phenomenological and modelling. If the basic physics and chemistry of the process are unknown, the uncertainties are deemed phenomenological. If the physical processes are known to some degree but the overall behavior cannot be predicted at this time due to mathematical complexities, the uncertainties are deemed modelling.

There appear to be four key issues which should be addressed:

1. Thermal hydraulics in a partially disrupted core. Modelling and analysis should be performed

to assess heat transfer from the uncovered, parti-
ally disrupted core to steam, the hydrogen and
liquid water, and the core structural heating
which would result. This question is a modelling
concern that may allow more credit to be taken
for cooling in a partially disrupted state.

2. Material motion during melting. Significant
   phenomenological issues exist in addressing fuel
   and clad motion and the accompanying chemical
   reactions as the core coolable geometry is lost.
   At present it is not clear if a large, molten-
   core pool will form or if the melt will continuously
   flow or drip into the lower plenum. This behavior
   has a significant impact on steam explosions.

3. Heat transfer to surrounding structure from a
   molten core. Heat transfer to surrounding struc-
   ture during core melt is a modeling issue that
   should be addressed. Structure can be weakened
   or melted due to the heat from molten core mate-
   rials. This can affect steam explosions in that
   the solid structure, if it remains, can mitigate
   the effects of the explosions.

4. Core barrel and vessel failure. The consequences of core barrel failure are not well understood, but it is possible that it could lead to an earlier breach of the reactor vessel, or it could restrict or enhance fuel-coolant contact and mixing for steam explosions. These possibilities should be investigated.

Let us briefly consider the issue of material motion during melting. One question is whether the molten core will flow through the solid structure below it, and drip into the lower plenum, or whether it will freeze causing blockages, and thereby enhance the possibility of a larger molten-core pool. A similar question has been under investigation in the LMFBR safety field, and a thin film model has recently been proposed by Eisenhawer et al.[2] to predict the penetration distance of molten fuel through solid core structure. This model is based upon simulant experiments at Sandia[2] and analysis of prototypic experiments by Spencer et al.[3] at Argonne. The model considers the situation where molten fuel is flowing through the core structure melting the solid clad as it is cooled and finally frozen (Figure 2-13). For our case the parameter of interest is the penetration distance before the molten fuel freezes and again forms a plugged-up molten pool. Using this thin film
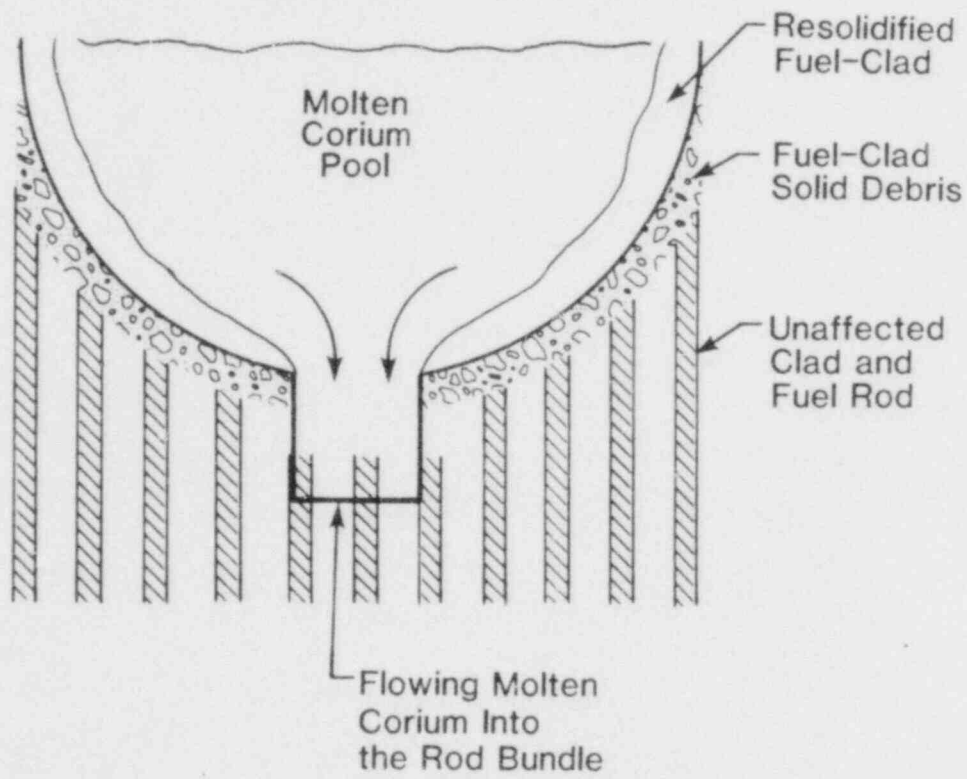
Figure 2-13. Model of Molten Fuel Flowing Through Core Structure and Melting Solid Clad

model, we predict that the molten core material cannot penetrate more than 0 to 0.2 meter before it refreezes and plugs the flow channel. This range of values corresponds to a wide range of initial molten core flow velocities ($\sim$0-6 m/s). This axial penetration distance is much smaller than the active fuel length ($\sim$4 m), suggesting that the formation of a large molten-core pool is possible.

2.4.2 Steam Explosion Thermodynamic Work Potential

An upper bound to the work potential from a steam explosion can be found from a thermodynamic analysis. The work estimate depends on four factors:

1. the amount of fuel and coolant that become involved in the interaction

2. the final state of the interaction; e.g., expansion to 0.1 MPa or to the reactor vessel volume

3. the assumptions used to describe the interaction process

4. the equation of state and constitutive relations used for the fuel and coolant.

We have completed, at this time, a very simplified analysis to estimate the maximum work potential. It should be emphasized that these calculations can only be taken as rough indications of the upper bound. More sophisticated

analysis, utilizing better equation of state models, rate processes for fuel-coolant mixing, fuel fragmentation, and fuel-coolant heat transfer should be used for a realistic assessment of the explosion work potential.

To estimate the work potential, consider that the interaction occurs in two steps. In the first, find the temperature which the fuel and coolant masses achieve if they come into thermal equilibrium with each other under the condition of no expansion of either the coolant or the fuel liquid. This constant volume assumption is only valid if the real equilibration time is short (<<0.1 ms). Based upon real rate processes, it is expected that this assumption would be difficult to achieve. In the second step, find the work done when the coolant and fuel expand reversibly to a prescribed final state either

(a) without heat transfer between the coolant and the surroundings (i.e., adiabatic expansion), or

(b) with the fuel and coolant in thermal equilibrium.

With these somewhat artificial prescriptions for the interaction, we have implicitly prescribed time periods by defining the intermediate state (i.e., that corresponding to the equilibrium temperature at the initial volume) and the final state. In this manner the transient fuel-coolant interaction process has been idealized as a non-flow process. In fact,

these time periods are not real because the processes occurring during the two steps are not physically distinct. Further, there are heat transfer and pdV work rates which characterize this process. However, for convenience, our idealization of a non-flow process between end states allows us to establish conservative bounds on the work potential.

2.4.2.1 Fuel/Coolant Thermal Interaction, Step I - Determination of the Equilibrium Temperature (T_e). The control mass can be identified as either the combined masses of the fuel and coolant or the masses of the coolant and fuel separately. We will choose the latter, hence, two control masses. This is done since it is easier to define the T-S diagrams for one component (two-phase) fluids; i.e., the coolant or fuel alone, to represent the process, than it is to define the T-S diagram for the two component coolant-fuel mixture.

We assume that the liquids can be modelled as incompressible. Therefore, the control masses do not work on the environment during the equilibration process. To conservatively analyze the interaction, we assume that all the heat transferred from the fuel during the process is transferred to the coolant. Finally, because the equilibration process is so fast and the decay heat generation rate is so low, we can neglect the decay heat generated by the fuel

during the process. With these assumptions, the control
mass and the process representation for the coolant alone
can be sketched as in Figure 2-14.
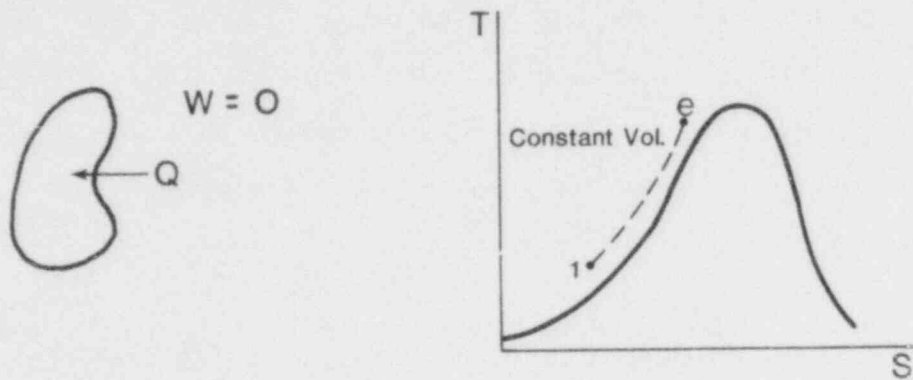
The Control Mass (Coolant)   Process Representation.

Figure 2-14

To evaluate Q, we identify the fuel as another control
mass undergoing a constant volume cooling process to the
equilibrium temperature (Figures 2-15). The comparable
sketches for this fuel mass are
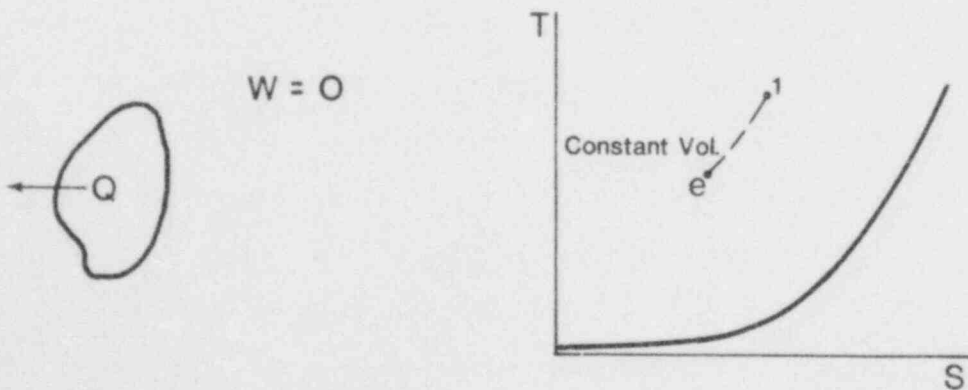
The Control Mass (Fuel)   Process Representation

Figure 2-15

Expressing the first law for each control mass neglecting potential and kinetic energy changes yields

$$\text{Coolant } \Delta E = U = M_c c_{v_c} (T_e - T_{1_c}) = Q \qquad (2-1)$$

$$\text{Fuel } \Delta E = U = m_f c_{v_f} (T_e - T_{1_f}) = Q \qquad (2-2)$$

Equating these results obtain

$$m_c c_{v_c} (T_e - T_{1_c}) = m_f c_{v_f} (T_{1_f} - T_e)$$

or

$$T_e = \frac{\left(\dfrac{m_f c_{v_f}}{m_c c_{v_c}}\right) T_{1_f} + T_{1_c}}{\left(1 + \dfrac{m_f c_{v_f}}{m_c c_{v_c}}\right)} , \qquad (2-3)$$

where m_f = fuel mass c_{v_f} = fuel specific heat

m_c = coolant mass c_{v_c} = coolant liquid specific heat

Note that we have implicitly assumed that the liquid fuel and coolant behave as incompressible liquids with constant specific heats. This again is a very approximate model, which adds simplicity, while sacrificing accuracy. Since this equilibrium state for each component is to the left of the saturated liquid line on a T-S plot, the quality of the fluids of each component by definition are either 1.0 or 0 depending on whether this temperature is above or below the

critical temperature. The quality, X, is unsubscripted with
regard to coolant versus fuel because the fuel remains a sub-
cooled liquid in the examples of the fuel-coolant interaction
in this chapter.

For a water and UO_2 combination, assuming

$$T_{1_f} = 3100K, \quad T_{1_c} = 400 \quad ,$$

$$T_e = \frac{\left(\frac{40,000 \quad (560)}{4,000 \quad (4184)}\right) 3100 + 400}{1 + \frac{40,000 \quad (560)}{4,000 \quad (4184)}} = 1945^\circ K \quad ,$$

and $X_e = 1.0$ since T_e is above the critical temperature of
water, $647^\circ K$.

2.4.2.2 Fuel/Coolant Thermal Interaction, Step II - Coolant and Fuel Expand Independently and Isentropically.

Consider the fuel and the coolant each expanding isentropi-
cally. Let us first estimate the work output of the coolant
in expanding to one atmosphere.

The coolant control mass now does work on the environment,
but transfers no heat. The control mass and the process
representation for the coolant are shown in Figure 2-16.
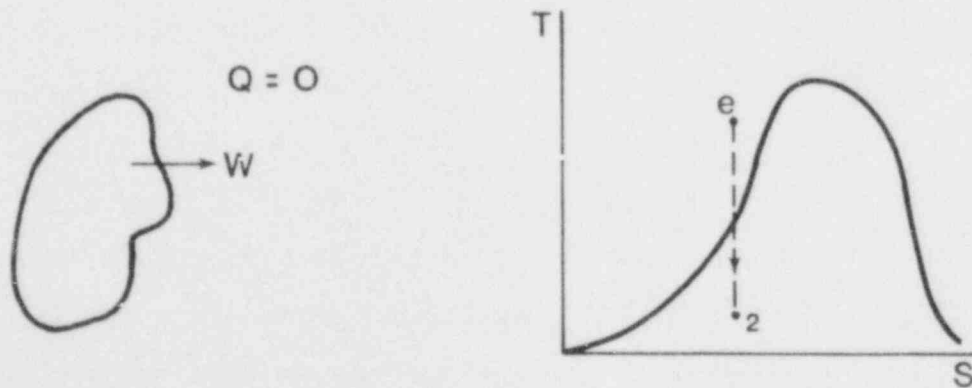
The Control Mass (Coolant)   Process Representation

Figure 2-16

Note that in general in expanding to the final state, 2, some coolant remains in liquid form. Assume that this liquid occupies negligible volume and is incompressible; recognize that this is a gross simplification.

From the first law for our control mass, neglecting potential and kinetic energy changes, we obtain

$$W = -\Delta U \quad , \tag{2-4}$$

or considering internal energy, u, on a unit mass basis

$$W = m_c \Delta u = -m_c (u_2 - u_e) \quad . \tag{2-5}$$

Allowing for expansion into the two phase region, the internal energy is defined as

$$u \equiv c_v T + X u_{fg} \equiv c_v T + X(h_{fg} - pv_{fg}) \quad , \tag{2-6}$$

where h_{fg} is the latent heat of vaporization, assumed constant; p is the pressure; and v is the specific volume.

Using this definition for u, Equation 2-5 can be written as

$$W = m_c \left[c_v(T_e - T_2) + X_e(h_{fg} - pv_{fg})_e - X_2(h_{fg} - pv_{fg})_2 \right] \tag{2-7.1}$$

If we neglect the liquid volume at state 2, this equation can be written as

$$\tag{2-7.2}$$

$$W = m_c \left[c_v(T_e - T_2) + ((Xh_{fg})_e - (Xh_{fg})_2) - ((Xpv_{ge}) - (Xpv_g)_2) \right]$$

To evaluate W, we must first determine X_2 which is done as follows. From the state principle and our selection of an isentropic expansion

$$Tds = dh - vdp = 0 \quad ,$$

which we can rewrite as

$$\frac{dh}{T} = \frac{vdp}{T} \quad . \tag{2-8}$$

From the definition of enthalpy, taking h_{fg} and c_p constant

$$dh = h_{fg}dX + c_p dT \quad . \tag{2-9}$$

Neglecting the liquid specific volume and assuming the perfect gas model applies to the vapor we obtain

$$v \equiv v_f + Xv_{fg} \approx Xv_g = X \frac{RT}{p} \quad . \tag{2-10}$$

Now for our isentropic expansion process, we can express p (T,s) as

$$dp = \left(\frac{\partial p}{\partial T}\right)_s dT$$

If we assume state e is almost at the saturation line so that the expansion is almost totally under the saturation dome, we can express $\left(\dfrac{\partial p}{\partial T}\right)_s$ utilizing the Clausius-Clapeyron

94

equation which relates conditions along the saturation line
to the enthalpy and volume of vaporization. Hence,

$$dp = \left(\frac{\partial p}{\partial T}\right)_S \ dT \cong \left(\frac{\partial p}{\partial T}\right)_{SAT} \ dT = \frac{h_{fg}}{Tv_{fg}} \ dT \cong \frac{ph_{fg}}{RT^2} \ dT \ , \quad (2-11)$$

where the last step utilizes the assumptions of Eq. (2-10).

Substituting the above three relations into Eq. (2-8) and
rearranging we obtain

$$h_{fg} \ \frac{dx}{T} + c_p \ \frac{dT}{T} - h_{fg} \ X \ \frac{dT}{T^2} = 0 \quad ,$$

which can be written as

$$d\left(\frac{X}{T}\right) = - \ \frac{c_p}{h_{fg}} \ \frac{dT}{T} \quad .$$

Now integrating this result between the equilibrium and the
final state we obtain the desired result, i.e.,

$$X_2 = T_2 \left[\frac{X_e}{T_e} + \frac{c_p}{h_{fg}} \ \ln \ \frac{T_e}{T_2} \right] \quad . \quad\quad (2-12)$$

If the equilibrium state is superheated coolant, $X > 1$,
then because we have assumed the coolant vapor behaves
as a perfect gas the work potential becomes

$$W = m_c \ \frac{R_c}{\gamma - 1} \ (T_e - T_2) \ ,$$

where

$$T_2 = T_e \left(\frac{P_2}{P_e} \right)^{\frac{\gamma-1}{\gamma}} \quad ,$$

where γ is the ratio of specific heats and R is the gas constant.

An alternative approach is to use the steam tables if the equilibrium state, $u(T_e, s_e)$, can be located in the tables. The equilibrium entropy, s_e, for an incompressible liquid is given by

$$s_e = s_1 + c_v \ln \frac{T_e}{T_1} \quad .$$

Then the final internal energy at 1 atm can be found at constant coolant entropy by using the tables. This eliminates the approximation in the second step although the simplifications in the first step remain.

2.4.2.3 Fuel/Coolant Thermal Interaction, Step II - Coolant and Fuel Expand Isentropically in Thermal Equilibrium. In this expansion process the coolant-fuel mixture expands isentropically but because the coolant and fuel are prescribed to remain in thermal equilibrium, the coolant entropy increases while the fuel entropy decreases. This

process representation is felt to be conservative and non-mechanistic. We are forced to use gross simplifications in the equation of state models to obtain an analytical answer. The model was originally used by Hicks and Menzies[4] for the UO_2-sodium system.

The coolant passes into the two-phase region and may achieve a superheated vapor state. The actual state achieved must be calculated. On the other hand, the fuel remains a subcooled liquid (or solid if it freezes) throughout the expansion process because of the relative slopes on a T-S diagram of the typical expansion path and the fuel saturated liquid line. Figure 2-17 shows the control mass and process representations for the coolant and for the fuel as separate control masses; for illustration, the final coolant state is shown as superheated vapor.
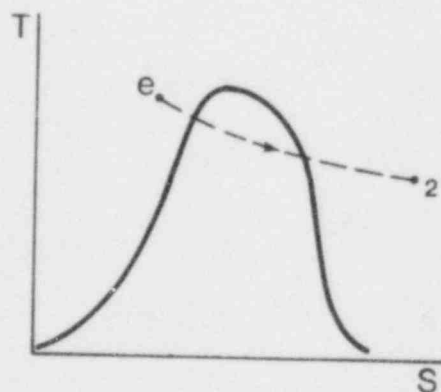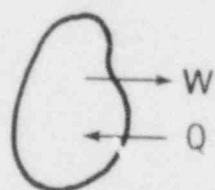
The Control Mass (Coolant)   The Process Representation
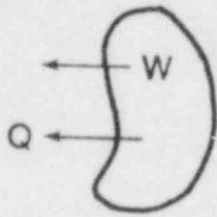
Figure 2-17
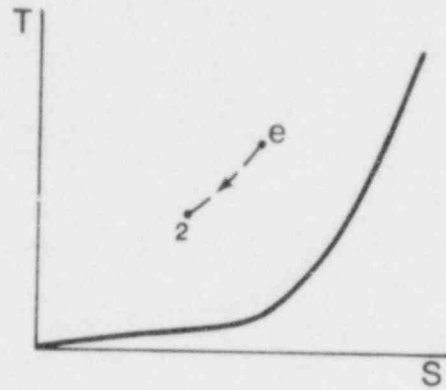
The Control Mass (Fuel)   The Process Representation

Figure 2-17 (cont'd)

The net work could be calculated by summing the work computed
for each phase separately, assuming each expanded to its
partial pressure consistent with the final total pressure
of one atmosphere. In this case, however, it is simpler to
consider the mixture as the control mass. The corresponding
graphical representation for the mixture are
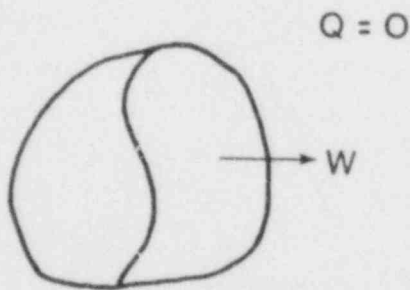
The Control Mass (Mixture)   The Process Representation
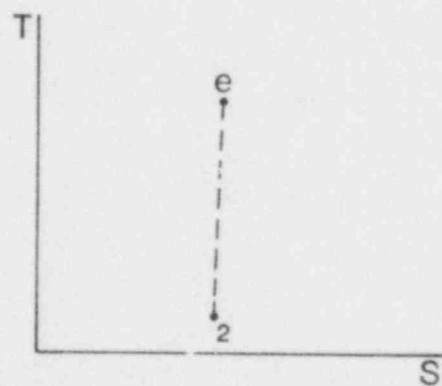
Figure 2-18

In the analysis we assume that the liquid phase of each component occupies negligible volume and is incompressible. Eq. (2-4) is the relevant first-law formulation but now is applied to the mixture. Considering the internal energy on a unit mixture mass basis, Equation 2-4 is written as

$$W = -m_m \Delta u_m = -(m_c \Delta u_c + m_f \Delta u_f) \quad . \qquad (2-13)$$

To express the coolant internal energy change, Δu_c, the final state of the coolant (i.e., whether it is a two-phase mixture or a superheated vapor) must be known. Therefore, we must evaluate the final coolant quality, X_2, to see if it is less than or greater than unity. To do so, we repeat the procedure of Example 2, but now consider the mixture expansion as isentropic.

From the state principle for the mixture in this isentropic process,

$$T_m ds_m = dh_m - v_m \, dp_m = 0 \quad . \qquad (2-14)$$

From the definition of mixture enthalpy,

$$h_m = \frac{\left(m_c c_{p_c} + m_f c_{p_f} \right) T + m_c \, X \, h_{fg_c}}{m_c + m_f} \quad . \qquad (2-15)$$

Differentiating,

$$dh_m = \frac{\left(m_c c_{p_c} + m_f c_{p_f} \right) dT + m_c h_{fg_c} dX}{m_c + m_f} \quad . \qquad (2-16)$$

Again, using the simplification for the fuel volume and the liquid coolant volume, Eq. (2-10), we obtain

$$v_m = \frac{X m_c v_{g_c}}{m_c + m_f} = \frac{XRT}{P} \left(\frac{m_c}{m_c + m_f} \right) \qquad (2-17)$$

Utilizing the Clausius-Clapeyron equation in the same manner as previously

$$dp_m \cong \left(\frac{dp}{dT} \right)_{\substack{SAT \\ coolant}} dT = \frac{p h_{fg_c}}{R_c} \frac{dT}{T^2} \qquad (2-18)$$

Substituting the above three relations into the state principle and rearranging, we obtain

$$\left(m_c c_{p_c} + m_f c_{p_f} \right) \frac{dT}{T} + m_c h_{fg_c} d\left(\frac{X}{T} \right) = 0 . \qquad (2-19)$$

Now integrating this result between the equilibrium and final states yields

$$X_2 = T_2 \left[\frac{X_e}{T_e} + \left(\frac{m_c c_{p_c} + m_f c_{p_f}}{m_c h_{fg_c}} \right) \ln \frac{T_e}{T_2} \right] , \qquad (2-20)$$

where T_2 is taken as the saturation temperature for one atmosphere. This result indicates that the final coolant state is a superheated vapor so that Δu_c is written as

$$\Delta u_c = \Delta u_c (X_e = 0 \text{ to } X = 1) + \Delta u_c \ (X = 1 \text{ to the actual state 2})$$

which can be written as follows, using Eq. 2-6 and the numerical values of X_e and X,

$$\Delta u_c = \left[c_v (T - T_e) + h_{fg} - p v_{fg} \right]_c + c_{v_{vc}} (T_2 - T), \qquad (2-21)$$

where T is the temperature corresponding to X equal to unity, and the subscript on c_v in the second term explicitly indicates that the coolant is in vapor form.

The fuel internal energy is

$$\Delta u_f = c_{v_f} (T - T_e) + c_{v_f} (T_2 - T) \quad . \qquad (2\text{-}22)$$

To evaluate Δu_c and Δu_f the final temperature, T_2, must be determined in the superheat region. This is done again using the state principle, Eq. (2-14), but now considering only that portion of the expansion process in which the coolant state is a superheated vapor. Therefore, Eq. (2-16) is written as

$$dh_m = \frac{\left(m_c c_{p_{vc}} + m_f c_{p_f} \right)}{m_c + m_f} \ dT \ , \qquad (2\text{-}23)$$

where again $c_{p_{vc}}$ is the specific heat of the coolant vapor and explicitly indicates that the coolant is in vapor form and Eq. (2-17) is written as

$$v_m = \frac{RT}{p} \left(\frac{m_c}{m_c + m_f} \right) \quad . \qquad (2\text{-}24)$$

Substituting Eq. (2-23) and (2-24) into Eq. (2-14), we obtain the following relation between mixture temperature and pressure:

$$\left[\frac{m_c c_{p_{vc}} + m_f c_{p_f}}{m_c R_c} \right] \frac{dT}{T} = \frac{dp}{p} \quad . \qquad (2\text{-}25)$$

Defining the above term in brackets as n, integration of Eq. (2-25) to the known final state p_2, T_2 yields

$$T_2 = T \left(\frac{T_2}{p} \right)^{1/n} \quad . \qquad (2\text{-}26)$$

This form of the state principle [i.e., Eq. (2-26) with Eq. (2-13) can be used to evaluate the work potential if the equilibrium state, $u(T_e, s_c)$, is initially super-heated. Unfortunately, we cannot use the steam tables to verify the accuracy of this process because this is not an isentropic coolant expansion. It is felt that this model is very crude and gives a very large upper bound estimate.

We used the isentropic coolant expansion model to predict the maximum explosion work potential; this calculation was for a given amount of fuel and coolant expanded to the reactor vessel free volume. Our realistic estimate for the steam explosion work potential, 300 MJ, is based upon a mechanistic analysis of Buxton's experiments[6] and extrapolating up to the reactor scale, assuming the same configuration with 10% of the core interacting with 10 metric tons of water. The thermodynamic limit for this fuel-coolant mixture is 500 MJ. An upper bound work potential estimate of 3000 MJ results from assuming 40% of the core interacts with 20 metric tons of water in the lower plenum, and an isentropic coolant expansion.

We emphasize that these estimates are very approximate because the analysis used is based on a number of gross simplifications.

2.4.3 Transient Propagation Model

Once the trigger induces film collapse the rapid
heat transfer process begins. This induces a local pres-
sure increase, and a collapse of nearby vapor films. The
resulting effect propagates through the mixture. There is
extensive research work involved in this phase of the
explosion. At present relatively little is known about
either how the explosion propagates or how the mechanisms for
fuel fragmentation and fuel-coolant heat transfer. Experi-
ment and analysis are now being performed to gain knowledge
on how the explosion propagates so that the initial condi-
tions for the coolant vapor expansion and the explosion
work potential may be ascertained.

Recent experiments by Mitchell[5] using $Fe-Al_2O_3$ and
water have indicated that the rapid fuel fragmentation and
heat transfer observed in Nelson's experiments can occur at
a much larger scale (fuel mass = 5 kg). Mitchell observed
a rapidly propagating explosion through a coarsely mixed
fuel-coolant system. Large peak pressures were generated
(> 15 MPa) and a shock front propagating at 300-500 m/s was
observed. Behind this front fuel appeared to be rapidly
fragmented.

To model the propagation phase of the fuel-coolant
interaction in large-scale systems, we have developed a
transient one-dimensional computer model, based upon a two-phase

mixture theory. The model represents the mixture as an array of molten fuel drops, each surrounded by a vapor film immersed in the liquid coolant. This microscopic structure can account for a number of the physical effects that we believe are important to the propagation phase.

To simplify the theoretical formulation and the subsequent numerical analysis, we have made two fundamental assumptions:

1. Relative motion between the fuel drop, vapor film, and surrounding coolant is ignored for film collapse calculations.

2. The mixture is represented as a homogeneous system; i.e., at any point in the mixture, the initial fuel radius and vapor film thickness are the same but will subsequently vary with time and space.

The first assumption implies spherically symmetric film collapse. The second assumption can be relaxed. However, a homogeneous system is considered a good first approximation.

This problem employs Lagrangian coordinates because our interest is in short-time wave propagation phenomena with associated small displacements or flows. As an example of the governing equations let us look at the mass continuity equation for the mixture

$$\rho_m V = (\rho_m V)_0 \quad , \tag{2-27}$$

where ρ_m is the mixture density and V is the mixture material volume. This is equivalent to the Eulerian formulation. The material density, ρ_m, and the volume fractions, ϕ_i, follow the constraint relations

$$\rho_m = \phi_H \rho_H + \phi_c \rho_c + \phi_v \rho_v \qquad (2-28)$$

$$\phi_v + \phi_H + \phi_c = 1 \qquad (2-29)$$

where H, v, c refer to fuel, coolant vapor, and coolant liquid. A complete derivation of the remaining conservation laws and constitutive relations have been done in two ways: (1) by the method of Lagrange Multipliers and (2) by a simplified two-phase theory for bubbly flow.

The key ingredient in the model is the mechanism for fuel fragmentation that initiates the explosion and sustains it.

At the present time, we propose two mechanisms that may separately or jointly cause fuel fragmentation and significantly increase the energy exchange rates between fuel and coolant during the final stages of film collapse. The first model considers that the impact of the liquid on the fuel drop during collapse causes cavitation of the fuel melt. The second model considers that fuel collapse and the initial rapid vapor generation and high pressures cause Taylor instabilities that fragment the fuel and enhance the heat transfer.

Provided we are willing to sacrifice some computational efficiency, existing wave propagation codes designed to solve conventional continuum relations can be modified to solve these equations. This is a feasible approach since the mass equation and the momentum equation retain the conventional forms for single-material mechanics problems.

We have chosen to modify the one-dimensional Lagrangian wave propagation code, WONDY IV. The explicit, finite-difference scheme used in WONDY IV is structured so that, as a particular mesh point is advanced in time, the new position is first computed from known values of the pressure and the mixture momentum balance, and then the new density is computed from the balance of mixture mass. To complete the cycle of computations, the equation-of-state subroutine is then called and a new value of pressure and internal energy is computed by simultaneously solving the constitutive equation for pressure and the energy balance equation.

This format is useful for our problem since the mixture mass and momentum equations are already built into the code. The remaining field equations in the mixture formulation are local statements; that is, they do not contain spatial gradients, and can be solved in the equation-of-state subroutine.

The new equation-of-state subroutine is constructed in the following manner: first, the old and new values of

density, ρ, are linearly interpolated to give a continuous value of ρ across the time step; then the energy equations along with the vapor-film collapse relations are viewed as a set of ordinary differential equations in time; finally, these equations are integrated from the old value of time by means of a Runge-Kutta technique. This provides the new value of mixture internal energy, U_M, and the new value of mixture pressure, P_M, which are required to continue the computation.

This computational scheme has proven useful in a variety of similar problems wherein complex differential relations are integrated in the equation-of-state subroutine. In particular, accurate modelling of experimental data for pressure waves propagating in bubbly liquids has been achieved. In general we have found that the Runge-Kutta integration scheme can be replaced by more accurate methods without altering the results. Also, because of the rate-dependent nature of the film collapse relations, the usual artificial viscosity terms found in these wave codes can be eliminated.

Figure 2-19 contains two wave profiles at 0.14 ms and 0.26 ms after initiation of the trigger pulse. The trigger pulse which occurs on the right boundary is a square wave input 10 MPa in amplitude and 10 μs in duration; however, trigger pulses as low as 1 MPa result in an explosion in this example. The mixture is modelled after some of Mitchell's
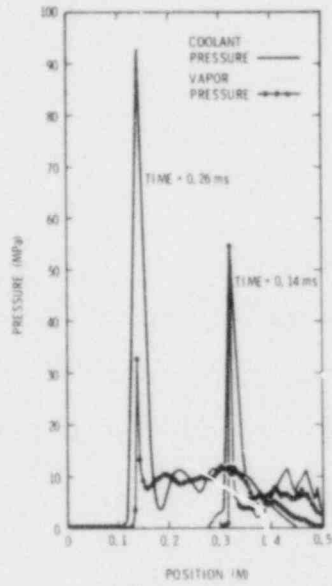
Figure 2-19. Wave Profiles at 0.14 ms and
0.26 ms After Initiation of
Trigger Pulse

experiments[5] and contains 20% by volume of 10 mm diameter
molten fuel drops with 0.2 mm thick films. Both the pressure
within the vapor film and within the surrounding coolant
are plotted. At the head of the left-traveling wave is a
pressure spike which is a result of film collapse and
coolant impact on the fuel drops. In this calculation,
an acoustic cavitation fragmentation converts 10% of the
impact energy a into new fuel-coolant contact surface area
by using a surface tension coefficient of 0.4 N/m. The
resulting vaporization of the coolant after impact is
evidenced by a buildup of pressure over the entire region
behind the pressure spike. This broad region of elevated
pressure in turn initiates the final expansion phase of the
vapor explosion.

2.5 Assessment of Containment Failure (M. L. Corradini,
    D. V. Swenson)

In January 1980, the Nuclear Regulatory Commission
Research Branch requested that Sandia and Los Alamos assist
in a study of the Zion and Indian Point Nuclear Power
Stations. The stated purpose of the ZIP study was to
identify some of the methods for significantly reducing the
likelihood of large airborne radioactivity releases due to
core melt accidents for plants located in large population
densities, i.e., Zion and Indian Point.

109

One physical process that may threaten the containment is a steam explosion. A possible consequence of this interaction would be the generation of solid missiles from the reactor vessel that might threaten the containment integrity.

Design measures which can significantly reduce the risk of such accidents (e.g., filtered vented containment system or additional shielding), as well as realistic estimates of the consequences and risk of such accidents, were investigated. Because the ZIP study had both risk assessment and design objectives, the consequences of steam explosions were estimated in both realistic and conservative frameworks; realistic, because in this way the explosion can be compared to other containment designs, and conservative because it is desirable that the probability of failure by steam explosion should be very small. Therefore, the goals of this brief study were to

1. determine if large mass missiles can be formed by realistic and upper bound steam explosions

2. determine if small mass missiles can threaten the containment.

Calculations have been completed for a range of slug energies; i.e., 300 MJ and 3000 MJ. The first value was taken from analysis in SAND79-2002. The second value and

upper bound, corresponds to 1.5% of the fuel thermal energy in the entire core.

Several structural analyses were performed to examine the effect of the slug type (i.e. liquid fuel, liquid coolant, solid), liquid slug shape, slug velocity, and reactor vessel internal pressure on the impact of the slug with the reactor vessel head. The results of these analyses suggest that the greatest deformation of the head occurs at the top. Based upon either a plastic strain failure criteria or a fracture mechanics failure criteria the top of the head is predicted to fail first. The behavior after this initial failure location is uncertain. It appears that the reactor vessel stud bolts might also fail later in time, neglecting stress relief due to the first failure. Therefore, the preliminary conclusions drawn from these results were that

1. the top of the reactor vessel head will fail first in all the loading configurations considered.

2. based on this behavior it seems unlikely that a large mass missile would be generated.

3. small mass missiles, e.g. a control rod drive assembly (CRD), could be generated at velocities in the range of 100-400 m/s.

Code calculations have also been completed to determine the penetration capability of a small mass missile, CRD, with a velocity in the range of 100 to 400 m/s. The missile

impacts the control rod concrete missile shield which is above the reactor vessel. The missile was modelled as a solid mass of steel, while the reinforced concrete was modelled as concrete interspersed with steel layers. The initial computations utilized a coarse spatial mesh of the missile and concrete to determine the overall response. The results indicated that some penetration of the concrete occurred but the missile was greatly decelerated and subsequently destroyed. Based on these results the preliminary conclusion reached was that it is unlikely for a small mass missile to penetrate both the missile shield and the containment.

The research work is continuing in two areas

1. to identify mitigating effects on missile generation due to the explosion

2. to refine the structural calculations performed to assure that they are conservative.

The uncertainty in these preliminary conclusions necessitates further research, although the expectation is that the conclusions are conservative.

References

1. J. B. Rivard, "Review of In-Vessel Meltdown Sequence," Zion-Indian Point Study, SAND80-0617 (Albuquerque, NM: Sandia Laboratories, March 1980).

2. S. W. Eisenhawer, D. O. Lee, M. L. Corradini, R. W. Ostensen, "A Study of Heat Transfer from a Flowing Liquid to a Melting Wall," Proc. of the Fast Reactor Safety Conference, Seattle, WA (1979).

3. B. Spencer, et al., Transactions of the American Nuclear Society, 29, 446, (1978).

4. D. Hicks, B. Menzies, Argonne National Laboratory Report, ANL-6120, (1965).

5. M. Berman (Ed.) Light Water Reactor Safety Research Quarterly Report, SAND80-0927, October 1979 (Albuquerque, NM, Sandia Laboratories, nd), to be published.

6. L. D. Buxton, W. B. Benedick, "Steam Explosion Efficiency Studies," SAND79-1399, NUREG/CR-0947 (Albuquerque, NM: Sandia Laboratories, December 1979).

3.   Separate Effects Tests for TRAP Code Development

3.1   Summary (R. A. Sallach, R. E. Elrick)

The TRAP code was developed at Battelle-Columbus in order to predict the quantity of fission products transported from the reactor core to other primary system regions as a result of various accident scenarios. The code requires information about the fission product elements, such as the nature of the vapor species and their vapor pressures. In addition information is required about the interaction of the vapor species with the walls. This program supplies that information by conducting separate effects tests to identify the vapor species and to provide quantitative data as needed. The fission products which are of most concern are cesium, iodine, strontium, tellurium, and ruthenium.

The experimental effort is two-fold -- the first part includes transpiration tests in which the transport of a single compound is studied; the second part is directed at using laser Raman spectroscopy to study transport of single and multiple compounds. These are discussed in more detail in the following paragraphs.

3.2   Transpiration Tests

These tests are performed at New Mexico Tech and at Sandia National Laboratories in Albuquerque.

3.2.1 New Mexico Tech

The vaporization and transport of cesium hydroxide is being studied. The analysis of an earlier test series at 580-590°C has been completed. The mass transport of cesium as cesium hydroxide in moist nitrogen at 587 ± 4°C is 5.5 mg Cs/liter of gas. The calculated vapor pressure assuming a CsOH monomer as the gas specie is 0.8 torr (not 0.08 torr as reported in the February monthly report). This value is higher than expected. The vapor pressure data for NaOH and NaI and for KOH and KI[1] indicate that the hydroxide and iodide of the same alkali element should have comparable vapor pressures. Extrapolation of CsI data down to 590°C predicts ~0.08 torr.

A possible explanation is that CsOH + H_2O vapor complexes were formed. Subsequently, CsOH was vaporized into dry nitrogen. The very preliminary results indicated a vapor pressure of 0.2 to 0.3 torr. However additional tests are needed before the interpretation of CsOH + H_2O vapor complexes can be considered confirmed.

3.2.2 Sandia National Laboratories

Minimal experimentation was performed during this quarter due to the relocation of the laboratory. Pure SrI_2 was prepared since earlier experiments had indicated that SrI_2 was stable in high temperature water vapor. Thermodynamic calculations (based on the JANAF tables) suggest

that if CsOH is also present in the gas stream the reaction

$$2CsOH + SrI_2 \longrightarrow 2CsI + Sr(OH)_2$$

should occur; i.e., SrI_2 is not expected to be a significant vapor species in accident scenarios.

The transport of tellurium was considered. Thermodynamic calculations indicate that in a pure steam flow or with hydrogen gas also present the vapor species are Te_2 and/or H_2Te. However, Te_2 has been reported[2] to react with a stainless steel alloy above 450°C. Unanswered are the following questions:

> At what temperature does dissociation of the solid
> metal tellurides become important?
> Would an oxide layer produced by the reaction of
> the stainless steel with high temperature steam
> prevent the reaction with Te_2 vapor?
> What is the effect of steam exposure on a metal
> surface containing absorbed or reacted tellurides?

A series of experiments has been started to address these questions. Samples of both stainless steel and nickel have been reacted with Te_2 vapor producing a metal telluride coating containing 10^{-1} mg Te/mm^2. Characterization of these coatings is in progres   Specimens will then be exposed to various gas steams   .d temperatures to determine where the tellurium goes.

3.3 Laser Raman Spectroscopy

Two experimental arrangements will utilize Raman spectroscopy. The first is an interim apparatus in which single vapor species are produced in a nitrogen gas stream. Its purpose is to obtain base spectra for these vapor species and investigate their interaction, if any, with H_2O vapor and H_2 gas. The second is the Fission Product Reaction Facility. Here multiple fission product vapor species are introduced into high temperature steam giving a better simulation of reactor accident conditions. Their status is as follows.

3.3.1. Interim System - A laser Raman spectrograph system has been made available for these experiments. An optical cell has been designed and almost completed. Some difficulty was encountered in welding the nickel crucible which is the source of the vapor species. Other welding techniques are being tried. No further difficulties are expected.

3.3.2. Fission Product Reaction Facility - Design and fabrication of this facility is on schedule. Design is more than 80 percent complete while fabrication is over 60 percent complete.

References

1. Handbook of Chemistry and Physics, 56th Edition, R. C. Weast, Ed., CRC Press, Cleveland, Ohio, 1975-1976.

2. J. Nucl. Mater. 62 (1976) 50-62.

4. Containment Emergency Sump Performance

4.1 Summary (G. G. Weigand, M. Berman, R. R. Prairie)

The containment emergency sump performance (CESP) program will investigate the reliability of emergency core cooling system (ECCS) sumps. The CESP program provides technical direction to the DOE-sponsored, experimental sump program at Alden Research Laboratory (ARL), and it has a two-fold purpose:

- to provide a containment-sump data base to NRC, and
- to provide ECCS sump design information to the nuclear industry.

ARL is constructing the full-scale test facility. We reviewed the test facility design and instrumentation and forwarded our comments to ARL. ARL projects a test facility completion date of mid-June 1980.

The test program will investigate three design areas of interest:

- generic behavior of sumps,
- behavior of the sump under adverse conditions caused by flow disruptions, and
- vortex suppression concepts.

The test program combines a statistically based technique (fractional-factorial experiment design) and the one-at-a-time variation technique. The fractional-factorial technique is used because it can, with a minimum outlay of resources,

investigate main variable effects and some variable interactions. The test program utilizes $(1/3 \times 3^4)$ and $(1/2 \times 2^5)$ fractional-factorial designs to investigate primary variable effects, and it utilizes the one-at-a-time variation technique to study secondary variable effects.

4.2 ECCS Sump

A loss-of-coolant accident (LOCA) in a pressurized water reactor (PWR) will trigger the reactor's emergency core cooling system (ECCS). The ECCS supplies coolant to the reactor core and vessel to dissipate the decay heat, and under certain conditions it supplies coolant to the containment spray system (CSS) to reduce containment pressure and scrub radioactive material from the containment environment. A failure of the ECCS can be serious; the disruption of core coolant flow could lead to core damage.

The removal of decay heat and the scrubbing of the containment environment can be long-term operations; thus, continuous operation of the ECCS depends upon a continuous supply of coolant. During the initial portion of a LOCA, the ECCS draws coolant from on site storage tanks. If the storage tanks are depleted, the ECCS could switch to a recirculation mode of operation. In the recirculation mode the ECCS draws discharged coolant from the containment building sumps. Containment sump operation can thus become a key link in the flow to the reactor which would protect the containment.

Preoperatonal tests have been performed at a number of plants to demonstrate sump operability in the recirculation mode. Adverse flow conditions--such as air entrainment, cavitation, and vortexing--were encountered in virtually every test. As a result the NRC has placed the operability of the containment sump into the unresolved safety issues category and has given high priority to research that addresses containment sump reliability. This report discusses recent progress in the construction and experimental design phases of the CESP program.

4.3 Facility Design and Construction

The CESP test facility is under construction at ARL. Details of the full-scale, test-facility design are presented in Reference 1. We have reviewed the design of the facility and its instrumentation and have forwarded comments to ARL. Figures 4-1 through 4-4 show the test facility layout. Figures 4-2, 4-3 and 4-4 show the general features of the experimental test facility, while Figure 4-1 shows specific details of the sump. The CESP sump will accommodate most of the wide range of geometric and flow variables that would be expected in actual plant installations. The design emphasizes generality and variability. The sump can operate with single or multiple outlet pipes, with flow rates ranging to as high as 20,000 gpm, and with various internal configurations
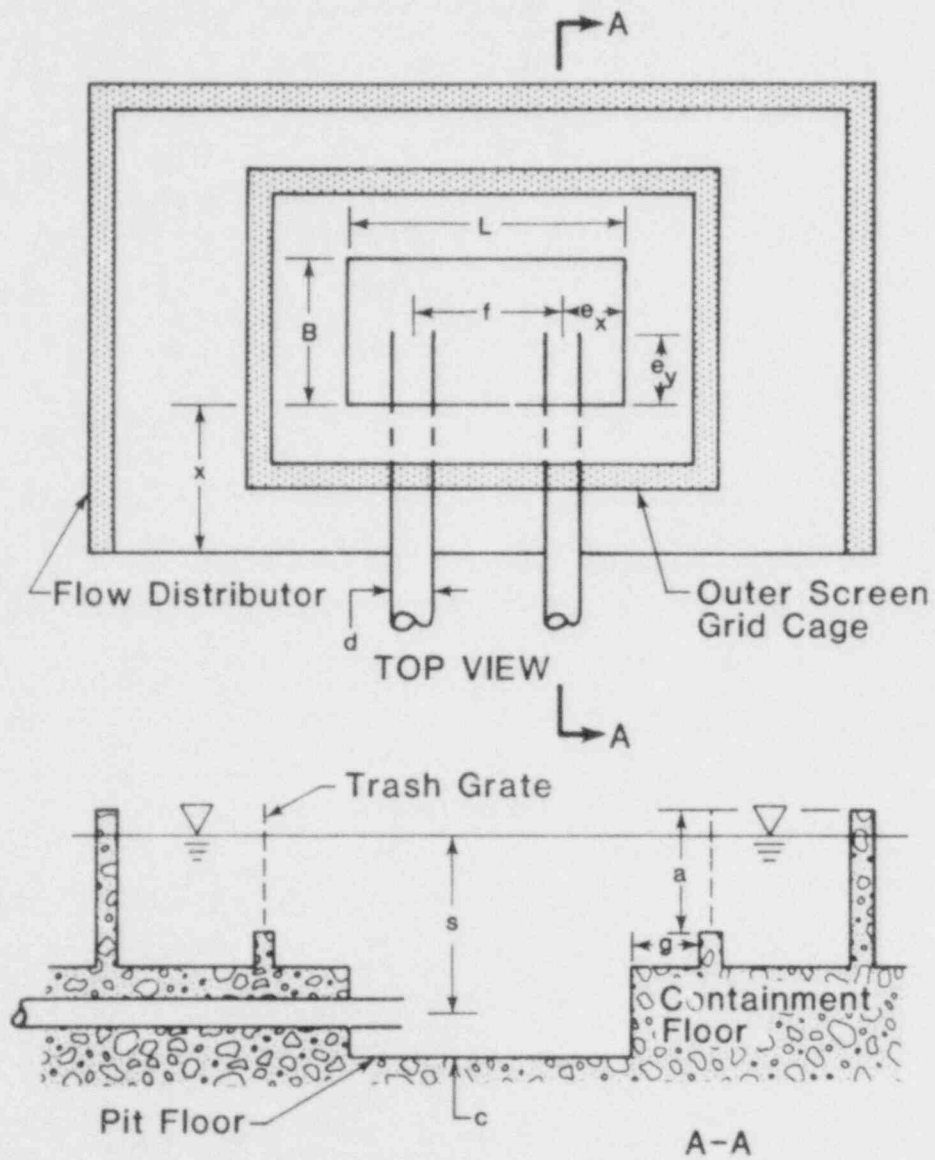
Figure 4-1. Details of the ECCS Sump under
Investigation in the CESP Program
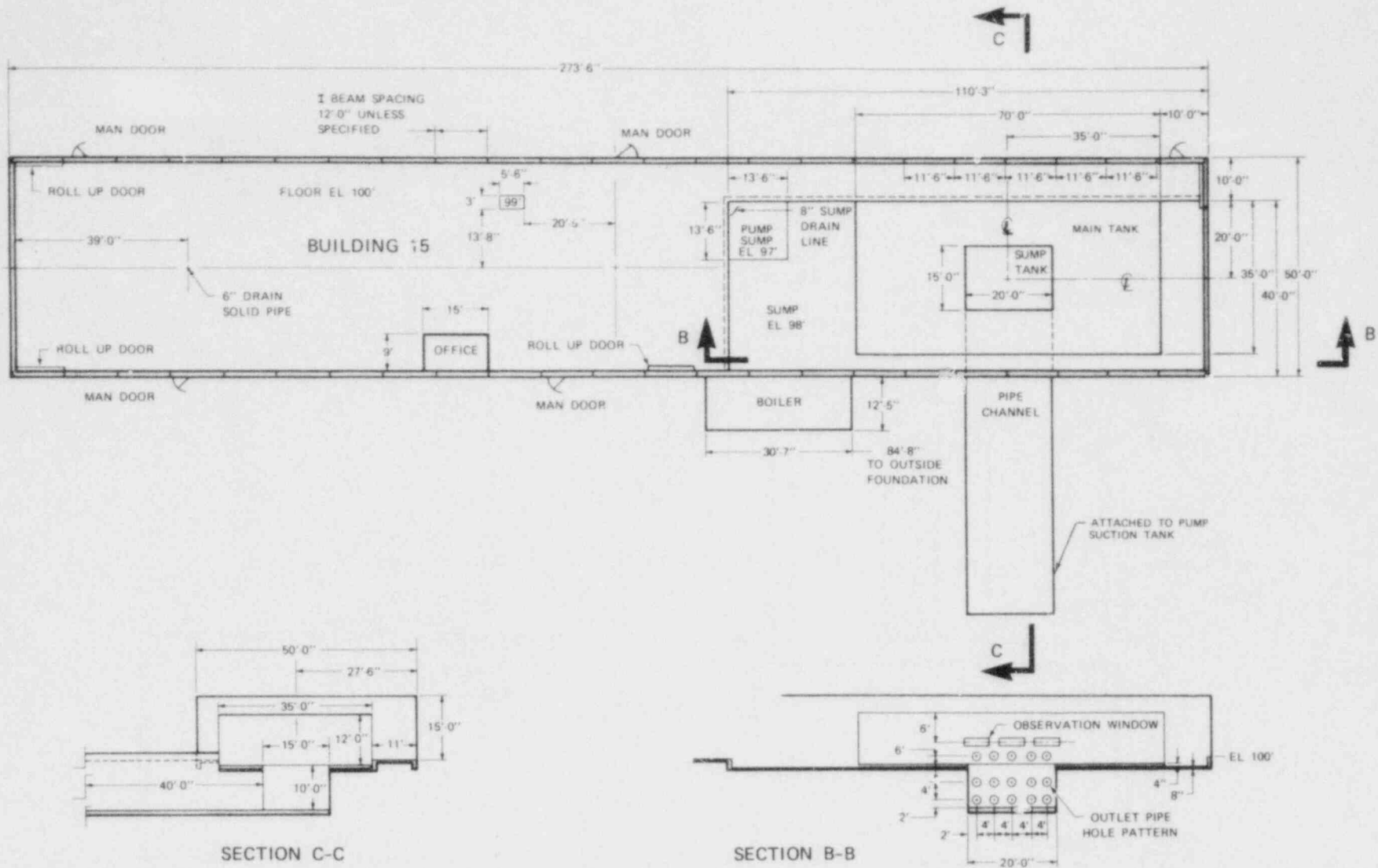
Figure 4-2.   General Layout of the Test Facility Building Showing the Sump and Main Tank Placement
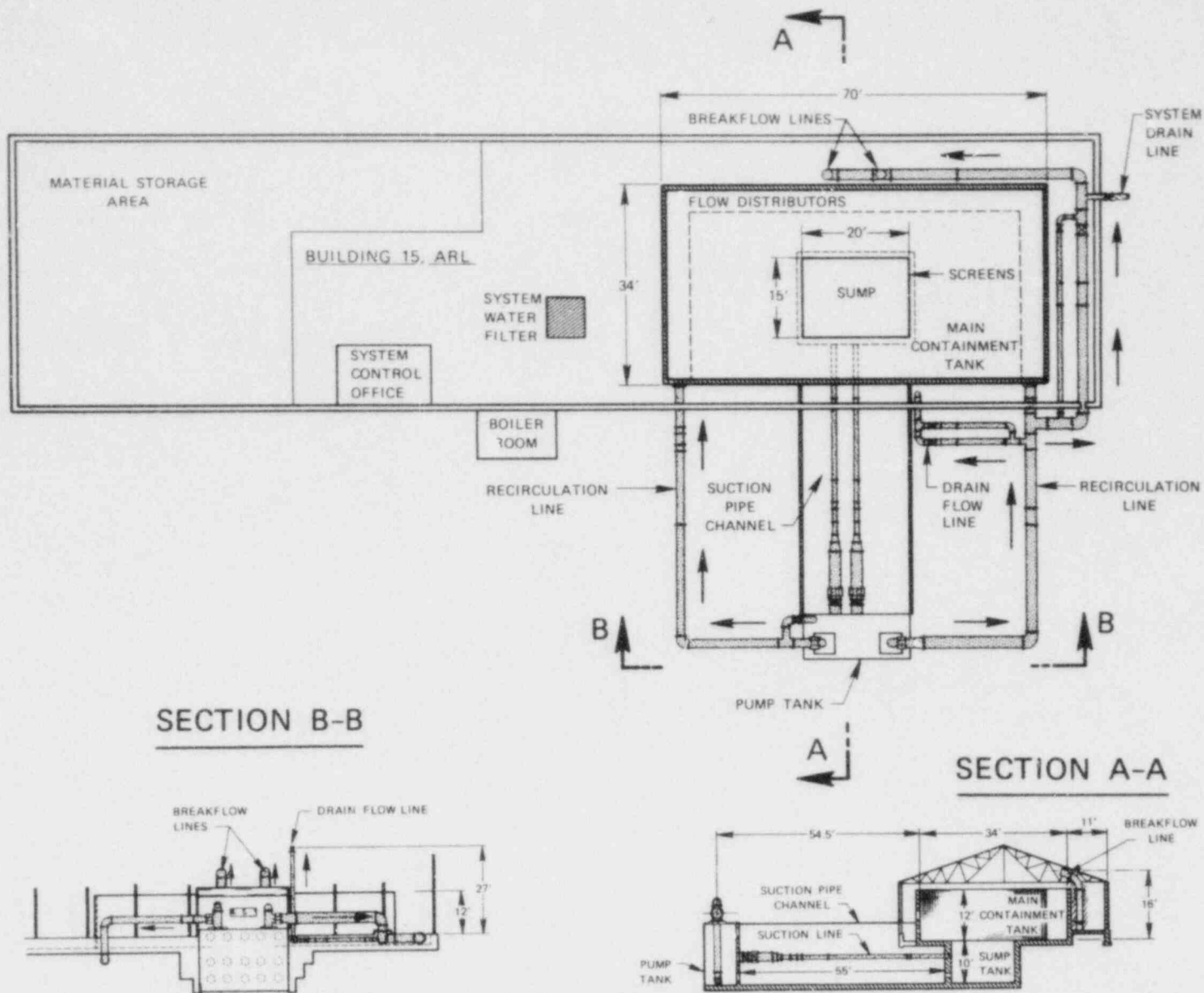
Figure 4-3. Details of the Main and Sump Tanks and of the Piping
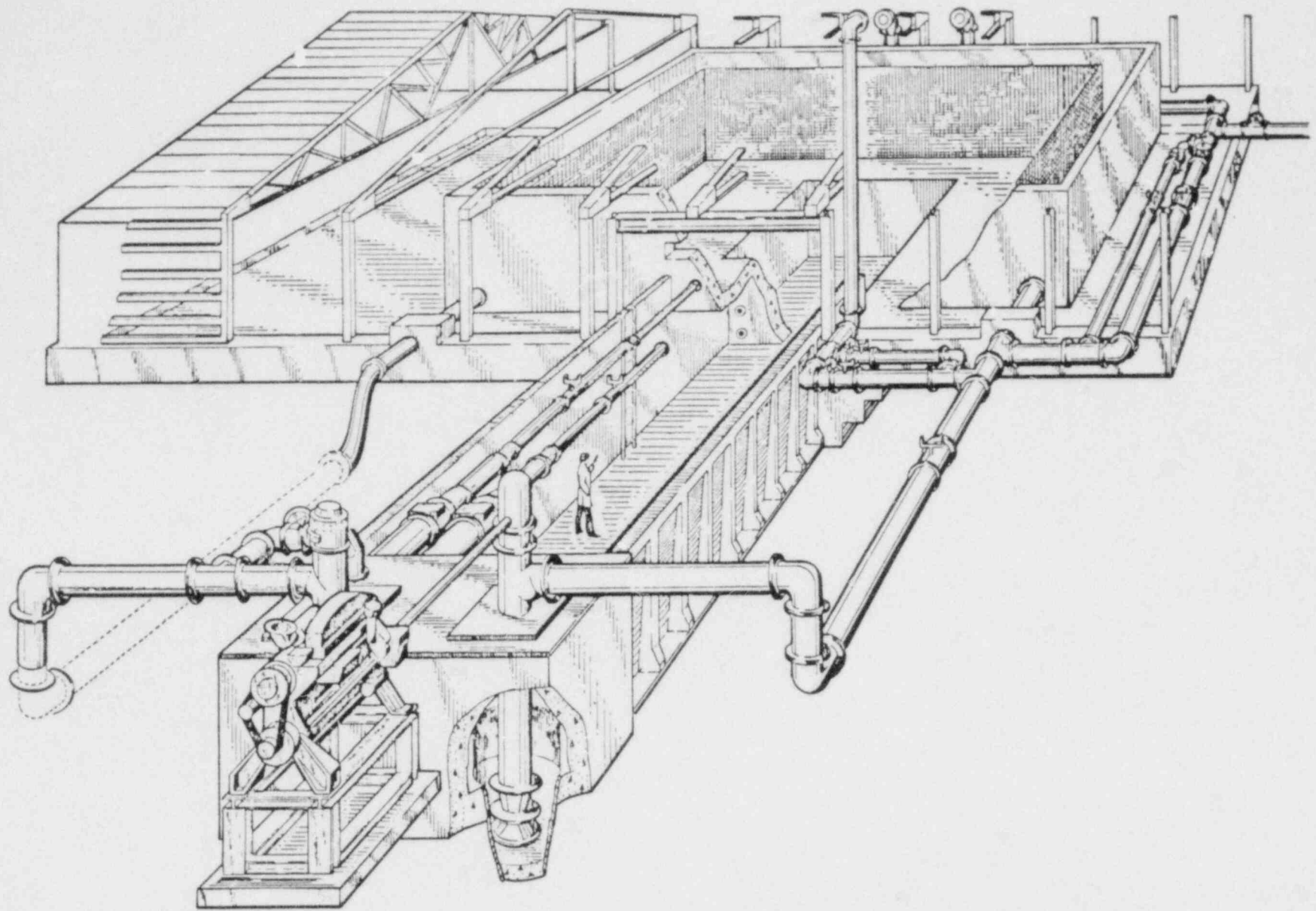
Figure 4-4. Perspective View of the CESP Facility

or surface conditions. The CESP sump geometry variables
have the following ranges (see Table 4-1 and Figure 4-1):

s: 0.15 to 6.1 m (0.5 to 20 ft)   a: 0.3 to 1.83 m
                                            (1 to 6 ft)
d: 20.32, 30.48, 40.64, 60.96 cm
    (8, 12, 16, 24 in)   c: d/2 to .91 m
                                            (3 ft)

L: 1.83 to 6.1 m (6 to 20 ft)   e: d/2 to 3.05 m
                                            (10 ft)

B: 1.22 to 4.57 m (4 to 15 ft)   f: 1.22 to 4.88 m
                                            (4 to 15 ft)

b: 0.3 to 4.57 m (1 to 15 ft)   g: 0 to 1.83 m
                                            (0 to 6 ft)

ARL has projected a test facility completion date of
mid-June 1980; check-out of the test facility will require
about one month.

4.4 Test Program

The test plan for the CSR program is designed to have
broad application, and it will serve two purposes. First,
it will provide an extensive data base to the NRC for the
resolution of sump vortexing problems, a part of unresolved
safety issue A-43. Second, the same data will provide
ECCS sump design information to the nuclear industry in
general.

The test program covers three broad areas of interest
for ECCS sump design. They are

Table 4-1

Geometric, Flow, and Fluid Property Variables

Geometric Variables	Flow Variables	Fluid Property
1. Pipe diameter, d	1. Volumetric Flow per pipe, Q	1. Density
2. Sump length, L	2. Circulation,	2. Viscosity,
3. Sump width, B	3. Submergence, s	3. Surface tension,
4. Approach depth at screen, a		
5. Screen distance from sump wall, g		
6. Depth to pipe entrance from building floor, b		Acceleration due to gravity, G
7. Depth to pipe entrance from sump floor, c		
8. Pipe entrance orientation parameters, e_x, e_y		
9. Pipe spacing, f		
10. Wall clearance, x		

the generic behavior of the sump with uniform
approach flow conditions (Phase I)

changes in the generic behavior of the sump as a
result of adverse conditions caused by flow disrup-
tions (Phase II)

vortex suppression concepts (Phase III).

4.4.1 <u>Generic Sump Behavior (Phase I)</u>. Figure 4-1 illus-
trates a typical ECCS sump; Table 4-2 shows the 11 geometric
variables, 3 flow variables, and 3 fluid properties needed
to describe the sump. Standard dimensional analysis[2] using
a single length dimension--the pipe diameter (d)--gives

dependent variable = function $\left(\frac{L}{d}, \frac{B}{d}, \frac{a}{d}, \frac{b}{d}, \frac{g}{d}, \frac{c}{d}, \frac{e_x}{d}, \frac{e_y}{d}, \frac{f}{d}, \frac{s}{d} \right.$ R, F, W$\Big)$

(vortex severity, swirl, head loss, etc.)

where

R, Reynolds number = $\frac{Ud}{\nu}$

F, Froude number = $\frac{U}{\sqrt{Gs}}$

W, Weber = $\frac{U^2 d}{\sigma / \rho}$,

i.e., three dimensionless numbers and ten dimensionless
geometric variables which use the pipe diameter for non-
dimensionalization. Clearly, an ECCS sump is a multiple
length, multiple variable problem whose behavior cannot be

analyzed empirically with only a few dimensionless inde-
pendent variable:, as many simpler sump geometries could.
Consequently, Phase I experiments employ statistical design
methods. In particular, they use a fractional-factorial
experiment design.

The fractional-factorial technique is especially
applicable to problems that have a large enough number of
independent variables (such that a full factorial is imprac-
ticable), yet some information is available on the expected
behavior of the dependent variables. The fractional-factorial
method has two principle advantages:[3]

- it gives the variable main effects and some
  variable interactions,

- it allows each variable to be investigated over
  its range with a relatively small number of tests.

Phase I tests have two parts: fractional-factorial
experiments (part 1) and sensitivity tests (part 2). The
variables in the fractional-factorial tests are selected
using a judgmental ranking of each variable according to
its expected importance along with certain physical con-
straints imposed by the test facility. The geometric
variables selected for study in the fractional factorial
tests are d, L, B, b, g, e_x, and f. Part 2 tests the
remaining sump variables and topics of concern; these
sensitivity tests assume that the behavior of the parameter

under investigation is independent of the other variables, i.e., the sensitivity tests investigate one parameter at a time while holding all other variables fixed.

The flow rate and submergence will vary through broad ranges for each of the test configurations. Tables 4-2 and 4-3 show the fractional-factorial test plans. The -, 0, and + designations in the tables represent a low, median, and high value for each range. Table II describes a ($1/3$ x 3^4) fractional-factorial for the variables d, L, B and b. Investigation of the data from these twenty-seven test configurations will include analysis of variance, regression analysis, and dimensionless empirical correlation.[4,5,6]

The analysis of variance technique partitions the total variance in the measured variable into independent parts--each part associated with a factor (measured variable) of the experiment. This information will allow us to estimate factor effects and to perform associated tests of factor significance. Regression analysis* provides a systematic method for developing a prediction equation for estimating, with confidence limits, a response surface as a function of the independent factors. The resulting response relation provides an indication of the sensitivity of the response surface to changes in levels of the independent variables.

---

*Regression analysis can be considered a special case of analysis of variance; however, it is almost always referred to as a separate analysis method because of its special techniques and importance.

Table 4-2

Fractional Factorial Design $(1/3 \times 3^4)$
for the Factors d, L, B, and b

Trial	d	L	B	b	e_x	g
1	0	-	-	-	-	-
2	-	0	-	-	-	-
3	-	-	0	-	-	-
4	-	-	-	0	-	-
5	0	0	0	0	-	-
6	+	0	0	-	-	-
7	0	+	0	-	-	-
8	0	0	+	-	-	-
9	+	0	-	0	-	-
10	0	+	-	0	-	-
11	0	0	-	+	-	-
12	+	-	0	0	-	-
13	0	-	+	0	-	-
14	0	-	0	+	-	-
15	-	+	0	0	-	-
16	-	0	+	0	-	-
17	-	0	0	+	-	-
18	+	+	-	-	-	-
19	+	-	+	-	-	-
20	+	-	-	+	-	-
21	-	+	+	-	-	-
22	-	+	-	+	-	-
23	-	-	+	+	-	-
24		+	+	0	-	-
25	+	+	0	+	-	-
26	+	0	+	+	-	-
27	0	+	+	+	-	-

Table 4-3

Fractional Factorial Design ($1/2 \times 2^5$)
for the Factors d, L, B, e_x, and g

Trial	d	L	B	b	e_x	g
1	−	0	0	−	−	−
2	+	+	+	−	+	−
3	+	+	+	−	−	+
4	−	0	0	−	+	+
5	+	+	0	−	+	+
6	−	0	+	−	−	+
7	−	0	+	−	+	−
8	+	+	0	−	−	−
9	+	0	+	−	+	+
10	−	+	0	−	−	+
11	−	+	0	−	+	−
12	+	0	+	−	−	−
13*	−	+	+	−	−	−
14	+	0	0	−	+	−
15	+	0	0	−	−	+
16	−	+	+	−	+	+

---

*Same as trial 21 in Table 4-2.

The dimensionless empirical correlation will use the information gained in performing the analysis of variance and the regression analysis to produce plots, charts, or empirical expressions for the main sump behavior as a function of the main dimensionless variables or dimensionless numbers.

Table 4-3 describes a $(1/2 \times 2^5)$ fractional-factorial for the variables d, L, B, e_x, and g (note that $f = L - 2e_x$); data are reduced as before. At this point the two fractional-factorial experiments will be combined, the variables Q and s included, and a regression equation involving all the factors formed. This final relation will describe a major portion of the sump's behavior including interdependent variable interactions.

The sensitivity experiments will test both sump parameters and sump orientation and configuration concepts. This testing will investigate the following twelve items:

- nonsymmetrical outlet pipe orientations
- vertical outlet pipe orientations
- BWR outlet pipe configurations
- effect of variable e_y
- effect of variable x
- effect of variable c
- cover plate (variable a)

- 8 in. diameter outlet pipes
- scale effects
- temperature effects
- single outlet pipe operation and associated transient
- outlet pipe shape, i.e., bellmouth or cone.

The sensitivity tests will be performed by varying one of the above sensitivity parameters through several configurations (usually 3) while keeping the other geometric sum. parameters fixed.

The testing will consist of two types of procedures: steady-state tests and survey tests; Figure 4-5 illustrates both types. For a steady-state test, flow rate (Q) and submergence (s) are held constant while data set: a least 30) are sequentially recorded for each value of Q and s; these tests are then statistically analyzed (mean, standard deviation, etc.). In the survey test submergence (s) is held constant while the flow varies in discrete, small steps through the flow range; only a single data set is recorded for each flow value. The data analysis of the survey data will employ the statistical results found at each of the steady-state points.

4.4.2 Approach Flow Perturbations (Phase II).

The Phase II test series will determine the behavior of the sump when subjected to approach flow perturbations--
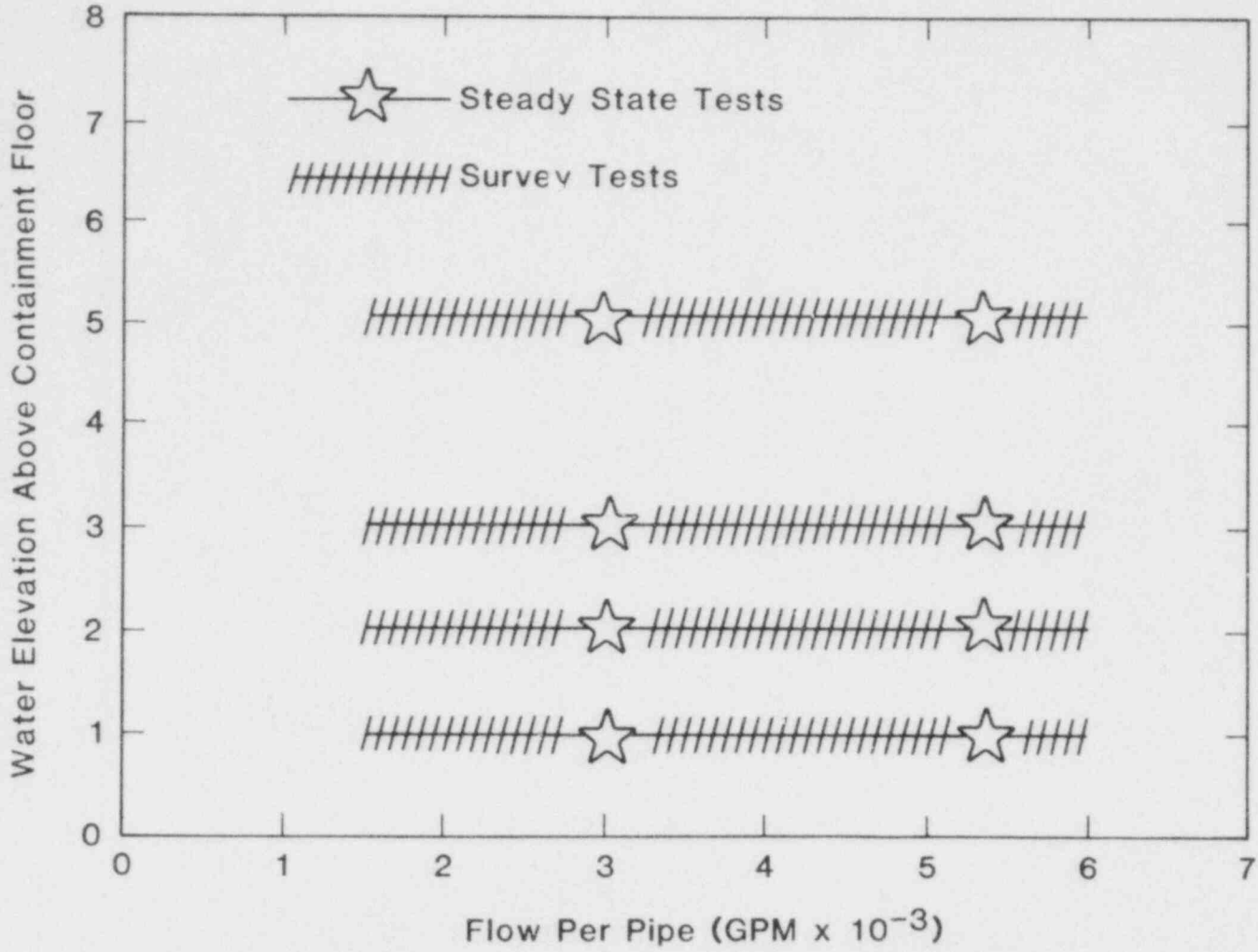
Figure 4-5.   Two Types of Test Procedures: Steady State
and Survey Testing

both above and below the surface. The flow disturbances considered are screen blockage (up to 75%), break flow impingement, drain flow impingement, flow-rate transients, and nonuniform approach velocity distribution and obstructions.

Phase II will select test configurations or the basis of Phase I test results; however, Phase II considers only sump configurations with desirable characteristics.

Phase II test procedures are similar to Phase I, part 2. Phase II places particular emphasis on establishing the inherent stability of severely perturbed sump designs. A sump excursion from the baseline behavior in Phase I provides data which will determine trends in vortexing, the movement of any phenomenon boundaries, increased or decreased profile losses, etc.

4.4.3 Vortex Suppression (Phase III).

A sustained air core or debris entraining vortex can lead to high inlet losses, to decreased pump performance, or even to pump failure. Phase III will consider the development and evaluation of vortex suppressors. Generally, vortices and flow rotation in a sump are suppressed using two processes: form drag and viscous dissipation. A vortex suppressor exhibits a large form drag in the direction of expected flow rotation; this will suppress the angular rotation of the water. Additionally, the suppressors break

up the large-scale motion; the resulting smaller scale motions will dissipate viscously.

Vortex suppressor configurations under investigation include horizontal grates, inner cages, and splitter vanes. Horizontal grates are usually placed in several layers below the minimum water level; grate configurations to be tested in Phase III consist of standard floor grates, perforated plates, and heavy screen mesh. Inner cages fit directly over the outlet pipe entrance; Phase III testing will investigate various cage geometries built of perforated plates, floor type grates, and screen. Splitter vanes, normally placed at the pipe entrance, reduce swirl; Phase III testing will evaluate the swirl-reducing effectiveness of various splitter vane geometries (number of vanes, etc.).

References

1. Durgin, W. W. and Padmanabhan, M., "Assessment of Hydraulic Performance of Containment Recirculation Sumps as Influenced by Various Geometric and Flow Parameters," Alden Research Laboratory Report, Fiscal Year Report for 1979, October 1979.

2. Fox, R. W. and McDonald, A. T., Introduction to Fluid Mechanics (New York: John Wiley and Sons, Inc., 1973).

3. Federer, W. T., _Experimental Design_ (New York: The MacMillan Company, 1955).

4. Hald, A., _Statistical Theory with Engineering Applications_ (New York: John Wiley and Sons, Inc., 1952).

5. Draper, N. R. and Smith, H., _Applied Regression Analysis_ (New York: John Wiley and Sons, Inc., 1966).

6. Crow, E. L., Davis, F. A., and Maxfield, M. W., _Statistics Manual_ (New York: Dover Publications, Inc., 1960).

DISTRIBUTION:

US Nuclear Regulatory Commission (400 copies for R3)
Division of Document Control
Distribution Services Branch
7920 Norfolk Avenue
Bethesda, MD 20014

US Nuclear Regulatory Commission (7)
Office of Nuclear Regulatory Research
Washington, DC 20555
Attn: R. DiSalvo
       S. Fabic
       D. A. Hoatson
       C. E. Johnson
       R. R. Sherry
       C. Z. Serpan
       L. H. Sullivan

US Nuclear Regulatory Commission (6)
Division of Systems Safety
Office of Nuclear Reactor Regulation
Washington, DC 20555
Attn: T. P. Speis
       J. F. Meyer
       N. Lauben
       J. K. Long
       A. R. Marchese
       W. R. Butler

US Department of Energy
Operational Safety Division
Albuquerque Operations Office
P. O. Box 5400
Albuquerque, NM 87185
Attn: J. R. Roeder, Director

Kraftwerk Union (2)
Hammerbacher strasse 12 & 14
Postfach 3220
D-8520 Erlangen 2
Federal Republic of Germany
Attn: Dr. M. Peehs
       Dr. K. Hassmann

Gesellschaft für Kern Forschung (2)
75 Karlsruhe
Postfach 3640
Federal Republic of Germany
Attn: Dr. J. P. Hosemann
       Dr. S. Hagen

Dr. H. Karwat
Technische Universitaet Muenchen
D-8046 Garching
Federal Republic of Germany

Distribution (cont'd):

Prof. F. Mayinger
Technische Universitaet Hannover
3000 Hannover 1
Federal Republic o⌐ Germany

Dr. M. V. Banaschik
Gesellschaft Fuer Reakforsicherheit (GRS)
Postfach 101650
Glockengasse 2
5000 Koeln 1
Federal Republic of Germany

Swedish State Power Board   (2)
El-Och Vaermeteknik
Sweden
Attn: Eric Ahlstroem
        Wiktor Frid

M. El-Genk
EG&G - Idaho. Inc.
P. O. Box 1625
Idaho Falls, ID 83401

R. A. Bari
Brookhaven National Laboratory
Upton, NY 11973

M. L. Stevenson
Los Alamos Scientific Laboratory
P. O. Box 1663
Los Alamos, NM 87545

Electric Power Research Institute   (2)
3412 Hillview Avenue
Palo Alto, CA 94303
Attn: J. Carey
       L. B. Thompson

D. H. Walker
Offshore Power System
8000 Arlington Expressway
Box 8000
Jacksonville, FL 32211

L. Hochreiter
Westinghouse Corp.
Nuclear Energy Systems
P. O. Box 350
Pittsburgh, PA 15230

Prof. S. Abdul-Kalik
Nuclear Engineering Department
University of Wisconsin
Madison, WI 53706

Distribution (cont'd):

S. G. Bankoff
Chemical Engineering Department
Northwestern University
Evanston, IL 60201

1223	R. R.	Prairie
2510	D. H.	Anderson
2513	J. E.	Kennedy
2514	D. E.	Mitchell
4000	A.	Narath
4400	A. W.	Snyder
4410	D. J.	McCloskey
4412	J. W.	Hickman
4414	G. B.	Varnado
4414	A. S.	Benjamin
4414	W. B.	Murfin
4420	J. V.	Walker
4421	R. L.	Coats
4422	D. A.	Powers
4422	R. M.	Elrick
4424	W.	Breitung
4425	W. J.	Camp
4440	G. R.	Otey
4441	M.	Berman (15)
4441	R. K.	Cole, Jr.
4441	M. L.	Corradini
4441	J. C.	Cummings
4441	J. F.	Muir
4441	M. P.	Sherman
4441	G. G.	Weigand
4442	W. A.	Von Riesemann
4443	D. A.	Dahlgren
4444	S. L.	Thompson
4444	L. D.	Buxton
4444	R. K.	Byers
4445	L. O.	Cropp
4450	J. A.	Reuscher
5130	G. A.	Samara
5131	B.	Morosin
5131	W. B.	Benedick
5512	D. W.	Larson
5520	T. B.	Lane
5521	L. W.	Davison
5530	W.	Herrmann
5534	J. F.	Assay
5534	D. S.	Drumheller
5830	M. J.	Davis
5836	J. L.	Ledman
5836	L. S.	Nelson
5846	E. K.	Beauchamp
5846	R. A.	Sallach
8266	E. A.	Aas
3141	T. L.	Werner (5)
3151	W. L.	Garner (3)
	For DOE/TIC (Unlimited Release)	
3154-3	R. P.	Campbell (25)
	For NRC Distribution to NTIS	